THE EFFECT OF WATER ON MANTLE MELTING

Leonie Hall

August 1999

A dissertation submitted to the University of Bristol in accordance with requirements of the degree of Ph.D. in the Faculty of Science

27,900 words

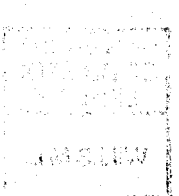

ABSTRACT

Water is an essential component in the generation of island arc magmas. Hydrous peridotite partial melting experiments at 1.5 and 3GPa simulate mantle melting processes in the subduction zone environment. FeO* and H_2O loss is minimised by using $Au_{80}Pd_{20}$ capsules and a starting mix initially reduced at $fO_2 \geq QFM+1$ at 1atm.

Adding H_2O to peridotite lowers the temperature of melting. At 1.5GPa and melt fraction (F) >8wt%, the decrease in melting temperature is directly proportional to peridotite H_2O content. At F<8wt%, onset of melting is controlled by amphibole composition and stability. At 3GPa and F>15wt%, rate of melting with increase in temperature is similar in hydrous and anhydrous peridotite. In a K_2O-free peridotite, onset of melting is expected to start at the H_2O-saturated solidus. Rate of melting at near-solidus temperatures is lower in hydrous peridotites than in anhydrous at 1.5-3GPa.

Lower melting temperature in hydrous lherzolite at 1.5GPa produces diopside-rich and enstatite-poor clinopyroxene (cpx) relative to anhydrous lherzolite. The mineral assemblage is enriched in cpx and olivine at the expense of orthopyroxene (opx). At F=5-22wt%, hydrous melts are depleted in MgO and CaO, and enriched in Al_2O_3. At F<5wt%, hydrous melts co-exist with amphibole and are Na_2O- and Al_2O_3-poor and SiO_2-rich. At F>22wt%, hydrous and anhydrous melts are similar in composition.
Increasing pressure to 3GPa causes greater olivine contribution to melting. Hydrous melts become enriched in MgO and FeO, depleted in SiO_2, CaO and Al_2O_3 and approach anhydrous melt compositions. Enstatite and jadeite components in cpx increase with pressure and opx decreases in abundance. Lower melting temperature stabilises garnet to larger melt fractions in hydrous peridotite. This results in MgTs-depleted opx, CaTs-depleted cpx and slightly Al_2O_3-poor melts, relative to anhydrous peridotite.

My results demonstrate that primitive basalt compositions erupted in island arcs can be generated by 8-28wt% melting of peridotite at 1-1.5GPa (30-45km). Melting is assumed to start in the mantle wedge at 2.7-3GPa (≈100km depth) (Tatsumi *et al.*, 1983; Iwamori *et al.*, 1995), so it is likely that these melts re-equilibrate at shallower depth before eruption.

ACKNOWLEDGEMENTS

My supervisors Bernie Wood and Mike Carroll initially proposed this project and provided ideas and direction during its development. In particular thanks go to Bernie for help on experimental technique and oxidation state calculations. Thanks go to Mike for advice on arc basalts, cheery emails and constructive proof-reading in the final stages. I owe a great deal to James Brodie, with whom I collaborated on the Fe and H_2O loss investigation and some of the experiments at 1.5GPa. James also donated The Bigger Faster Computah to the cause, and I am grateful to him for guidance, moral support and patience in the early days.

Fred Wheeler, Mike Dury, Stuart Kearns and John Craven all provided valuable technical assistance, and a reassuring calmness during moments of potential destruction.

Peter Ulmer and John Schumacher examined this thesis and I would like to thank them for their thorough, positive approach and debate. This manuscipt and my ideas have benefited enormously from their suggestions.

I owe a big thankyou to my CETSEI colleagues for helping me to master the art of experimental petrology. Afternoons in the dungeon were made a lot more fun by their wide-ranging lab discussions and music tastes. Speacial thanks go to my former partner-in-crime Kate Moore for 3 years of great friendship and Irn Bru.

My family have been understanding, encouraging and generous throughout my years of studying, and I acknowledge their help with love and gratitude. Finally I would like to thank Greg. His unswerving love, support, and encouragement, especially in the last few months, made this whole fandango seem possible.

AUTHOR'S DECLARATION

I declare that the work in this dissertation was carried out in accordance with the Regulations of the University of Bristol. The work is original except where indicated by special reference in the text and no part of the dissertation has been submitted for any other degree.

Any views expressed in the dissertation are those of the author and in no way represent those of the University of Bristol.

4 February 2000

TABLE OF CONTENTS

LIST OF TABLES

LIST OF FIGURES

CHAPTER 1

Introduction

Water is the most abundant volatile in the Earth's mantle, and is an essential component in subduction zone magmatism and global recirculation of materials. Our understanding of subduction zone processes depends on a good quality database describing the effect of water on partial melting of the mantle under conditions appropriate to the mantle wedge. Little quantitative data exist on hydrous mantle melting, however, particularly at depths of >70km. In this study, the phase relations and melt compositions of an H_2O-undersaturated peridotite have been experimentally determined under conditions equivalent to 40-100km depth in the mantle. Hydrous peridotite melting is quantitatively described as a function of pressure, temperature and H_2O content.

1.1 Chemical composition of the upper mantle

The upper mantle is usually defined by the Mohorovic discontinuity at its top surface and the 660km seismic discontinuity at its base. This study is primarily concerned with the processes and products of melting in the subduction zone mantle wedge. Seismic studies of subduction zones suggest that partial melting initiates at 100-120km depth within the mantle wedge (*e.g.* Gill, 1981), so in this study attention is focussed on the region of the upper mantle between the Moho and 100km depth (1-3GPa).
The bulk composition of the mantle is a subject of long-standing debate. Several lines of evidence suggest that the upper mantle is composed predominantly of peridotite.

1.1.1 Seismic data

Table 1.1 Comparitive seismic properties of peridotite and eclogite in the upper mantle to 70km depth (Ringwood, 1975; Anderson, 1989).

Property	Upper mantle	Peridotite[a]	Eclogite
P-wave velocity (km/s)	7.9 - 8.6, mean = 8.2 ± 0.2	8.2 - 8.3	8.2 - 8.6
Poissons ratio	0.25 - 0.26	0.25 - 0.26	0.30 - 0.32
Anisotropy (P-wave, %)	3 - 7	3 - 10	0.5 - 3
Density, S-wave data (g/cm^3)	3.33	3.25 - 3.4	3.4 - 3.6
Density, isostasy data (g/cm^3)	3.24 - 3.32	3.25 - 3.4	3.4 - 3.6

[a] Peridotite containing olivine Fo_{90}.

From Table 1.1, it can be seen that the P-wave velocities measured in the upper mantle are consistent with a peridotite or an eclogite composition. Observed values for Poissons ratio,

anisotropy and density, however, strongly favour peridotite as the bulk mantle composition.

1.1.2 Evidence from meteorites

The Solar System formed at 4.6Ga through the gravitational collapse of dispersed matter in interstellar space. Carbonaceous chondrites have radiometric ages of 4.6Ga, so are thought to represent the general chemical composition of the primordial solar nebula, and the material that condensed to form the Earth. After segregation of the core, the bulk composition of the Earth's primordial mantle has been calculated (Wyllie, 1981) to be:

(a) >90 wt% due to SiO_2, MgO and FeO. No other oxide >4wt%.
(b) 5-8 wt% due to Al_2O_3, CaO and Na_2O.
(c) >98 wt% due to these 6 oxides. No other oxide is >0.6 wt%

Only peridotite corresponds to this bulk composition.

1.1.3 Experimental studies

Early workers recognised that basalt magma is erupted in great volumes at the Earth's surface, and deduced that it must be derived from the mantle by partial melting (Bowen, 1928). Experimental studies have demonstrated that partial melts of peridotite are predominantly basaltic, and form liquids which are parental to the range of magmas observed at mid-ocean ridges and island arcs. Previous experimental studies are reviewed in detail in section 1.3.

1.1.4 Ultramafic rocks

Ultramafic rocks of potential mantle origin occur in 2 forms: as xenoliths, and in tectonically-emplaced terranes.

(i) Ultramafic Xenoliths

These provide the freshest samples of ultramafic rock presumed to be derived from the mantle. They are most commonly brought to the surface by eruption of CO_2-rich, SiO_2-poor mafic magmas (*e.g.* kimberlite, nephelenite or alkali basalt). The occurrence of diamonds in kimberlites implies a depth of origin of at least 140km, so kimberlitic magma will traverse upper mantle peridotite on its path to the surface. Ultramafic xenoliths are very abundant in kimberlites (Dawson, 1980; Nixon, 1987), and are believed to represent

mantle sampled at different levels during the magma's ascent. The most common xenolith composition is garnet lherzolite (Gurney & Harte, 1980) which is believed to originate in the deeper parts of the upper mantle (>60km).

Peridotitic xenoliths have also been found in alkali-basalt suites (Menzies, 1983; Nixon, 1987). In these xenoliths, spinel lherzolite is the most abundant composition, with minor garnet lherzolite. Since the dominant aluminous phase in the lherzolites is spinel rather than garnet, they are thought to have been sampled from shallower depths than the xenoliths in kimberlites. However, there is chemical and isotopic evidence that they may represent metasomatised residues after partial melting (Frey & Prinz, 1978). Xenoliths from kimberlites are therefore considered to be more reliable evidence of the mantle composition.

(ii) Alpine-type peridotites, and ultramafics in ophiolite complexes

Alpine-type peridotites and ophiolite complexes are exotic terranes characterised by rocks with ultramafic petrology, and field evidence of tectonic emplacement, *e.g.* the Lizard complex, Cornwall; Troodos ophiolite, Cyprus. In ophiolites, rocks that are derived from the oceanic crust are also preserved (Coleman, 1977; Gass *et al.*, 1984). A wide range of ultramafics have been identified in the alpine-type peridotites and ophiolites, the most abundant being lherzolite and compositions interpreted to be the products of partial melting of peridotite. Experimental studies show that these mineral assemblages are stable at pressures equivalent to mantle conditions, and the terranes are deduced to have originated as part of the upper mantle and overlying crust, subsequently thrust on land by tectonic processes.

In summary, there is strong geophysical, cosmochemical and petrological evidence that the upper mantle has a peridotitic composition. In addition to peridotite, there is also evidence of other ultramafic compositions in the upper mantle *e.g* harzburgite, pyroxenite and eclogite, and various models of mantle layering have been proposed to explain their existence (*e.g.* Anderson, 1979, 1982; Ringwood, 1982; Gasparik 1992a, 1993). However, peridotite is still the most plausible model of upper mantle bulk composition.

1.2 H_2O in the mantle

There are several lines of evidence for the presence of water in the mantle. Direct evidence comes from hydrous minerals (*e.g.* amphibole, mica) in mantle xenoliths and nodules (Wyllie, 1967; Sobolev, 1977; Dawson, 1980; Mitchell, 1986), and H_2O in fluid

inclusions in diamonds (Navon *et al.*, 1988; Schrauder & Navon 1993). Hydrous basalt glasses indicate H_2O must be present in the magma's mantle source region (Perfit *et al.*, 1981; Stolper & Newman, 1994). Indirect evidence comes from models of subduction volatile recycling (*e.g.* Peacock, 1990), which conclude that H_2O must be stored in the mantle.

H_2O in the mantle has 4 possible sources: (i) shallow recycled water from the hydrosphere, (ii) water assimilated from crustal rocks, (iii) hydrous minerals in subducted oceanic crust and sediments, and (iv) primordial H_2O. H_2O is most commonly stored in the upper mantle in hydrous minerals (*e.g.* amphibole, mica, chlorite, talc, dense hydrous magnesian silicates). It is also held in small but significant amounts in nominally anhydrous minerals such as olivine and pyroxene (Bell & Rossman, 1992; Kohn, 1996). As the mantle convects, the H_2O-bearing minerals break down when their pressure and temperature stabilities are exceeded. Water is released and reacts with the surrounding peridotite to form new more stable H_2O-bearing minerals. Where excess H_2O remains, it may be retained as a grain boundary fluid phase or it may flux the peridotite and form a hydrous silicate melt, depending on mantle chemistry and physical conditions.

There is evidence that H_2O is not distributed evenly throughout the upper mantle. Mid-ocean ridge basalts (MORB) have typical H_2O contents of 0.1-0.3wt% (Dixon *et al.*, 1988; Michael, 1988; Sobolev & Chaussidon, 1996). This corresponds to approximately 0.01-0.045wt% H_2O in their upper mantle source (Michael, 1988). Island arc basalts, basaltic andesites and boninites are characterised by high H_2O contents, typically 2-5wt% (Stolper & Newman, 1994; Baker *et al.*, 1994; Dobson *et al.*, 1995; Sobolev & Chaussidon, 1996). Estimates of the corresponding upper mantle H_2O content vary from 0.1-0.2wt% (Sobolev & Chaussidon, 1996), to 0.3-0.7wt% (Stolper & Newman, 1994) to 0.6-1.5wt% (Baker *et al.*, 1994). It is clear, however, that the subduction zone upper mantle is in enriched in H_2O, and this is reflected in the explosive volcanism observed in island arcs.

1.3 Oxidation conditions in the upper mantle

Oxygen fugacity (fO_2) in the upper mantle is believed to be heterogeneous and varies up to at least 4 log units (Wood *et al.*, 1990; Luth *et al.*, 1990; Ballhaus, 1992). Mantle fO_2 has been estimated in different tectonic environments by oxygen thermobarometry, Fe^{3+}/Fe^{2+} ratios in glasses (Christie *et al.*, 1986) and volatile speciation in lavas (*e.g.* Carmichael, 1991). Within the spinel stability field, mantle beneath spreading ridges is estimated to have fO_2 of 1 log unit below the quartz-fayalite-magnetite buffer (QFM-1)

(Christie *et al.*, 1986; Wood *et al.*, 1990; Ballhaus, 1992). The upper mantle in subduction zones is thought to be more oxidised than in areas of extension. Estimates of fO_2 in subduction zone mantle vary from QFM to QFM+1.5 (Wood *et al.*, 1990) and from QFM to QFM+3 (Ballhaus, 1992).

Oxygen fugacity exerts a strong influence on the speciation of mantle fluids, which consist primarily of C, H and O (Anderson, 1975). Under fO_2 conditions typical of spreading ridge and subduction zone mantle ($fO_2 \geq$QFM-1), the dominant fluid species are H_2O and CO_2, whilst at lower fO_2, CH_4, CO and H_2 dominate (Holloway, 1981). The fO_2 conditions also influence the speciation of Fe (and other polyvalent elements) and hence the composition and phase equilibia of Fe-bearing mantle minerals.

1.4 Previous experimental work

1.4.1 Experimental work on anhydrous peridotite melting

It is widely accepted that most basalts are derived from liquids produced by partial melting of peridotite. The theory was proposed as early as 1915 by Harper, but it was Bowen (1928) who first made a reasoned case for it. At the time it was a controversial idea, and until the mid-1940s it was more popularly believed that basaltic magma came from layers of basaltic composition, *e.g.* in the crust (Kennedy & Anderson, 1938) or in a glassy stratum beneath the crust (Daly, 1933).

During the 1950s, advances in petrology, cosmochemistry and geophysics all suggested the dominance of peridotite in the mantle, and its significance to basalt petrogenesis. Equally importantly, new experimental equipment was developed that allowed quantitative study of basalt and peridotite melting behaviour under mantle conditions. The first experimental studies were carried out at 1 atm, in simple and natural systems (Osborn & Tait, 1952). They showed that an equilibrium thermal divide exists between alkali basalts and tholeiites at this pressure. The invention of the piston cylinder (Boyd & England, 1960) led Yoder & Tilley (1962) to carry out the first major experimental work on basalt magma genesis at higher pressures. This showed that the 1 atm thermal divide between alkali basalts and tholeiites is broken down at high pressure (>2GPa). They concluded that both types of basalt were generated by partial melting of garnet peridotite at depths of 60km or less. This confirmed the proposal by Kuno (1960) that pressure is a strong control on melt composition, and that different primary magmas can be produced at different depths in the mantle.

Green & Ringwood (1967) determined the phase relations for a series of basalt compositions, and compared the near-liquidus minerals with the near-solidus minerals in an upper mantle composition under the same pressure (P) and temperature (T) conditions. A major departure was that instead of peridotite, they used "pyrolite" (pyroxene-olivine rock). This is a synthetic mixture of peridotite and basalt that they argued was much closer to a primary undifferentiated mantle composition (Ringwood, 1962a, 1962b). In pyrolite, Green & Ringwood (1967) showed that garnet was only stable at depths of 100km or more, so they concluded that it would not play a significant role in the genesis of primary magmas in the mantle. Green & Ringwood (1967) identified a primitive olivine-rich tholeiitic liquid formed at 35-70km. This, they argued, was the only primary liquid from mantle melting, and alkali basalt could be derived from it by subsequent olivine fractionation.

These early studies highlighted some serious experimental problems. The charges were sealed in Pt capsules, and suffered from Fe loss due to reduction of Fe oxides to metal which then alloyed with the Pt. To try to limit Fe loss, very short run times were used (e.g. 1 hour) which were insufficient to achieve equilibrium of the run products.

Mysen & Kushiro's study (1977) was one of the first to look at direct partial melting of peridotite. They used $Pt_{95}Au_5$ capsules to try to minimise Fe loss but their experiments showed up to 20% relative Fe loss. Mysen & Kushiro (1977) tried to measure the degree of partial melting using a radioactive tracer that was concentrated in the melt, but the data were poorly constrained due to analytical problems. The study did provide useful information on phase stabilities along the melting curve. Results showed that melt composition is related to the residual mineral assemblage, and that the modal amounts and compositions of the crystals in the assemblage are controlled by the bulk composition of the peridotite. Mysen & Kushiro (1977) concluded erroneously that the melt composition remained relatively constant until a phase had been exhausted, and therefore was isobarically pseudoinvariant. They assumed that peridotite melting behaviour was analogous to that seen in simple system studies (*e.g.* Kushiro & Yoder, 1974).

Jaques & Green (1980) studied direct partial melting of 2 different peridotites, which had 40wt% olivine subtracted from their compositions. This increased the modal abundance of the remaining phases and aided their identification, especially near elimination. Not only did the experiments suffer from Fe loss and short run times but another major problem was identified. During quenching, meta-stable disequilibrium phases nucleate as crystals and as rims on primary phases, causing modification of the melt. Direct analysis of the quench-modified liquid did not provide an accurate estimation of the true equilibrium melt composition. Instead, Jaques & Green (1980) calculated the equilibrium melt composition

by mass balance, using the compositions and estimated modal abundances of residual phases, and a bulk composition corrected for iron loss (Green, 1973, 1976). The method introduced considerable uncertainties, however, both in phase composition (because of zoning in crystals) and phase proportions, and the resulting melt compostions are poorly constrained.

During the same period, 2 major studies of basalt crytallization were carried out by Presnall *et al.* (1978) and Stolper (1980). Both focussed on the origin of MORB but used different methods and came to very different conclusions. Presnall *et al.* (1978) studied the simple CaO-MgO-Al_2O_3-SiO_2 (CMAS) system, and showed that the peridotite solidus is composed of 3 curves which correspondto the three subsolidus assemblages of plagioclase lherzolite (0-1 GPa), spinel lherzolite (1-2.1GPa), and garnet lherzolite (>2.1GPa). Presnall *et al.* (1978) concluded that MORB were primary partial melts of plagioclase lherzolite, formed at ≈0.9GPa. Stolper (1980) used a different approach reasoning that, if MORB are primary melts, they must lie on the olivine+orthopyroxene cotectic at their depth of origin. He tested this by forcing saturation of MORB compositions with olivine and orthopyroxene, then re-analysing the melt. This method, first used by Walker *et al.* (1979), became known as the sandwich technique. It has the advantage that generally a sufficiently large pool of melt is created that quench modification is restricted to the periphery immediately adjacent to primary phases, and an analysable area of crystal-free glass remains. The second important technique developed by Stolper (1980) was the use of graphite capsules. This minimised Fe loss, although Stolper left them unsealed and therefore created the potential problem of H_2 diffusion across the capsule. From his results, Stolper concluded that not even the most primitive MORB are primary, but could be derived by olivine fractionation from a picritic parent formed at 0.5-2GPa. This conclusion was based on the assumption that the melting behaviour was pseudoinvariant at a given pressure which was also suggested by Mysen & Kushiro (1977).

Fuji & Scarfe (1985) demonstrated that melting behaviour is not pseudoinvariant. They ran sandwich experiments at 1GPa, and varied the bulk composition by using different peridotites, different basalts and varying proportions of peridotite/basalt. Fuji & Scarfe showed that at a given pressure, melt composition is controlled by the bulk composition of the system and by degree of partial melting. Peridotite melting behaviour is not isobarically pseudoinvariant, and a range of primary melts compositions can be generated isobarically. Fuji & Scarfe disagreed with Stolper (1980), and argued that most Mg-rich MORB could be primary.

Takahashi & Kushiro (1983) improved Stolper's method by sealing their graphite capsules in Pt to minimise hydrogen diffusion into the charge. This important study followed 2 lines of investigation. Firstly, they ran a series of sandwich experiments to establish the time required for run products to reach equilibrium. Secondly they performed experiments to establish the effects of pressure on the solidus and partial melt compositions of a fertile peridotite (HK66) at 0-3GPa. Results showed that the solidus is depressed relative to that in the CMAS system, due to the presence of alkalis, confirming conclusions drawn by Hoover & Presnall (1982) from work on the Na_2O-CMAS system. Partial melt compositions become systematically more enriched in olivine and undersaturated in SiO_2 with increasing pressure. Takahashi (1986) extended this work with another study using a slightly less fertile peridotite (KLB-1), similar in composition to Ringwood's pyrolite, and running experiments up to 14GPa. He showed that, at high pressure and temperature, increase in the enstatite component in clinopyroxene solid solution causes the orthopyroxene field to narrow and disappear at ≈3.5GPa.

Falloon & Green (1987) and Falloon *et al.* (1988) made a detailed study of anhydrous partial melting at 0.8-3.5GPa, using pyrolite and a more depleted peridotite (Tinaquillo lherzolite). Falloon & Green (1987) ran reversal experiments to test the melt compositions calculated by Jaques & Green (1980) and found that they contained too much normative olivine to be in equilibrium with partially molten peridotite. Falloon & Green (1987) used the data to produce a new set of liquid-solid cotectics in the CIPW normative basalt tetrahedron. Their data were in agreement with those of Takahashi (1986), and with those of Takahashi & Kushiro (1983) except for experiments at 0.8-1.2GPa. Falloon & Green (1987) suggested that Takahashi & Kushiro's (1983) cotectics at 0.8-1GPa were more consistent with a location at 1-1.2GPa, and that the difference arose from different pressure-calibrations between laboratories.

Theoretical studies emphasised that melting in adiabatically rising mantle is polybaric and near-fractional (McKenzie, 1984; Klein & Langmuir, 1987; McKenzie & Bickle, 1988). Early attempts to model this process were hampered by lack of experimental data at small melt fractions (Klein & Langmuir, 1987, 1988; McKenzie & Bickle, 1988, Niu & Batiza, 1991). Kinzler & Grove (1992a) performed sandwich experiments with high initial melt/peridotite ratios to generate a series of melt compostions saturated with a mantle mineral assemblage over a range of pressures, temperatures and melt fractions. Using their new data and that from previous studies, they generated a set of stoichiometric melting equations to parameterize mantle melting (1992b, 1993), and predicted liquid compositions produced by assimilation of polybaric, near-fractional melts. However, data to constrain the melting reaction at small melt fractions was still very sparse.

To study partial melting of peridotite at small melt fractions, a new technique known as the diamond aggregate method was developed by 2 independent groups of workers (Johnson & Kushiro, 1992; Baker *et al.*, 1992). A diamond matrix acts as a low pressure zone into which high pressure melts are pooled. This allows small melt fractions to be separated from the solid residue during quenching, preventing modification of the melt composition and producing an analysable area of glass. Hirose & Kushiro (1993) used this method to study melts formed by low degrees of partial melting (≈5wt%) at 1-3GPa. They concluded that isobaric normative melt composition becomes progressively nepheline-enriched with decrease in melt fraction.

Baker & Stolper (1994) and Baker *et al.* (1995) studied peridotite partial melting at 1GPa by means of the diamond aggregate method. From their results, they argued that liquids produced by very low degrees of partial melting (2wt%) would be high in SiO_2 and alkalis, and quartz-normative. This caused great controversy, and Falloon *et al.* (1996) suggested that equilibrium might not be easily achieved using the diamond aggregate method. In fact the problem was one of analytical error, and glasses from the experiments of Baker & Stolper (1994) and Baker *et al.* (1995) were recently re-analysed by Hirschmann *et al.* (1998). Results showed that very small melt fraction liquids do have high SiO_2, but this is strongly correlated with high alkalis, and the liquids are nepheline-normative not quartz-normative.

Robinson *et al.* (1998) studied low degree partial melts of 2 peridotites at 1.5GPa, using the sandwich technique in combination with multiple saturation experiments. Results agree well with those of studies using the diamond aggregate technique (Hirose & Kushiro, 1993; Kushiro, 1996). Robinson *et al.* generated a stoichiometric melting equation to describe near-solidus melting (0-3wt%) in a fertile peridotite. Hirose & Kawamura (1994) and Hirose & Kushiro (1998) have used the diamond aggregate method to compare incremental melting with batch melting at 0.5-2GPa. Incremental melts differ significantly in composition to batch melts generated under the same conditions, but aggregated incremental melts have a similar composition to batch melts. Higher temperature is required to produce an aggregated incremental melt than a batch melt of a similar total melt fraction.

In summary, early work on anhydrous partial melting provided a useful qualitative understanding of peridotite partial-melting. Quantitative work was hampered by experimental and analytical problems, especially Fe loss to capsules, and quench modification of melt. In the 1980s, development of the sandwich technique and use of graphite capsules overcame these problems. As the amount of data on anhydrous peridotite melting increased, so did our understanding of mantle processes.

Thermodynamic studies showed that adiabatic mantle melting is a polybaric and near-fractional process. Experimental studies during the 1990's have therefore focussed on studying liquid compositions at very low degrees of partial melting. A new experimental method, known as the diamond aggregate technique, was developed to achieve this. Although there were initial doubts about its validity, recent work has shown that there is good agreement between studies using the diamond aggregate technique and those using the sandwich technique.

1.4.2 Experimental work on hydrous peridotite melting

In parallel to work on anhydrous peridotite melting, experiments have been conducted to investigate the effect of H_2O on mantle properties. It had been suggested that under hydrous conditions, primary partial melts from an ultramafic mantle could be andesitic rather than basaltic (Poldevaart, 1955; O'Hara, 1965). This was the focus of the first experimental studies of the subject. Kushiro and co-workers initially studied melting behaviour in simplified systems + H_2O (Kushiro *et al.*, 1968; Yoder, 1969; Kushiro, 1969, 1970, 1972), and noted two important features. Firstly, the presence of H_2O dramatically lowered the solidus in the systems. Secondly, the effect of adding H_2O was to expand the liquidus volume of forsterite relative to enstatite, and to enrich the melt in SiO_2. Kushiro *et al.* (1972) extended the study to partial melting of natural hydrous peridotite, and generated a dacitic glass at 2.6GPa under H_2O-saturated conditions. They concluded that andesitic magmas could be primary melts of peridotite under high-pressure, vapour-present conditions.

The production of andesitic liquids by direct melting of peridotite was challenged by Ringwood and co-workers (Green & Ringwood, 1964; Green & Ringwood, 1967; Nicholls & Ringwood, 1973). Using basalt crystallization studies, they confirmed that H_2O increased the stability of olivine, but showed that basaltic andesites or dacites were not in equilibrium with hydrous peridotite at >2GPa. They argued that Kushiro *et al.*'s (1972) dacitic glass had been quench-modified from a more mafic composition. Green (1973, 1976) continued their work with a major investigation into the melting and phase relationships of peridotite in the upper mantle, under H_20-saturated and undersaturated conditions. Ringwood's (1975) "pyrolite" was used, with 40wt% olivine subtracted from its composition to aid identification of the other phases. The results highlighted several experimental and analytical problems, in particular the severe Fe loss to the AgPd or Pt containers, and quench modification of glassed melts. To overcome this, Green used short run times, and calculated the expected equilibrium melt compositions using the residual phase compositions and their estimated abundances (as in Jaques & Green, 1980). The method introduces many errors, and equilibrium may not have

been reached. An important qualitative conclusion, however, was that the H_2O-undersaturated solidus coincided closely with the dehydration and melting of amphibole, and was intermediate to the dry and excess-H_2O solidi.

In the same period Mysen & Boettcher (1972, 1973, 1975a,b) determined the phase relations of natural peridotite + H_2O-CO_2, under vapour-saturated conditions. Their experiments showed marked and progressive Fe loss to AgPd containers that suggested disequilibrium. Their solidi were much lower than those determined in all previous studies, and it has been suggested (Green, 1976) that Mysen & Boettcher (1972, 1973, 1975a,b) misinterpreted glass quenched from vapour under subsolidus conditions as quenched melt.

Milhollen *et al.* (1974) studied the phase relations of a naturally hydrous peridotite. They pointed out that the experiments probably suffered Fe loss to the Pt containers and thermocouple poisoning, leading to underestimation of run temperature. They compared their results to those of Green (1973) and Mysen & Boettcher (1972, 1973). The phase stability fields of Milhollen *et al.* (1974) broadly coincide with Green's (1973), but the 3 studies differ in their location of the solidus and amphibole stability boundary. They deduced that this was largely due to experimental problems and pointed out that "there has been no proof for attainment of a state of stable equilibrium in hypersolidus peridotite-H_2O experiments so far". The experimental problems of Fe loss, attainment of equilibrium and quench modification of melt stopped progress in the study of hydrous peridotite melting for nearly a decade. New techniques were developed, however, which minimised Fe loss and quench modification problems, and by the 1990s interest had resumed.

Kawamoto & Hirose (1994) showed that Fe loss to AuPd containers was <4% relative in wet basalt melting experiments, under relatively oxidising conditions (fO_2 = QFM+1). Quench modification problems could be avoided by pre-crimping of containers in peridotite melting experiments. Melt pools in the crimp and quenches to glass (Hirose & Kawamoto, 1995). Hirose & Kawamoto (1995) quantified the effect of H_2O on melting temperature, fraction and compostion for an H_2O-undersaturated peridotite at 1GPa. They concluded that melts with <2.5wt% H_2O have similar compositions to similar melt fractions in a dry system. Melts with >3wt% H_2O have increased SiO_2 and decreased MgO relative to similar melt fractions in a dry system. Attention refocussed on the possibility of generating primary andesitic melts. Hirose (1997) showed that at 1GPa, partial melts at low temperature (<1100°C) with high H_2O (≥6wt% i.e. saturated) are andesitic in composition.

Kushiro (1990) used the sandwich technique to run hydrous melting experiments at 1.2-2.0 GPa. Fe loss was minimised by using Pt containers pre-saturated with Fe (Grove, 1981). Results showed that at 1.2GPa, adding ≈5wt% H_2O causes a similar shift in melt composition to that caused by decreasing pressure from 1.2 to 0.8 GPa in a dry system. A second observation was that at constant temperature and pressure, increasing H_2O causes melt composition to become more SiO_2-rich which produces magnesian andesite (boninite) at $H_2O \geq 8$wt% in the melt.

Gaetani & Grove (1998) completed a study of the effects of varying H_2O content on melt composition at 1.2-2.0 GPa. They used Fe-saturated AuPd capsules, and high initial ratios of melt/peridotite material in a modified version of the sandwich technique. They argued that "andesitic" glasses (Kushiro, 1990; Hirose, 1997) only appear enriched in SiO_2 when recalculated on a volatile-free basis. On a hydrous basis, Gaetani & Grove's partial melts are SiO_2-depleted relative to dry melts at similar melt fractions. They suggested that the effect of H_2O on peridotite melting reactions is to decrease the contribution of clinopyroxene to the melt, through lowering the temperature of melting. Using isobaric batch melting calculations, they concluded that H_2O-undersaturated peridotite has a lower melt productivity compared to dry mantle.

In summary, early work in the 1960s and 1970s focussed on whether primary andesite magmas could be generated by the addition of H_2O to the mantle melting system. This gave qualitative information on hydrous peridotite melting, but was hampered by the same problems encountered in anhydrous mantle melting studies, i.e. Fe loss and quench modification. During the 1980s and 1990s, 2 solutions were found to each problem. Fe loss was minimised by using AuPd capsules, or by using Pt capsules pre-saturated with Fe. Quench modification was avoided by using the sandwich technique, or by pre-crimping the capsule to create a pooling area for the melt. Experimental studies resumed, and a reasonable number of data now exist on hydrous peridotite melting in the spinel lherzolite field (1-2GPa). The dataset on hydrous mantle melting is still very incomplete especially at small melt fractions and at higher pressures. These data are essential to understanding melting in the subduction zone mantle wedge, since it is believed to be a polybaric, near-fractional process and to originate at 100-120km depth in the garnet lherzolite field.

1.5 Anhydrous peridotite phase equilibria

Peridotite consists of 4 major mineral phases: olivine (ol), orthopyroxene (opx), clinopyroxene (cpx) and a minor aluminous phase (plagioclase feldspar (plag), spinel or garnet). During partial melting, the relative contributions of these four phases vary with the

pressure and temperature conditions. The phase equilibria of these four phases control the melt reaction and composition.

Peridotite phase equilibria have been determined experimentally by several workers. Estimated solidus temperature varies between studies, due to the use of different peridotite bulk compositions. The onset of melting in peridotite is sensitive to the Mg/Fe ratio, volatiles present and concentration of incompatible oxides *e.g.* Na_2O, K_2O (Hirose & Kushiro 1983; Fujii & Scarfe 1985; Falloon & Green 1988; Robinson *et al.*, 1998). Some commonly used peridotite compositions are shown in Table 1.2.

Table 1.1 Chemical composition of peridotites used in earlier experimental studies.

Name Studies used	KLB-1 Takahashi, 1986	HK-66 Takahashi & Kushiro, 1983	PHN-1611 Hirose & Kushiro, 1994	MPY-90 Green, 1979
SiO_2	44.48	48.02	43.70	45.2
TiO_2	0.16	0.22	0.25	0.7
Al_2O_3	3.59	4.88	2.75	3.5
Cr_2O_3	0.31	0.25	0.28	0.4
FeO*	8.10	9.90	8.81	8.0
MnO	0.12	0.14	0.13	0.1
NiO	0.25	n.d.	-	0.2
MgO	39.22	32.35	37.22	37.5
CaO	3.44	2.97	3.26	3.1
Na_2O	0.30	0.66	0.33	0.6
K_2O	0.02	0.07	0.14	0.13
Mg#[a]	89.6	85.3	88.3	89.3

* All Fe as Fe^{2+}.
[a] Mg# = 100* molar MgO/(MgO + FeO*).

The upper limit to the peridotite solidus can be taken from CMAS simple system studies (Presnall *et al.*, 1978). Figure 1.1 shows that the solidus extends from ≈1240°C at 1 atm to 1750°C at 5GPa, and is composed of 3 curves corresponding to the stability fields of plagioclase lherzolite (low pressure), spinel lherzolite (intermediate pressure) and garnet lherzolite (high pressure). The lower limit to the peridotite solidus can be taken from studies of fertile peridotite, *e.g.* HK66 (Takahashi & Kushiro, 1983). The solidus shows the same major features as in the CMAS system, but is depressed by ≈130°C and the cusps occur at 1.1 and 2.6 GPa. More refractory peridotites will have solidi intermediate to these bounds, e.g. KLB-1 has a solidus ≈50°C higher than HK66 (Takahashi, 1986; Scarfe et al 1979).

Figure 1.2 shows melting curves above the solidus for peridotite KLB-1 (Takahashi, 1986). These "out curves" mark the disappearance of the different mineral phases. The temperature and pressure of cpx-out is important for 2 reasons. Firstly, abyssal harzburgites, generated by partial melting of peridotite, are common (*e.g.* Michael & Bonatti, 1985), suggesting that conditions must have exceeded cpx-out during their

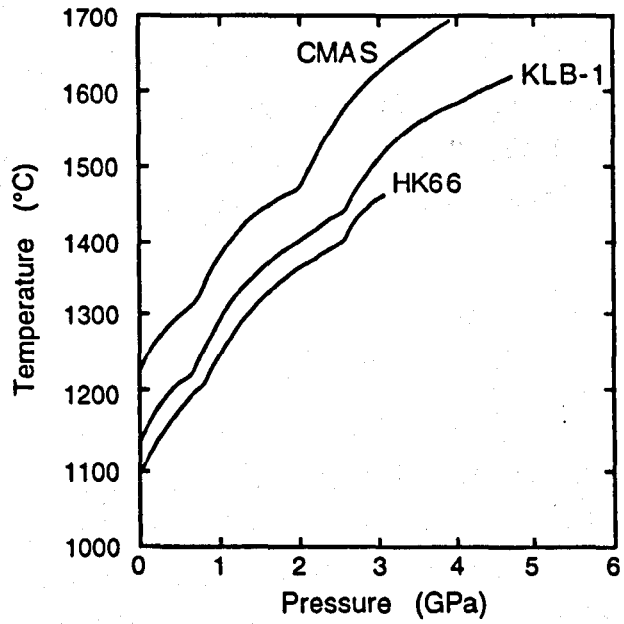

Figure 1.1 Solidi of the CMAS system and other peridotites. Peridotite compositions and data sources are shown in Table 1.2.

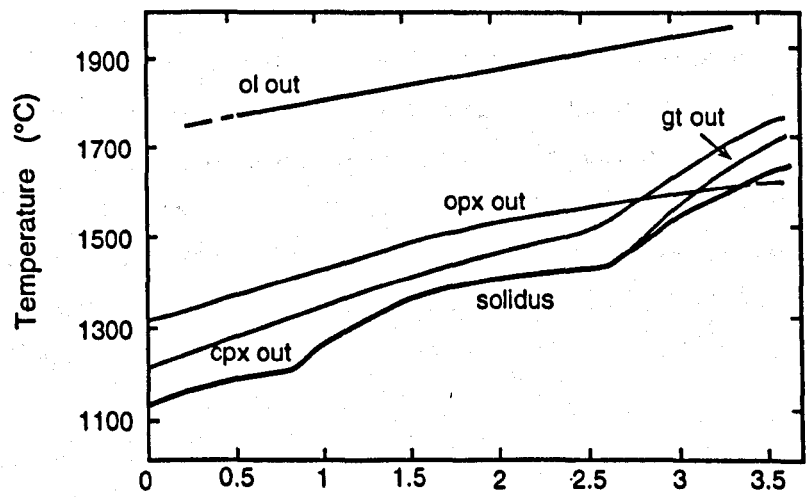

Figure 1.2 The melting phase relations of a typical peridotite KLB-1 up to 3.5GPa (after Takahashi, 1986). Ol, olivine; opx, orthopyroxene; cpx, clinopyroxene; gt, garnet.

genesis. Secondly, as cpx is eliminated, the peridotite residue composition becomes more refractory, rapidly increasing its solidus temperature so that melting is effectively ceased (Mysen & Kushiro, 1977). The location of cpx-out is sensitive to peridotite composition, being >100°C lower for fertile peridotite HK-66 (Takahashi & Kushiro, 1983) than for the more depleted composition of MORB-pyrolite (Falloon & Green, 1987). Similarly opx-out is also sensitive to peridotite composition, occurring at lower temperature in more fertile mantle.

1.6 Summary

The Earth's upper mantle is generally accepted to be predominantly composed of peridotite. Partial melting behaviour of the dry mantle is now well constrained by experimental data. Early conflicts in views were mainly the result of experimental and analytical problems, which have been overcome through the development of new techniques. Increased information has led to improvements in our understanding of how the mantle melts, and it is now considered a polybaric, near-fractional process. Recent work has shown that both the sandwich technique and the diamond aggregate technique are useful in simulating this process.

Several lines of evidence indicate that H_2O is an essential component in the mantle, and is strongly associated with subduction zone magmatism. By studying the phase equilibria of hydrous peridotite, we can provide a robust framework for mantle melting and processes. Experimental studies of hydrous mantle melting have advanced with the development of new techniques, and we now have a broad understanding of the general effects of H_2O on mantle melting. Data are still very sparse, however, especially at low degrees of partial melting and at higher pressures. Information on melting under these conditions is essential to the development of quantitative models of the hydrous mantle melting system and subduction zone processes.

CHAPTER 2

Iron and Water Loss using $Au_{80}Pd_{20}$ Sample Containers in Hydrous Fe-bearing Systems

Introduction

It is well-recognised that iron loss from experimental charges through alloying with noble metal containers can be significant (*e.g.* Ito & Kennedy, 1967; Green, 1976; Grove, 1981). Iron loss is a serious problem because it results in changing bulk composition and phase relations during the course of an experiment (*e.g.* Stern & Wyllie, 1975). This effect can generate severe disequilibrium among experimental products. Similar problems have been encountered with water loss from hydrous charges, due to diffusion of hydrogen or molecular water through the capsule wall (*e.g.* Patiño Douce and Beard, 1994). To conduct experiments in hydrous, water-undersaturated iron-bearing systems, a capsule configuration is needed that limits both iron loss and hydrogen diffusion through the capsule wall.

Kawamoto & Hirose (1994) reported that AuPd alloys are suitable materials for containing hydrous basaltic melts at 0.5-1.5GPa and 1100-1400°C. They demonstrated that FeO* (total iron as FeO) loss from hydrous basalts to $Au_{90}Pd_{10}$ and $Au_{75}Pd_{25}$ capsules is <4% relative after 24 hours. This figure agrees well with estimated iron loss to graphite-lined Pt capsules from anhydrous charges (*e.g.* Takahashi & Kushiro, 1983; Falloon & Green, 1988). Hirose & Kawamoto (1995) showed that use of AuPd alloys results in negligible H_2O loss from hydrous peridotite charges at 1GPa. Hydrogen loss was estimated to be ≈10% relative after 24-48 hours in $Au_{75}Pd_{25}$ capsules (Kawamoto, 1996).

Kawamoto & Hirose's (1994) data suggest that iron loss from silicate melt to AuPd capsules is dependent on oxygen fugacity (fO_2), with more reducing conditions increasing iron loss. Before AuPd containers can be used with any reliability, therefore, some understanding of the dependence of iron loss on oxidation state is required. In this study, experiments were conducted to test the effect of initial oxidation state on iron and water loss from hydrous, water-undersaturated basalts to $Au_{80}Pd_{20}$ capsules at 0.7-1GPa and 1300-1350°C. The results are compared with the behaviour of graphite-lined Pt capsules under similar conditions, and with the behaviour of $Au_{80}Pd_{20}$ capsules in hydrous, water-undersaturated peridotite melting experiments at 1.5GPa.

2.1 Experimental and analytical methods

2.1.1 Experimental methods

Experiments were conducted in an end-loaded, piston cylinder apparatus. Talc-pyrex outer sleeves were used in 3/4 inch diameter furnace assemblies with crushable alumina inner sleeves and a tapered graphite furnace. CaF_2 outer sleeves were used in 1/2 inch diameter furnace assemblies with crushable alumina inner sleeves and a parallel-sided graphite furnace. The hot piston-out method was used in all cases (Johannes *et al.*, 1971). Temperature was monitored and controlled to within ±1°C using a WRe_3/WRe_{25} (D-type) thermocouple. No correction for the effect of pressure on thermocouple e.m.f. was made. A pressure correction of -10% was used for the talc-pyrex assembly (Johannes *et al.*, 1971), and a pressure correction of -8% for the CaF_2 assembly, based on calibration of the quartz-albite-jadeite transition. Pressure was monitored and controlled to within ±0.05GPa using a Heise gauge. The temperature gradient close to the centre of the furnace within the assemblies is ≈3°C mm^{-1} based on calibrations using 2 thermocouples (H. Soulard, pers. comm.)

Starting mixes were prepared by grinding high-purity oxides (SiO_2, TiO_2, Al_2O_3, Fe_2O_3, Cr_2O_3 and MgO) and carbonates (Na_2CO_3 and $CaCO_3$) under ethanol in an agate mortar. The mixtures were decarbonated at 1000°C in air, ground and reduced in a CO/CO_2 gas-mixing furnace at 1000°C at known fO_2. This was either 1 l.u. below the quartz-fayalite-magnetite (QFM) buffer at 1atm ("QFM-1 mixes") or 1 l.u. above the QFM buffer at 1atm ("QFM+1 mixes"). The mixtures were then reground under ethanol until the grain size was ≤30μm. At this stage, H_2O was added as $Mg(OH)_2$, and the mixes were ground and subsequently stored at 120°C prior to use. The compositions of all starting mixes were verified by fusing in a graphite crucible in air at 1000°C, and subsequent electron microprobe analysis (see section 2.1.2). The analysed starting compositions, with nominal H_2O contents, are shown in Table 2.1.

Three capsule configurations were used. The first consisted of a welded 2mm outside diameter (O.D.) $Au_{80}Pd_{20}$ capsule inside a 3mm O.D. Pt capsule (see Figure 2.1). The reason for using a double capsule was that single AuPd capsules were observed to deform and rupture occasionally during the experiment. Starting mix was packed into both the inner AuPd capsule and the outer Pt capsule. Only run products within the inner capsule were subsequently analysed. The second capsule configuration used was similar to the first but incorporated a high-purity graphite liner within the inner AuPd capsule. The third capsule configuration is a welded 3mm O.D. Pt capsule that contained a high purity graphite liner which holds the starting mix.

Table 2.1 Compositions and initial oxidation state of starting mixes for hydrous basalt melting experiments.

Mix	L-2	L-12	L-13	L-4a	L-5	vn1
Initial fO_2[a]	QFM-1	QFM-1	QFM-1	QFM+1	QFM+1	QFM+1
SiO_2	48.75[24]	46.79[18]	44.00[32]	48.46[23]	47.22[39]	48.74[29]
TiO_2	0.57[4]	0.83[3]	1.21[2]	0.90[1]	0.75[1]	0.75[2]
Al_2O_3	18.72[26]	11.91[20]	13.17[10]	16.55[7]	17.74[11]	16.83[14]
FeO*	6.01[31]	9.61[20]	11.99[19]	5.59[13]	4.13[14]	6.72[32]
MgO	11.51[11]	17.06[14]	16.34[12]	13.85[10]	18.51[10]	12.30[11]
CaO	11.94[9]	11.44[8]	10.65[6]	12.43[5]	7.52[7]	10.95[6]
Na_2O	2.19[3][c]	2.25[4]	2.60[3]	1.89[3]	4.43[4]	3.31[5]
H_2O[b]	1.69	5	5.0	2.5	4.96	5

* All Fe as Fe^{2+}.
[a] fO_2 relative to the quartz-fayalite-magnetite (QFM) buffer at 1000°C, 1atm.
[b] Nominal water content (wt%).
[c] All analyses are given in wt% on an anhydrous basis. Values in square brackets represent 2 standard errors of the analysed compositional range in terms of least units cited,
e.g. 2.19[3] should read 2.19 ± 0.03.

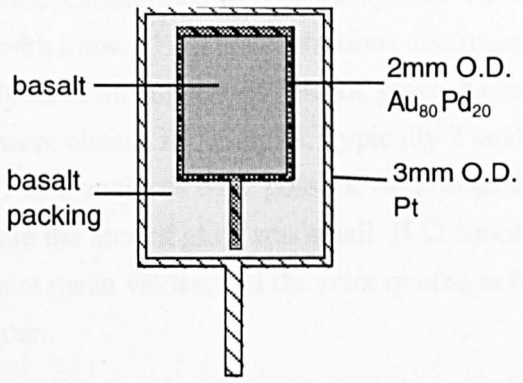

Figure 2.1 Section through $Au_{80}Pd_{20}$-Pt double capsule configuration.

In all cases, the capsule assembly was contained in a crushable alumina sleeve packed with fine alumina powder. The capsule was placed in the furnace hotspot and protected from thermocouple intrusion by a 0.5mm thick Pt disc. Some experiments incorporated a small piece of Pt foil in the charge, in order to obtain an estimate of fO_2 using the method described by van der Laan and van Groos (1991). Experiments were quenched by switching off the power supply. Initial quench rates were ≈300°C s^{-1} for CaF_2 assemblies and slightly slower for talc-pyrex assemblies.

2.1.2 Analytical methods

After quenching, capsules were extracted, mounted in Petropoxy™ resin, sectioned longitudinally and polished to a 0.1μm finish. All phases were analysed at the University of Bristol using a four-spectrometer Jeol JXA-8600 electron microprobe in wavelength dispersive mode with a 15 keV accelerating voltage and 15nA beam current. Crystalline

phases were analysed using a 1μm spot and glasses were analysed using with the beam rastered over an area of approximately 10μm x 15μm, in order to limit alkali migration. Data were recorded and corrected using ZAF procedures.

H_2O concentrations in the glasses were analysed by SIMS using the Cameca ims-4f in the Department of Geology and Geophysics, University of Edinburgh. A primary beam of O^- ions was accelerated at 10keV, and the secondary beam at 4.5keV. $^1H^+$ and ^{30}Si ion beams were measured with an electron multiplier, using an energy offset of -100±24eV to suppress isobaric molecular overlaps and minimize matix effects. Spot size was 15-25μm. ^1H and ^{30}Si ions were measured over 40 cycles, and the mean $^1H/^{30}Si$ ratio was calculated using only the beam counts measured over the last 10 cycles. To convert $^1H/^{30}Si$ data to values for H_2O concentration, calibrations were made against repeated analyses of 2 hydrous basaltic glasses with known H_2O concentrations determined by FTIR methods, and against repeated analyses of an anhydrous basaltic glass. Areas of glass that were free of cracks and inclusions were chosen for analysis. Typically 3 analyses were carried out per sample, though only 1 or 2 analyses were possible on glasses in some peridotite melting experiments, where the area of glass was small. H_2O concentrations given in Tables 2.2 and 2.3 represent mean values, and the error quoted in brackets afterwards represents 2 standard errors.

H_2O concentrations in some of the glasses were also analysed by infrared (IR) spectroscopy using a Nicolet 800 FTIR spectrometer at the University of Bristol. An unpolarised IR beam was used with a KBr or CaF_2 beamsplitter and a globar or visible source (respectively), with a liquid nitrogen cooled HgCdTe detector attached to a microscope. The microscope was enclosed in a nitrogen-purged chamber to ensure low, constant atmospheric H_2O levels. Samples mounted in epoxy resin were doubly polished, and sample thicknesses were measured to within ±1μm using an electronic micrometer. Areas of glass that were free of cracks and inclusions were chosen for analysis. A 100μm spot size with redundant aperturing was used. Spectra were acquired at a resolution of 4 wavenumbers. Baselines were fitted by eye: more complicated baseline-fitting procedures were not found to change estimated H_2O concentrations significantly. Values for molar absorptivities for basaltic glass were taken from Dixon *et al.* (1995).

2.2 Results

Run conditions, phase assemblages and glass compositions are reported in Tables 2.2 and 2.3. High FeO* loss (4-23% relative) is observed in all experiments containing Pt

Table 2.2 Experimental conditions and analyses for hydrous basalt melting experiments in Pt-$Au_{80}Pd_{20}$ double capsules.

Experiment	10QFM1	10QFM2	10QFM3	CFC[a]	CFD[a]	Leo12
Pressure cell[b]	CaF_2	CaF_2	CaF_2	CaF_2	CaF_2	CaF_2
Sample	L-12	L-12	L-12	L-2	L-2	L-12
Temperature (°C)	1300	1300	1300	1300	1300	1350
Pressure (GPa)	1	1	1	1	1	0.7
Duration (hrs)	24	24	24	24	24	0.5
Phases[c]	gl	gl	gl	gl	gl	gl
Initial fO_2[d]	QFM-1	QFM-1	QFM-1	QFM-1	QFM-1	QFM-1
Initial FeO* (wt%)	9.61[20][h]	9.61[20]	9.61[20]	6.01[34]	6.01[34]	9.61[20]
Initial H_2O[e] (wt%)	5	5	5	1.69	1.69	5
Final fO_2[f]				QFM-1	QFM-2	
Final FeO* (wt%)	9.60[7]	8.54[3]	9.41[4]	5.11[10]	5.75[10]	9.45[9]
Final H_2O (wt%)	3.78[27]	3.85[11]	4.20[20]	1.10[10]	1.07[11]	3.21[51]
FeO* loss[g] (rel.%)	0.1[22]	-11.1[21]	-2.1[21]	-15.0[59]	-4.3[59]	-1.7[22]
H_2O loss[g] (rel.%)	-24.5[54]	-23.1[22]	-16.1[39]	-35.2[62]	-36.4[67]	-35.9[102]
Experiment	Leo13	vn1	TPB	TPE[a]	CFA	CFB[a]
Pressure cell[b]	CaF_2	T	T	T	CaF_2	CaF_2
Sample	L-13	vn1	L-4a	L-4a	L-5	L-4a
Temperature (°C)	1350	1330	1350	1330	1300	1300
Pressure (GPa)	0.7	1	1	1	1	1
Duration (hrs)	0.5	0.5	24	24	24	24
Phases[c]	gl	gl	gl,cpx,sp	gl,cpx,sp	gl	gl
Initial fO_2[d]	QFM-1	QFM+1	QFM+1	QFM+1	QFM+1	QFM+1
Initial FeO* (wt%)	11.99[19]	6.72[32]	5.59[13]	5.59[13]	4.13[14]	5.59[13]
Initial H_2O[e] (wt%)	5	5	2.5	2.5	4.96	2.5
Final fO_2[f]				QFM+2		n.a.
Final FeO* (wt%)	12.04[10]	7.00[14]	5.36[12]	4.99[5]	4.33[14]	4.38[16]
Final H_2O (wt%)	2.54[5]	4.47[24]	1.91[17]	2.18[12]	4.35[8]	2.86[41]
FeO* loss[g] (rel.%)	+0.4[11]	+4.2[52]	-4.1[32]	-10.7[25]	+4.8[48]	-21.6[37]
H_2O loss[g] (rel.%)	-49.2[11]	-10.7[48]	-23.6[67]	-12.8[48]	-12.3[16]	+14.2[163]

* All Fe as Fe^{2+}.
n.a. not analysed
[a] Charge contained Pt foil in order to estimate fO_2 during the experiment.
[b] T = talc-pyrex.
[c] gl, glass; cpx, clinopyroxene; sp, spinel.
[d] fO_2 relative to the quartz-fayalite-magnetite (QFM) buffer at 1000°C, 1atm.
[e] Nominal water content.
[f] fO_2 relative to the QFM buffer under run conditions. fO_2 estimated on the basis of Fe exchange between Pt foil and melt (O'Neill, 1987; Holloway *et al.*, 1992).
[g] +, FeO* or H_2O gain; -, FeO* or H_2O loss.
[h] All analyses are given in wt% on an anhydrous basis. Values in square brackets represent 2 standard errors of the analysed compositional range in terms of least units cited, *e.g.* 9.61[20] should read 9.61± 0.20

foil, irrespective of capsule configuration. This is due to Fe alloying with the foil and is not an indication of FeO* loss to the capsule. All errrors quoted are 2 standards errors on the mean.

2.2.1 $Au_{80}Pd_{20}$-Pt capsules

FeO* loss is generally ≤4% relative from hydrous basalts to $Au_{80}Pd_{20}$-Pt double capsules, both from QFM-1 mixes and from QFM+1 mixes. In one experiment (10QFM2) FeO* loss is 11.1% relative (discussed in section 3.1). Experiments using $Au_{80}Pd_{20}$-Pt double capsules show very variable relative H_2O loss. Mean relative H_2O loss is 27.0±7.7% from QFM-1 mixes and 8.6±14.4% from QFM+1 mixes, after 24

Table 2.3 Experimental conditions and analyses for hydrous basalt melting experiments in graphite-lined Pt capsules and $Au_{80}Pd_{20}$-Pt double capsules.

Experiment	C2	C3	C4	C5	CGP	TPA1	TPA2
Capsule	Pt	Pt	Pt	Pt	AuPd-Pt	Pt	Pt
Pressure cell[a]	CaF_2	CaF_2	CaF_2	CaF_2	CaF_2	T	T
Sample	L-2	L-2	L-2	L-2	L-2	L-4a	L-4a
Temperature (°C)	1300	1300	1300	1300	1300	1330	1330
Pressure (GPa)	1	1	1	1	1	1	1
Duration (hrs)	24	24	24	24	24	24	24
Phases	glass	glass	glass	glass	glass	glass	glass
Initial fO_2[b]	QFM-1	QFM-1	QFM-1	QFM-1	QFM-1	QFM+1	QFM+1
Initial FeO* (wt%)	6.01[34]	6.01[34]	6.01[34]	6.01[34]	6.01[34]	5.59[13]	5.59[13]
Initial H_2O[c] (wt%)	1.69	1.69	1.69	1.69	1.69	2.5	2.5
Final fO_2[d]		QFM-4					QFM-5
Final FeO* (wt%)	6.06[34]	n.a.	6.08[18]	6.40[6]	6.40[15]	5.46[22]	4.32[11]
Final H_2O (wt%)	1.39[6]	n.a.	0.99[8]	0.71[9]	0.72[11]	0.33[4]	0.31[5]
FeO* loss[e] (rel.%)	+0.8[80]	n.a.	+1.2[64]	+6.5[57]	+6.5[62]	-2.3[46]	-22.7[30]
H_2O loss[e] (rel.%)	-17.5[37]	n.a.	-41.5[46]	-57.8[51]	-57.6[63]	-86.7[17]	-88[14]

* All Fe as Fe^{2+}.

n.a. not analysed

[a] T = talc-pyrex.

[b] fO_2 relative to the quartz-fayalite-magnetite (QFM) buffer at 1000°C, 1atm.

[c] Nominal water content.

[d] fO_2 relative to the QFM buffer under run conditions. fO2 estimated on the basis of Fe exchange between Pt foil and melt (Holloway *et al*, 1992; O'Neill, 1987).

[e] +, FeO* or H_2O gain; -, FeO* or H_2O loss.

[f] Values in square brackets represent 2 standard errors of the analysed compositional range in terms of least units cited, *e.g.* 6.01[34] should read 6.01±0.34.

hours. H_2O loss does not appear to be related to the duration of the experiment.

In experiments containing Pt foil, fO_2 can be estimated on the basis of iron exchange between the foil and the melt (O'Neill, 1987; Holloway *et al.*, 1992). In $Au_{80}Pd_{20}$-Pt double capsules, fO_2 during the experiment appeared to remain within 1 l.u. of the initial fO_2 of the starting mixes.

2.2.2 Graphite-lined Pt and $Au_{80}Pd_{20}$-Pt capsules

Graphite-lined Pt experiments show no measurable FeO* loss (within error) after 24 hours at 1GPa and 1300-1350°C. These results are consistent with previous work (Takahashi & Kushiro, 1983; Falloon & Green, 1988; Holloway *et al.*, 1992, Robinson *et al.*, 1998), and confirm that graphite linings can minimise iron loss to Pt capsules. Using a graphite-lined $Au_{80}Pd_{20}$-Pt double capsule (experiment CGP1), no FeO* loss occurred. H_2O loss in experiments using graphite-lined capsules is significant and very variable with a mean value of 52.2±22.6% relative, after 24 hours.

The measured fO_2 within graphite liners is equivalent to 4-5 l.u. below the QFM buffer at 1330°C. This is below CCO and below IW at 1GPa, but no C or native Fe formed. Likely that true fO2 has been underestimated in calculation and is close to CCO buffer (QFM-2).

2.3 Discussion

2.3.1 FeO* loss to $Au_{80}Pd_{20}$

My results show that FeO* loss to AuPd alloys under hydrous conditions is generally ≤4% relative. Higher FeO* loss (11% relative) was observed in one experiment (10QFM2). Experiments conducted under identical conditions (10QFM1 and 10QFM3) show minimal FeO* loss, suggesting that the high FeO* loss in 10QFM2 is unrelated to run conditions. Kawamoto & Hirose (1994) showed that FeO* loss to AuPd capsules is dependent on the composition of the alloy used. Small-scale variations in the composition of the $Au_{80}Pd_{20}$ alloy used in experiment 10QFM2 could have made it more susceptible to FeO* loss. Alternatively a small puncture may have developed in the capsule during the experiment, not visible in the analysed polished section, which allowed diffusion of Fe into the outer Pt capsule.

Results in this study show that FeO* loss to AuPd alloys under hydrous conditions is not sensitive to fO_2, for initial oxidation states ranging from QFM-1 to QFM+1. Kawamoto & Hirose (1994) suggested that FeO* loss to AuPd containers is dependent on oxidation conditions within the capsule. They observed that FeO* loss to AuPd was greater from hydrous mixes at 1-1.5GPa than from the same mixes under anhydrous conditions. They speculated that this resulted from more oxidising conditions and lower Fe activity in the hydrous mixes. My results indicate that in Kawamoto & Hirose's (1994) experiments, fO_2 in the hydrous and anhydrous mixes must have differed by more than 2 l.u. for its effect on iron activity to be significant. Other explanations for the observed variation in Fe loss between experiments might be heterogeneities in FeO* of the natural starting mixes used, or in the composition of the AuPd alloy used.

Results using a graphite-lined $Au_{80}Pd_{20}$ capsule suggest that FeO* loss from hydrous basalts can be minimal at 1GPa, 1300°C. Gaetani & Grove (1998), however, observed siginificant iron loss (≈38% relative) to graphite-lined $Au_{80}Pd_{20}$ capsules at 1.6GPa. Iron loss to graphite-lined AuPd capsules is likely be variable, depending on initial Fe^{3+}/FeO^*, H_2O and CO_2 content (Holloway *et al.*, 1992).

2.3.2 H_2O loss using $Au_{80}Pd_{20}$ capsules

Results show that H_2O loss from hydrous basalts using $Au_{80}Pd_{20}$ capsules is highly variable, but that a correlation exists with initial oxidation state of the starting mix. On average, H_2O loss is lower from more oxidised starting mixes than from more reduced ones. H_2O loss occurs due to diffusion of H_2 through the capsule wall (Grashoff *et al.*, 1983), following dissociation of H_2O by the reaction:

$$H_2O = H_2 + 1/2\ O_2$$

In an iron-bearing system, O_2 is consumed by the oxidation of Fe^{2+} by the reaction:

$$2FeO + 1/2\ O_2 = Fe_2O_3$$

Using a relatively oxidised starting mix, the initial Fe^{3+}/Fe^{2+} ratio is higher and the activity of FeO is decreased. H_2O loss is greater in experiments using graphite-lined Pt and $Au_{80}Pd_{20}$ capsules, since O_2 is consumed by reaction with the graphite (Holloway *et al.*, 1992):

$$C_{(graphite)} + O_2 = CO_2$$

$$CO_2 + O^{2-}_{(melt)} = CO_3^{2-}{}_{(melt)}$$

Patiño Douce & Beard (1994) suggested that H_2O loss also occurs from charges by diffusion of molecular H_2O through the capsule, in addition to H_2 diffusion. It is possible that differing amounts of H_2O diffusion could explain the wide range in H_2O loss observed in experiments conducted under identical conditions. Few, if any, data are available on H_2O diffusivity in noble metals, but the process will be driven by a chemical gradient in H_2O activity across the capsule wall. Differences in the amount of H_2O diffusion between experiments might be caused by variation in H_2O activity in the run assembly outside the $Au_{80}Pd_{20}$-Pt double capsule. This could be minimised by heating the run assembly at 100°C before commencing the experiment to ensure no adsorbed H_2O is present. H_2O diffusivity through $Au_{80}Pd_{20}$ is also likely to be affected by the number of diffusive pathways available for a large gaseous species such as H_2O. This might vary between capsules, due to heterogeneity in the microcrystalline structure of the $Au_{80}Pd_{20}$ alloy that developed either during manufacture or during annealing (Patiño Douce & Beard, 1984).

2.3.3 H_2O loss in peridotite melting experiments

Mean H_2O loss using double Pt-$Au_{80}Pd_{20}$ capsules in peridotite melting experiments is <3% relative (see section 3.1.3). Bulk H_2O concentration in the peridotite melting experiments reported in this study was generally <2wt%, and H_2O loss may have been minimised by low H_2O activity in the charge. A hydrous basaltic powder containing ≈5wt% H_2O was used to pack between the inner AuPd and outer Pt capsule in the peridotite melting experiment surrounding the $Au_{80}Pd_{20}$ capsules. This may have decreased outward diffusion of H_2O through the $Au_{80}Pd_{20}$ capsule by preventing the development of steep gradients in H_2O activity between the charge and the outer run assembly.

2.4 Conclusions

FeO* loss to $Au_{80}Pd_{20}$ from hydrous basalt is generally ≤4% relative at 0.7-1GPa and 1300-1330°C. FeO* loss is not sensitive to initial oxidation state, for starting mixes with a range in fO_2 equivalent to QFM+1 to QFM-1. H_2O loss from hydrous basalts in $Au_{80}Pd_{20}$ capsules is very variable, but in general, H_2O loss is higher in more reduced starting mixes. Mean H_2O loss is 27.0±7.7% relative after 24 hours from starting mixes initially reduced at fO_2 equivalent to QFM-1. Mean H_2O loss is 8.6±14.4% relative after 24 hours from starting mixes initially reduced at fO_2 equivalent to QFM+1.

$Au_{80}Pd_{20}$ is a suitable capsule material to prevent FeO* loss during hydrous basalt and peridotite melting experiments. H_2O loss can occur from hydrous basalt contained in $Au_{80}Pd_{20}$ capsules, but this can be minimised by using a starting mix that has been initially reduced to an fO_2 greater than QFM+1 at 1atm. Use of a hydrous basalt powder as a packing material around the $Au_{80}Pd_{20}$ capsule may help to prevent outward diffusion of H_2O from the capsule.

FeO* loss from hydrous basalts contained in graphite-lined Pt capsules is negligible at 1GPa, 1300-1350°C. H_2O loss in these experiments is variable and high with mean value of 52.2±22.6% relative. Graphite-lined AuPd-Pt and Pt capsules are not suitable for hydrous, water-undersaturated, basalt melting experiments, since H_2O will be lost from the charge.

CHAPTER 3

The Effect of H_2O on Peridotite Melting at 1.5GPa

Introduction

H_2O has a significant effect on partial melting of peridotite. Addition of H_2O forms hydrous minerals in the peridotite, lowers the temperature of melting and increases the olivine and clinopyroxene (cpx) liquidus volumes at the expense of orthopyroxene (opx) (Kushiro, 1972; Gaetani & Grove, 1998). H_2O is an essential component which facilitates mantle melting in subduction zones. Theoretical, experimental and geochemical studies indicate that mantle melting is a fractional rather than a batch melting process (e.g. McKenzie, 1984; Johnson *et al.*, 1990; Iwamori, 1993), and that melt may segregate from the solid residue at melt fractions of ≈1% by volume (McKenzie, 1984). Our understanding of mantle melting in subduction zones is hampered by a lack of quantitative data on the effect of H_2O on peridotite melting temperature and liquid composition, especially at small melt fractions.

I have conducted experiments at 1.5GPa to simulate partial melting of hydrous peridotite in the subduction zone environment at melt fractions ranging from <1wt% to >30wt%. 1.5GPa was selected as it represents a reasonable minimum depth of melting in the mantle wedge. I have used a Au-Pd-Pt double capsule design, that has been demonstrated to minimise Fe loss and H_2O loss under relatively oxidising conditions (see Chapter 2). Experiments were conducted using the sandwich technique, since this can be used successfully to study partial melting over a range of melt fractions (Robinson *et al.*, 1998), without engendering problems of polybaric melt accumulation (Falloon *et al.*, 1998).

Peridotite in subduction zones appears to be enriched in a component consisting mainly of H_2O, Na_2O and K_2O (Stolper & Newman, 1994; Gaetani & Grove, 1998). I have chosen to investigate one "end-member" composition of the subduction component (H_2O+Na_2O), in order to limit the number of variables in the melting system. The peridotite composition used (Leo3) is shown in Table 3.1. Leo3 is a fertile spinel lherzolite with 0.5wt% H_2O and high Na_2O content (0.64wt%). To investigate the effect of H_2O on partial melting of spinel lherzolite at 1.5GPa, I will compare my results to those of a study on anhydrous peridotite MPY (Robinson *et al.*, 1998). The composition of MPY, given in Table 3.1, is lower in Na_2O than Leo3 and is slightly less fertile.

3.1 Experimental and analytical methods

3.1.1 Experimental methods

Starting mixes were prepared by grinding analytical grade oxides (SiO_2, TiO_2, Al_2O_3, Fe_2O_3, Cr_2O_3, MnO and MgO) and carbonates (Na_2CO_3 and $CaCO_3$) under ethanol in an agate mortar. The mixtures were decarbonated at 1000°C in air, reground and reduced in a CO/CO_2 gas-mixing furnace at 1000°C at known fO_2 as follows. The peridotitic starting mix used was reduced at an fO_2 equivalent to 1 log unit (l.u.) below the quartz-fayalite-magnetite buffer (QFM-1). This was chosen as a reasonable lower limit to oxidation conditions in a subduction zone mantle at a depth equivalent to 1.5GPa (Wood *et al.*, 1990; Ballhaus,1992). Basaltic starting mixes were reduced at an fO_2 equivalent to 1 l.u. above the QFM buffer (QFM+1). Relatively oxidised basaltic mixtures were used to minimise H_2O loss from the charge (see Chapter 2). The mixtures were ground under ethanol until the grain size was ≤30μm. H_2O was added to starting mixes Leo3, Leo4 and vn1 as $Mg(OH)_2$, and to starting mixes vn5 and vn8, as $Mg(OH)_2$ and $Al(OH)_3$. The mixes were then re-ground and subsequently stored at 120°C prior to use. The compositions of all basaltic starting mixes were verified by fusing mixes at 1GPa, 1300°C, using a double Au-Pd-Pt capsule and run durations of 30mins. The resulting crystal-free glasses were analysed by electron microprobe. H_2O contents in mixes vn5 and Leo4 were verified using SIMS methods (see section 3.1.2). The composition of Leo3 was verified by XRF methods at the University of Edinburgh. The analysed starting compositions are shown in Table 3.1.

Table 3.1 Starting compositions used in experimental studies at 1.5GPa (all analyses are recalculated to 100wt%).

	Leo3[a]	Leo4[b]	VN1[b]	VN5[b]	VN8[b]	MPY[c]
SiO_2	43.30	47.39	46.45	46.33	48.16	45.9
TiO_2	0.18	0.88	0.73	1.16	0.8	0.17
Al_2O_3	4.57	16.18	16.54	19.52	19.27	4.65
Cr_2O_3	0.46	0.32	0.09	0.00	0.07	0.57
FeO*	8.19	5.47	6.67	4.64	6.05	6.15
MnO	0.00	0.2	0.03	0.08	0.09	0
MgO	38.81	13.55	11.80	4.66	4.88	38.4
CaO	3.37	12.16	10.16	8.11	6.8	3.61
Na_2O	0.64	1.85	2.92	3.48	5.19	0.5
H_2O	0.50[d]	2.20	4.60[e]	12.02[d]	8.69[d]	0
Mg*	0.89	0.82	0.76	0.64	0.59	0.89

[a] XRF analysis.
[b] Probe analysis.
[c] Robinson *et al.*, 1998.
[d] Nominal H_2O content (wt%).
[e] H_2O content measured by SIMS methods (wt%).

Experiments were conducted in an end-loaded, solid media piston cylinder apparatus. CaF_2 outer sleeves were used in 1/2 inch diameter assemblies with crushable alumina inner sleeves and a graphite furnace. An $Au_{80}Pd_{20}$-Pt double capsule (see Figure 2.1) was

used to minimise Fe and H_2O loss from the charge. The capsule was protected from thermocouple intrusion by a 0.5mm thick Pt disc.

The hot piston-out method was used in all cases (Johannes *et al.*, 1971). Temperature was monitored and controlled to within ±1°C using a WRe_3/WRe_{25} (D-type) thermocouple. No correction for the effect of pressure on thermocouple e.m.f. was made. A pressure correction of -8% for the CaF_2 assembly, based on calibration of the quartz-albite-jadeite transition, was applied. Pressure was monitored and controlled to within ±0.05GPa using a Heise gauge. The temperature gradient close to the centre of the furnace within the assemblies is ≈3°C mm^{-1} based on calibrations using 2 thermocouples (H. Soulard, pers. comm.) At the end of each run, experiments were quenched at initial rates of ≈300°C s^{-1}. Experimental run conditions are given in Table 3.2.

Table 3.2 Experimental run conditions at 1.5GPa.

Experiment	T[a] (°C)	Duration (h)	Basalt used	wt% basalt	F[b] (wt%)	Phases present[c]
VN1100	1100	33	VN5	19	[d]	ol,opx,cpx,amph
VN1085	1085	32	VN5	19.3	0.7 ± 1.8	ol,opx,cpx,sp,amph,gl
VN1130-10	1130	28	VN8	9.55	2.5 ± 2.0	ol,opx,cpx,sp,amph,qm
VN1130	1130	27	VN8	19.7	8.0 ± 1.0	ol,opx,cpx,sp,qm
VN1145	1145	30	VN1	23.1	6.1 ± 0.8	ol,opx,cpx,sp,qm
VN1150	1150	30.5	VN1	20	8.6 ± 1.2	ol,opx,cpx,sp,qm
VN1160	1160	30.5	VN1	22.7	18.1 ± 1.0	ol,opx,cpx,sp,gl
VN1175	1175	28	VN1	19.5	15.8 ± 1.0	ol,opx,cpx,sp,gl
VN1190	1187	30.5	VN1	17.5	23.8 ± 0.4	ol,opx,sp,gl
VN1205	1213	32	VN1	15.3	23.8 ± 0.4	ol,opx,sp,gl
VN1220	1229	30	VN1	17.3	25.5 ± 0.4	ol,opx,sp,gl
VN1235	1240	30	VN1	19.4	26.9 ± 0.2	ol,opx,sp,gl
VN1240	1252	29.5	VN1	22.6	26.1 ± 0.2	ol,opx,sp,gl
VN1250	1256	30	Leo4	17.9	22.9 ± 0.4	ol,opx,sp,gl
VN1260	1269	31	Leo4	21.3	22.1 ± 0.4	ol,opx,sp,gl
VN1270	1279	30	Leo4	14.2	28 ± 0.4	ol,opx,sp,gl
VN1275	1275	28	VN1	23.7	27.5 ± 0.2	ol,opx,sp,gl
VN1290	1298	30	Leo4	12.6	30 ± 0.6	ol,opx,sp,gl
VN1300	1306	48	Leo4	12.6	27.6 ± 0.4	ol,opx,sp,gl
VN1319	1331	27	Leo4	15.5	31.9 ± 0.4	ol,opx,sp,gl

[a] Temperatures reported have been corrected for small variations in sample geometry using a thermal gradient of 3°C/mm, calibrated using 2 thermocouples (H. Soulard, pers. comm.).
[b] Melt fraction and 2 standard errors. See Appendix 4 for derivation.
[c] ol, olivine; opx, orthopyroxene; cpx, clinopyroxene; sp, spinel; amph, amphibole; gl, glass; qm, quench mat of crystals and interstitial glass.
[d] Subsolidus.

3.1.2 Analytical methods

After quenching, capsules were extracted, mounted in Petropoxy™ resin, sectioned longitudinally and polished to a 0.1μm finish. In all experiments at ≥ 1175°C and in the experiment at 1085°C, the liquid quenched to a glass. In experiments at 1130-1160°C, the liquid quenched to a mat of feathery cpx and/or amphibole crystals with interstitial glass.

All phases were analysed at the University of Bristol using a four-spectrometer Jeol JXA-8600 electron microprobe in wavelength dispersive mode with a 15 keV accelerating voltage. Crystal phases were analysed using a 1μm spot and 15nA beam current. Glasses generated at ≥1190°C were analysed using a 10μm spot and 15nA beam current to limit alkali migration. Quenched liquids in lower temperature experiments were analysed using a rastered beam at 75 000x magnification and a 3nA beam current. This was found to be the most effective method to limit alkali migration, when Na_2O content of the melt was relatively high. Data were recorded and corrected using ZAF procedures.

H_2O concentrations in the glasses were analysed by SIMS using the Cameca ims-4f in the Department of Geology and Geophysics, University of Edinburgh. A primary beam of O- ions was accelerated at 10keV, and the secondary beam at 4.5keV. $^1H^+$ and ^{30}Si ion beams were measured with an electron multiplier, using an energy offset of -100 ± 24eV to suppress isobaric molecular overlaps and minimise matrix effects. Spot size was 15-25μm. ^1H and ^{30}Si ions were measured over 40 cycles, and the mean $^1H/^{30}Si$ ratio was calculated using only the beam counts measured over the last 10 cycles. This was in order to avoid measurement of H_2O adsorbed on the sample surface. To convert $^1H/^{30}Si$ data to values for H_2O concentration, calibrations were made against repeated analyses of 2 hydrous basaltic glasses with known H_2O concentrations determined by FTIR methods, and against repeated analyses of an anhydrous basaltic glass. Areas of glass that were free of cracks and inclusions were chosen for analysis. Typically 3 analyses were carried out per sample. H_2O concentrations given in Table 3.3 are mean values.

In some experiments (see Table 3.3) H_2O in the liquid could not be measured directly, either because the area of glass was too small, or because the liquid quenched to a mat of crystals and interstitial melt. In such cases, theoretical H_2O concentrations in the glasses were estimated by mass balance, using the bulk H_2O added to the charge and the proportion of liquid formed in the charge (see Appendix 1). Theoretical melt H_2O contents were adjusted for estimated H_2O loss. To test the accuracy of estimating melt H_2O by mass balance, theoretical and measured H_2O concentrations are compared for glasses analysed by SIMS (see Table 3.4). Results agree within 2 standard errors for experiments at ≤1240°C. In experiments at >1240°C, melt H_2O is underestimated by 0.75±0.2wt% (25-30% relative) using mass balance methods. Several factors could have contributed to this, *e.g* Leo4 has slightly higher actual H_2O than the nominal value or slightly higher Fe_2O_3/FeO^* than was assumed.

3.1.3 H_2O loss

Estimation of H_2O loss was based on the assumption that all H_2O loss occurs due to H_2 loss from the charge and accompanying Fe oxidation. H_2O loss (or gain) is therefore

Table 3.3 H_2O content of melt and peridotite, and estimated H_2O loss in experiments at 1.5GPa.

Experiment	H_2O analysis method[a]	Melt H_2O[b,c] (wt%)	Peridotite H_2O[b] (wt%)	H_2O gain/loss[d] (relative %)
VN1100	t	[e]	0.34 ± 0.13[f]	2.99 ± 0.41
VN1085	t	18.79 ± 1.91	0.23 ± 2.57[g]	-11.35 ± 0.30
VN1130-10	t	13.26 ± 3.07	0.39 ± 0.91[g]	-9.63 ± 0.69
VN1130	t	9.45 ± 1.32	0.76 ± 0.17	-5.49 ± 0.80
VN1145	t	9.29 ± 1.31	0.57 ± 0.19	-8.32 ± 1.01
VN1150	t	10.99 ± 3.30	0.95 ± 0.33	-6.10 ± 4.01
VN1160	t	4.29 ± 0.23	0.78 ± 0.08	1.66 ± 0.10
VN1175	SIMS	5.05 ± 0.70	0.80 ± 0.15	2.01 ± 0.83
VN1190	SIMS	3.24 ± 0.22	0.78 ± 0.08	-3.83 ± 1.67
VN1205	SIMS	3.54 ± 0.17	0.85 ± 0.06	-2.84 ± 1.10
VN1220	SIMS	3.73 ± 0.22	0.97 ± 0.06	3.28 ± 0.42
VN1235	SIMS	3.17 ± 0.17	0.86 ± 0.05	-4.14 ± 0.71
VN1240	SIMS	3.40 ± 0.16	0.88 ± 0.05	-4.59 ± 0.83
VN1250	SIMS	2.34 ± 0.12	0.54 ± 0.05	0.85 ± 2.04
VN1260	t	2.00 ± 0.09	0.44 ± 0.05	1.71 ± 0.84
VN1270	SIMS	2.71 ± 0.14	0.76 ± 0.05	4.40 ± 1.20
VN1275	t	3.32 ± 0.09	0.93 ± 0.03	-7.13 ± 2.05
VN1290	SIMS	2.78 ± 0.21	0.83 ± 0.08	4.69 ± 1.98
VN1300	SIMS	2.47 ± 0.14	0.69 ± 0.06	-5.04 ± 2.02
VN1319	t	1.61 ± 0.10	0.52 ± 0.07	-6.31 ± 1.95

[a] SIMS, measured directly using Secondary Ion Mass Spectroscopy; t, theoretical estimate based on mass balance of H_2O_3. See Appendix 1 for derivation.
[b] H_2O content and 2 standard errors.
[c] Theoretical H_2O contents have been adjusted for estimated H_2O loss.
[d] Estimated H_2O loss and 2 standard errors. See Appendix 3 for derivation. Positive value indicates a relative gain in H_2O, negative value indicates a relative loss in H_2O.
[e] Subsolidus.
[f] Estimate based on amphibole H_2O content. See Appendix 2 for full discussion.
[g] Estimate based on melt and amphibole H_2O content. See Appendix 2 for full discussion

Table 3.4 Comparison of measured and theoretical melt H_2O in glasses at 1.5GPa.

Experiment	Measured melt H_2O[a]	Theoretical melt H_2O[b]
VN1175	5.05 ± 0.68	4.41 ± 0.16
VN1190	3.24 ± 0.23	3.18 ± 0.07
VN1205	3.54 ± 0.17	3.12 ± 0.06
VN1220	3.73 ± 0.21	3.30 ± 0.07
VN1235	3.17 ± 0.17	3.28 ± 0.05
VN1240	3.40 ± 0.16	3.37 ± 0.05
VN1250	2.34 ± 0.11	1.88 ± 0.08
VN1270	2.71 ± 0.13	1.91 ± 0.07
VN1290	2.78 ± 0.20	1.75 ± 0.12
VN1300	2.47 ± 0.14	1.76 ± 0.08

[a] H_2O content and 2 standard errors, measured using SIMS method.
[b] H_2O content and 2 standard errors, based on estimate by mass balance.

directly proportional to change in Fe_2O_3 in the bulk composition of the charge during the experiment. Change in Fe_2O_3 was estimated by mass balance (see Appendix 2). Estimations of H_2O loss (in relative %) for all experiments are shown in Table 3.3.

Change in H_2O ranges from a gain of 1.66% relative to a loss of 11.35% relative. Mean H_2O loss for all experiments is 3.0 ± 2.2% relative. In experiments with melt H_2O contents <5wt%, mean H_2O loss is lower (1.1 ± 1.1% relative). H_2O loss is greater for the lower temperature experiments with melt H_2O contents greater than 5wt%, with a mean value of 8.18 ± 2.18% relative.

3.1.4 Peridotite H_2O

During a sandwich experiment, H_2O will be exchanged between melt in the peridotite layer and melt in the basalt layer until equilibrium is established. The H_2O content of the melt at the end of the experiment depends not only on the initial H_2O content of the peridotite starting mix, but also on the H_2O content of the basalt starting mix. The peridotite H_2O content required to produce the final melt H_2O content can be estimated using the H_2O content of the melt and the degree of melting in the peridotite (see Appendix 4). Estimations of peridotite H_2O content for all experiments are given in Table 3.3.

H_2O saturation of Leo3

In the subsolidus state, H_2O saturation of a peridotite defines the maximum H_2O content that can be stored in the equilibrium crystalline phases without the formation of a separate fluid phase. This depends on the abundance and identity of H_2O-bearing minerals present. The proportion of hydrous minerals formed will depend on the bulk composition of the peridotite. The principal H_2O-bearing phase in Leo3 at 1.5GPa is pargasitic amphibole, with an H_2O content of ≈1.9wt% based on stoichiometry. The maximum proportion of amphibole that can exist subsolidus in Leo3 will be constrained most strongly by Na_2O content of the peridotite. Assuming that all Na_2O is used in forming amphibole, then the maximum subsolidus proportion of amphibole in Leo3 is estimated as ≈20% (assuming Na_2O amphibole = 3.2wt% as analysed in 1100B, and Na_2O Leo3 = 0.64wt%). As a rough estimate, an upper limit on the H_2O content of Leo3 at saturation is therefore ≈0.4wt%. This is in good agreement with previous estimates of amphibole peridotite H_2O saturation (Tatsumi, 1989; Schmidt & Poli, 1997). The estimated subsolidus amphibole content of Leo3 is decreased if Na_2O partitioning into cpx in taken into account. The jadeite ($NaAlSi_2O_6$) component of cpx is decreased in the presence of amphibole (Helz, 1982), however, and the proportion of cpx in the peridotite melting residue is decreased by the reaction of amphibole formation (Olafsson & Eggler, 1994; Sisson *et al.*, 1997). A saturation limit of 0.4wt% H_2O in Leo3 is, therefore, a reasonable approximation.

3.1.5 fO_2

The oxygen fugacity (fO_2) in these runs has been estimated using 2 methods. The first method estimates fO_2 from Fe_2O_3/FeO* (total iron) ratios required for agreement between olivine-melt molar FeO-MgO distribution coefficients and values predicted using Ulmer's (1989) model. fO_2 is calculated from the Fe_2O_3/FeO* ratios in the glasses using the expression of Kress & Carmichael (1991). The second method calculates fO_2 based on ol-opx-sp thermobarometry (Nell & Wood, 1989; Wood, 1990). Fe^{3+} in spinel was estimated from stoichiometry (3 cations). Results are shown in Table 3.5. Values of fO_2 are quoted relative to the QFM buffer at the experimental run temperature. Estimated values of fO_2 using the 2 methods agree to within 0.6 ± 0.3 l.u. The estimated range in fO_2 (based on an average of the 2 sets of values) is QFM+2.2 to QFM+7.8. The melts have increased in fO_2 by 1-6.6 l.u.

Table 3.5 Oxygen fugacity (fO_2) in experiments at 1.5GPa

Experiment	T[a] (°C)	fO_2[b] ol-m[c]	ol-opx-sp[d]
VN1085	1085	8.65	7
VN1130-10	1130	4.10	3.50
VN1130	1130	3.85	3.2
VN1145	1145	4.05	3.3
VN1150	1150	3.65	3.1
VN1160	1160	1.7	0
VN1175	1175	1.6	0.8
VN1190	1187	2.95	2.5
VN1205	1213	2.35	2.1
VN1220	1229	0.75	0.1
VN1235	1240	2.45	1.5
VN1240	1252	3.35	2.4
VN1250	1256	1.85	0.7
VN1260	1269	1.65	0.7
VN1270	1279	1.2	0.2
VN1275	1275	2.8	2.3
VN1290	1298	1.35	0.4
VN1300	1306	2.6	2
VN1319	1331	2.4	1.9

[a] Temperatures reported have been corrected for small variations in sample geometry using a thermal gradient of 3°C/mm, calibrated using 2 thermocouples (H. Soulard, pers. comm.).
[b] fO_2 (log units) relative to the QFM buffer at run temperature and 1.5GPa, and 2 standard errors.
[c] fO_2 estimated using the expression of Kress & Carmichael (1991). Fe^{3+}/FeO* values used are given in Table 3.6.
d fO_2 estimated by thermobarometry methods using olivine-orthopyroxene-spinel Mg-Fe equilibria (Nell & Wood; 1989; Wood, 1990)

3.2 Approach to equilibrium

All experiments were run for over 24 hrs to achieve effectively constant liquid composition (Kushiro, 1990; Hirose & Kushiro, 1995). In experiments where the liquid quenched to a glass, microprobe analysis shows that, within error, the glasses are homogenous in composition.

Olivine crystals show no evidence of zoning and have a constant composition throughout the charge. Spinel crystals are too small for zoning to be detectable. Subsolidus

experiments demonstrate, however, that spinels generally achieve equilibrium on the same timescale as olivine (Wood, 1990). Spinels in these experiments therefore are also assumed to have equilibrated with the liquid.

Orthpyroxene and clinopyroxene crystals are zoned in all these experiments. This is a well-documented phenomenon (*e.g.* Takahashi & Kushiro, 1983; Baker & Stolper, 1994; Walter & Presnall, 1994), and it has been shown that pyroxene crystals rarely homogenise in complex systems, even after 200 hrs. Zoned clinopyroxenes in peridotite are made up of 3 distinct zones, as discussed in Robinson *et al.* (1998):

(i) A disequilibrium metastable core with a composition related to that of the starting materials.

(ii) A rim which was in equilibrium with the liquid before quenching. The thickness of the rim depends on experimental duration.

(iii) An outer quench rim in direct contact with the glass, commonly non-stoichiometric.

Figure 3.1 illustrates how the compositions of the 3 parts can be identified. All pyroxene analyses obtained from 1 experiment are plotted using Ca^{2+} and Al^{3+} contents recalculated on a 6 oxygen basis. The co-existing equilibrium liquid is plotted on the same basis. Cpx analyses show a trend from core to equilibrium rim of increasing Ca^{2+} and Al^{3+}. Opx analyses show a trend from core to equilibrium rim of increasing Al^{3+}, but little change in Ca^{2+}. For both pyroxenes, quench rim analyses form a second trend away from the equilibrium rim composition towards that of the co- existing liquid. The equilibrium rim pyroxene compositions can therefore be identified as those where the core-rim and the quench-rim trends intersect.

Amphiboles do not show strong zoning in these experiments, but do have a narrow quench rim.Quench rim analyses can be identified on the basis of higher Ca^{2+} and Al^{3+} contents than equilibrium compositions.

3.3 Degree of Partial Melting

Using the sandwich method, the amount of melt in the capsule will always be greater than the amount that would be produced by direct melting of the parent peridotite. The degree

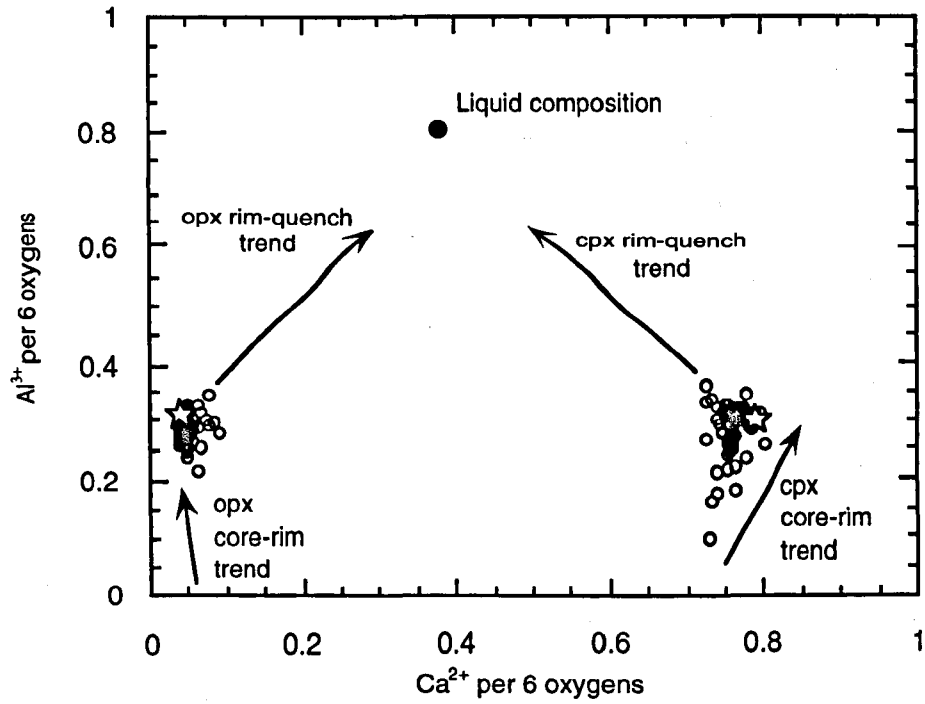

Figure 3.1 Covariation of Al^{3+} per 6 oxygens with Ca^{2+} per 6 oxygens of all stoichiometric pyroxene analyses from a single experiment (vn1150). The liquid composition is also plotted on a 6 oxygen basis. Cpx analyses show a trend from core to equilibrium rim of increasing Ca^{2+} and Al^{3+}. Opx analyses show a trend from core to equilibrium rim of increasing Al. Quench pyroxene compositions form a trend from the equilibrium rim composition towards that of the co-existing liquid. Equilibrium rim pyroxene compositions (shown by star) are those where the core-rim and quench-rim trends intersect.

of melting therefore cannot be estimated by point counting the phase proportions or by simple mass balance methods. Instead the degree of partial melting in these experiments is estimated by a more complex, 2-stage mass balance method (see Appendix 4), based on the methodology of Robinson *et al.* (1998). Their work has shown that this method is accurate provided the melt composition does not change greatly during the experiment. Results are presented in Table 3.2.

Experiment 1100B is identified as subsolidus on textural grounds. The peridotite part of the charge consists of anhedral, interlocking crystals and contains no interstitial melt (or material quenched from melt) at grain boundaries. The basalt layer contains pockets of glass, isolated from the peridotite layer by a mantle of cpx and amphibole crystals.

3.3.1 Degree of melting as a function of temperature

Melt fraction (F) is plotted against temperature in Figure 3.2. Temperature uncertainty for the piston cylinder apparatus at Bristol University is ±10-15°C (Robinson *et al.*, 1998),

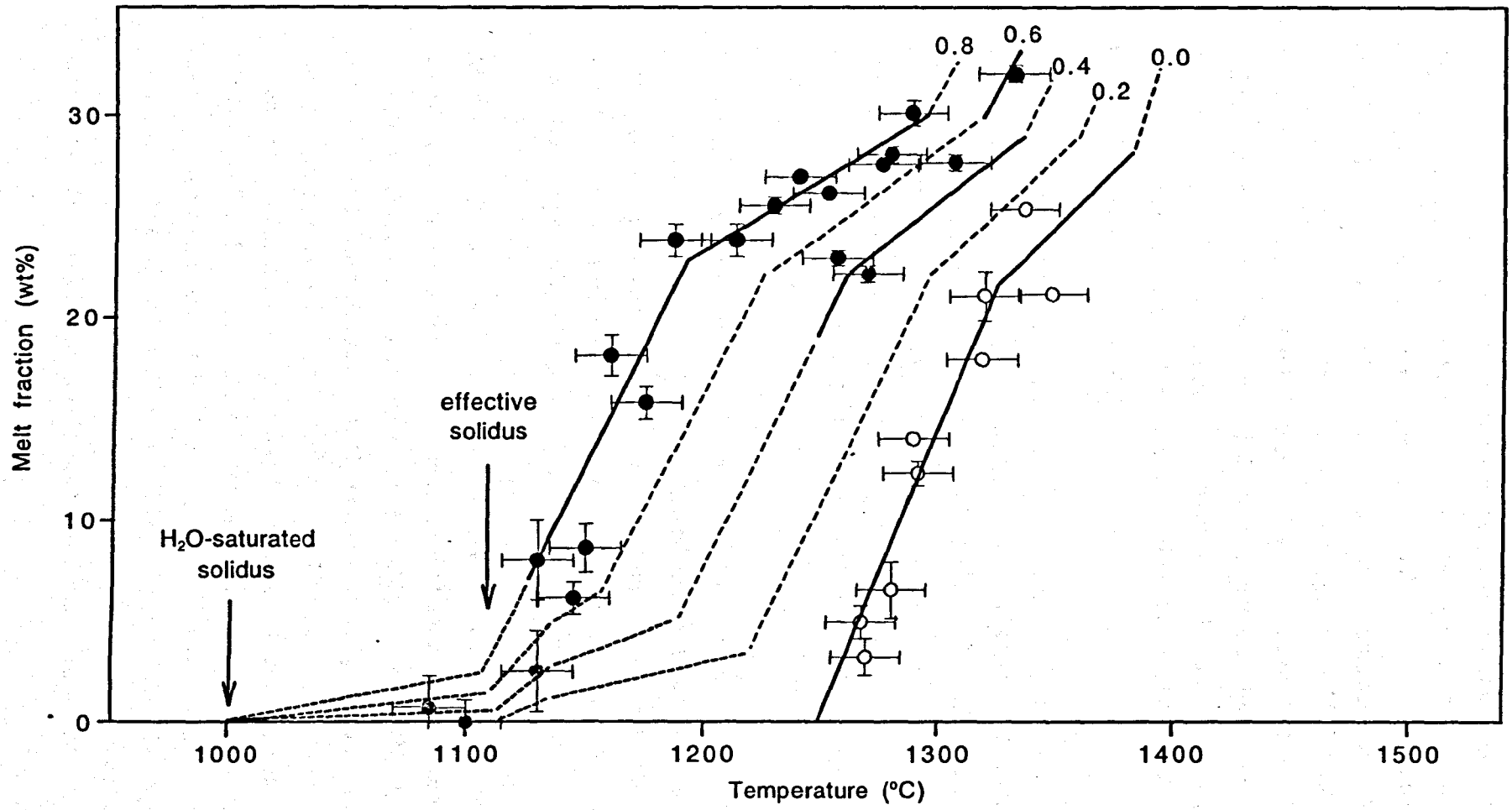

Figure 3.2 Degree of melting as a function of temperature and peridotite H_2O content at 1.5GPa. Contour values show peridotite H_2O in wt%. Broken lines indicate approximate location of contour. Pale grey circles = Leo3 + 0.3-0.49wt% H_2O, dark grey circles = Leo3 + 0.5-0.69wt% H_2O, black circles = Leo3 + ≥0.7wt% H_2O, open circles = anhydrous equivalent of Leo3 (estimated using data for peridotite MPY (Robinson et al), see text for details). Error bars for melt fraction are 2 standard errors.

based on reproducibility of melt composition in sandwich experiments (Robinson *et al.*, 1998). Contours show estimated H_2O content in the peridotite. Data for partial melting of Leo3 under anhydrous conditions has been estimated for comparison. For simplicity it was assumed that, at a given temperature, change in peridotite bulk composition affects the degree of melting, but does not affect (i) the composition of the melt and solid phases produced or (ii) the relative abundances of the solid phases. Degree of melting in anhydrous Leo3 was estimated by the two-stage mass balance method (Appendix 4), using phase composition data for partial melting of peridotite MPY (Robinson *et al.*, 1998). For each experiment in Robinson *et al.*'s study, the relative abundances of the solid phases were estimated by mass balance of all phase compositions with the bulk composition of MPY. Degree of melting in anhydrous Leo3 at the same temperature was estimated by mass balancing all phase compositions and solid phase relative abundances to the bulk composition of Leo3.

Adding H_2O to peridotite lowers the temperature of melting. At F>8wt%, the decrease in temperature is directly proportional to the amount of H_2O added. At F=8-20wt% in Leo3, the decrease in temperature is of the order of 18°C per 0.1wt% H_2O, *e.g.* to generate an anhydrous melt fraction of 18wt% requires a temperature of 1310°C, but with 0.8wt% H_2O the same melt fraction is generated at 1160°C, and with 0.4wt% H_2O at 1240°C. At larger melt fractions, the effect of H_2O on temperature of melting is diminished due to dilution.

The trend in F with temperature in hydrous peridotite is very similar to that for anhydrous peridotite, except at small melt fractions. At moderate melt fractions, F increases relatively rapidly (≈1% per 4°C) until cpx is eliminated from the peridotite melting residue (cpx-out). This occurs at similar melt fraction (F=20-22%) irrespective of peridotite H_2O content, being primarily a function of peridotite bulk composition.

At smaller melt fractions, the effect of H_2O on peridotite melting is more complex and is strongly controlled by amphibole stability. For H_2O-undersaturated Leo3, melting starts at ≈1100°C. This corresponds to the onset of amphibole melting (Niida & Green, 1999), and agrees well with estimates of the H_2O-undersaturated peridotite solidus in previous studies (Green, 1976; Olafsson & Eggler, 1994; Niida & Green, 1999). Melting is expected to start at this temperature for all peridotite H_2O contents below saturation (≈0.4wt% H_2O in Leo3, as discussed in section 3.1.4). For H_2O contents above saturation, melting is expected to start at the H_2O-saturated solidus, ≈1000°C (Kushiro, 1970; Green, 1973; Milhollen *et al.*, 1974). Above the H_2O-saturated solidus, F is expected to increase very slowly with temperature, as amphibole stability increases with decreasing H_2O activity in the melt (Holloway, 1973). For both saturated and undersaturated peridotite,

rapid increase in F is expected over a small temperature interval (10-15°C) once amphibole starts to melt at 1100±50°C (Niida & Green, 1999). This temperature bracket can therefore be considered as the "effective" hydrous peridotite solidus. The precise temperature of amphibole melting will depend on peridotite and amphibole bulk composition (Niida & Green, 1999). Conditions in experiment VN1085 are observed to be supra-solidus at 1085°C. This suggests that the peridotite H_2O content must be ≥ 0.4wt%, which appears reasonable given large error brackets on estimated peridotite H_2O. Once amphibole has been eliminated, F is expected to increase more slowly until cpx melting becomes significant. At small F in anhydrous peridotite, F increases at the same rapid rate (≈1% per 4°C) from the solidus until cpx is eliminated.

3.4 Solid phase equilibria and composition

Solid phase compositions are given in Table 3.6.

3.4.1 Olivine

Apparent Mg-Fe partition coefficients for olivine and melt (apparent $K_D^{Mg\text{-}Fe}$ ol-m) are calculated as:

$$\text{apparent } K_D^{Mg\text{-}Fe} \text{ ol-m} = (MgO/FeO^*)_{melt} / (MgO/FeO^*)_{olivine}$$

assuming all Fe to be Fe^{2+}.

Values for apparent $K_D^{Mg\text{-}Fe}$ ol-m are given in Table 3.6. Apparent $K_D^{Mg\text{-}Fe}$ ol-m generally ranges from 0.13-0.26, except for the lowest temperature experiment. These values are lower than those predicted for $K_D^{Mg\text{-}Fe}$ ol-m at 1.5GPa (0.337± 0.004) by Ulmer (1989). This is due to the presence of Fe^{3+} in the melt, under the relatively oxidising conditions of these experiments (fO_2>QFM+2). Apparent $K_D^{Mg\text{-}Fe}$ ol-m shows a strong correlation with estimated fO_2 in the experiments (see Figure 3.3a). Values for apparent $K_D^{Mg\text{-}Fe}$ ol-m in hydrous and anhydrous melts under more reducing conditions are close to Ulmer's predicted value (Gaetani & Grove, 1998; Robinson *et al.*, 1998).

$K_D^{Mg\text{-}Fe}$ ol-m decreases with decreasing melt fraction, as shown in Figure 3.3b. This corresponds to increased Fe^{3+} in the melt at smaller melt fractions. This trend is also observed in anhydrous melts at 1.5GPa (Robinson *et al.*, 1998), and suggests that Fe^{3+} isbehaving as an incompatible element. Na_2O increases in the melt with decreasing melt fraction (see section 3.5.1), and may also contribute to stabilising a greater proportion of

Table 3.6 Experimental phase compositions produced at 1.5GPa

Experiment	Phase[a]	No.[b]	Na_2O	MgO	SiO_2	Al_2O_3	CaO	TiO_2	FeO*	Cr_2O_3	MnO	Mg#[c]	Total[d]	K_D[e]	Fe_2O_3/FeO*[f]
vn151100B	Ol	37	0.01[1][f]	51.17[13]	41.20[9]	0.13[6]	0.16[2]	0.00[0]	7.26[8]	0.06[2]	0.09[2]	0.93	99.91		
	Opx	2	0.10[6]	32.38[34]	52.35[31]	7.93[19]	0.89[7]	0.09[5]	5.98[12]	0.28[11]	0.07[4]	0.91	99.52		
	Cpx	4	0.81[6]	16.62[113]	49.58[58]	7.16[19]	20.43[19]	0.93[1]	4.08[31]	0.39[2]	0.03[7]	0.88	99.33		
	Amph	36	3.20[2]	19.41[8]	44.42[11]	15.48[9]	11.34[4]	0.73[2]	4.75[18]	0.65[6]	0.06[1]	0.88	95.95		
vn151085	Liq	10	5.38[10]	5.98[6]	56.07[24]	19.77[16]	7.43[10]	1.03[6]	4.30[28]	0.03[4]	0.12[8]	0.71	87.78	0.80	0.07
	Ol	18	0.02[2]	54.27[86]	42.43[54]	0.33[20]	0.25[8]	0.01[0]	2.61[24]	0.03[2]	0.12[4]	0.97	99.07		
	Opx	5	0.04[2]	34.13[16]	52.51[11]	6.61[6]	0.84	0.15[3]	5.41[2]	0.16[4]	0.18[5]	0.92	98.71		
	Cpx	2	0.98[4]	15.06[10]	48.61[4]	6.87[13]	21.51[20]	0.49[3]	6.19[26]	0.26[5]	0.11[3]	0.81	93.45		
	Spinel	12	0.04[2]	19.60[60]	0.27[13]	24.46[330]	0.20[16]	0.53[32]	52.54[26]	2.25[5]	0.25[3]	0.40	98.41		0.88
	Amph	37	3.34[7]	18.83[28]	43.77[40]	14.31[28]	11.30[16]	0.97[11]	7.21[23]	0.22[8]	0.09[4]	0.81	95.51		
vn1130-10	Liq	4	4.70[8]	7.98[44]	50.76[226]	19.81[132]	9.22[74]	0.70[2]	6.70[22]	0.04[2]	0.18[0]	0.68	85.96	0.60	0.14
	Ol	31	0.02[2]	52.08[56]	41.62[28]	0.10[10]	0.18[6]	0.00[0]	5.93[14]	0.03[2]	0.11[4]	0.94	100.25		
	Opx	2	0.13[32]	31.87[108]	52.40[72]	7.29[7]	1.23[2]	0.14[1]	6.28[19]	0.56[30]	0.13[6]	0.90	99.62		
	Cpx	3	1.38[3]	15.30[10]	49.49[52]	7.04[12]	19.78[5]	0.34[2]	6.50[13]	0.17[2]	0.05[0]	0.40	94.62		
	Spinel	12	0.03[2]	17.62[18]	0.35[16]	30.13[80]	0.14[4]	0.48[2]	46.88[86]	4.26[38]	0.17[4]	0.81	99.08		0.78
	Amph	24	3.58[8]	18.63[24]	43.68[24]	14.78[14]	10.55[12]	0.77[4]	7.75[16]	0.24[5]	0.06[3]	0.40	96.37		
vn1130	Liq	122	4.60[26]	8.63[78]	50.99[78]	19.22[48]	8.73[28]	0.71[6]	7.06[48]	0.05[4]	0.11[8]	0.69	87.01	0.15	0.57
	Ol	69	0.02[2]	51.95[22]	41.50[20]	0.08[8]	0.14[4]	0.00[0]	6.22[18]	0.04[4]	0.12[4]	0.94	99.79		
	Opx	4	0.18[8]	32.35[56]	52.36[12]	7.35[5]	1.13[18]	0.13[2]	6.40[90]	0.13[4]	0.09[2]	0.90	99.50		
	Cpx	4	1.38[7]	14.91[32]	49.42[30]	7.48[40]	19.76[10]	0.33[3]	6.53[13]	0.15[1]	0.10[2]	0.43	94.24		
	Spinel	15	0.01[1]	18.04[18]	0.22[11]	34.72[76]	0.10[5]	0.43[2]	42.99[90]	3.40[36]	0.16[4]	0.80	98.28		0.77
vn1145	Liq	16	3.77[14]	8.70[78]	49.58[62]	20.29[36]	9.21[24]	1.06[6]	7.38[38]	0.07[4]	0.10[4]	0.68	87.55	0.13	0.60
	Ol	44	0.02[0]	52.26[16]	41.31[16]	0.21[8]	0.18[4]	0.00[0]	5.95[6]	0.04[2]	0.11[2]	0.94	98.37		
	Opx	6	0.13[4]	32.51[31]	53.02[30]	6.49[7]	1.21[9]	0.09[2]	6.04[19]	0.40[11]	0.13[4]	0.91	98.22		
	Cpx	3	1.17[36]	15.25[15]	49.36[30]	7.49[49]	20.31[6]	0.42[6]	5.79[18]	0.19[10]	0.04[8]	0.82	94.65		
	Spinel	9	0.02[2]	16.94[374]	0.17[2]	33.85[82]	0.07[3]	0.52[2]	40.67[67]	4.49[55]	1.28[60]	0.43	97.87		0.76

Table 3.6 (continued)

Experiment	Phase	No.	Na_2O	MgO	SiO_2	Al_2O_3	CaO	TiO_2	FeO*	Cr_2O_3	MnO	Mg#	Total	K_D	Fe_2O_3/FeO^*
vn1150	Liq	5	3.26[14]	9.95[76]	48.82[66]	19.17[86]	9.93[28]	1.14[8]	7.74[80]	0.02[2]	0.07[6]	0.70	88.41	0.15	0.55
	Ol	48	0.02[0]	52.39[14]	41.18[10]	0.11[4]	0.12[2]	0.01[0]	6.13[6]	0.02[0]	0.11[2]	0.94	100.38		
	Opx	4	0.15[4[	31.90[30]	52.29[30]	7.18[30]	1.60[54]	0.17[4]	6.52[28]	0.16[4]	0.09[4]	0.90	99.62		
	Cpx	3	1.08[3]	15.79[10]	49.06[16]	7.23[11]	20.04[17]	0.35[8]	6.12[19]	0.27[8]	0.07[8]	0.84	95.60		
	Spinel	6	0.01[1]	19.17[16]	0.15[6]	37.78[47]	0.08[2]	0.46[3]	37.20[51]	5.17[41]	0.10[5]	0.50	98.21		0.76
vn1160	Liq	14	3.01[10]	9.70[62]	48.99[40]	19.18[22]	10.94[28]	0.95[4]	7.15[26]	0.10[4]	0.12[6]	0.71	87.21	0.22	0.35
	Ol	14	0.02[0]	50.46[18]	41.23[8]	0.04[2]	0.13[0]	0.00[0]	8.09[10]	0.04[2]	0.08[2]	0.92	100.18		
	Opx	3	0.13[4]	31.69[28]	52.56[22]	7.58[18]	1.30[6]	0.14[1]	6.34[26]	0.20[1]	0.10[2]	0.90	100.05		
	Cpx	3	0.85[8]	16.49	49.55	7.27	20.60	0.30	4.49	0.46	0.03	0.87	97.26		
	Spinel	10	0.02[8]	21.10[26]	0.26[19]	52.41[7]	0.07[6]	0.17[2]	17.22[16]	8.77[13]	0.04[3]	0.69	95.35		0.53
vn1175	Liq	9	3.04[22]	11.35[14]	48.05[22]	18.03[8]	10.56[22]	1.01[4]	7.91[22]	0.05[4]	0.14[8]	0.72	88.45	0.22	0.34
	Ol	20	0.01[0]	50.86[14]	41.02[12]	0.04[2]	0.17[4]	0.00[0]	7.86[8]	0.04[2]	0.09[2]	0.92	99.54		
	Opx	2	0.13[9]	31.63[172]	53.03[88]	6.92[50]	1.61[52]	0.11[6]	6.18[38]	0.36[15]	0.07[6]	0.90	98.09		
	Cpx	4	0.90[5]	16.21[13]	49.76[48]	7.44[23]	19.65[28]	0.33[5]	5.23[23]	0.45[7]	0.06[6]	0.84			
	Spinel	12	0.03[2]	20.80[23]	0.29[15]	50.31[74]	0.09[3]	0.20[1]	19.97[30]	8.27[67]	0.11[4]	0.66	98.55		0.60
vn1190	Liq	8	2.70[4]	12.08[8]	47.81[10]	16.60[10]	10.57[26]	0.73[4]	8.55[14]	0.05[2]	0.10[4]	0.72	93.62	0.18	0.47
	Ol	56	0.02[0]	51.86[8]	41.24[6]	0.10[2]	0.17[0]	0.00[0]	6.57[4]	0.04[0]	0.08[2]	0.93	99.86		
	Opx	5	0.17[1]	30.50[38]	52.94[32]	7.26[28]	2.19[29]	0.12[4]	6.34[40]	0.44[10]	0.08[5]	0.90	98.99		
	Spinel	10	0.02[2]	19.34[21]	0.16[2]	35.47[125]	0.07[1]	0.24[2]	30.51[35]	14.16[116]	0.09[3]	0.53	96.80		0.74
vn1205	Liq	5	2.64[6]	12.75[30]	47.75[40]	16.11[28]	10.94[16]	0.83[4]	8.81[24]	0.12[4]	0.13[4]	0.72	92.73	0.20	0.42
	Ol	52	0.02[0]	51.49[12]	41.14[8]	0.13[4]	0.20[2]	0.00[0]	6.99[4]	0.04[0]	0.08[2]	0.93	100.10		
	Opx	5	0.25[8]	30.42[42]	52.29[14]	7.14[28]	2.71[44]	0.14[5]	6.51[9]	0.48[4]	0.08[6]	0.89	99.11		
	Spinel	10	0.03[2]	19.89[15]	0.22[2]	39.92[67]	0.13[4]	0.25[2]	27.94[2]	11.60[72]	0.08[4]	0.56	97.50		0.72
vn1220	Liq	15	2.55[4]	12.45[8]	49.11[38]	16.88[10]	10.97[18]	0.73[2]	7.23[18]	0.08[2]	0.06[2]	0.75	91.10	0.26	0.24
	Ol	50	0.01[0]	51.22[8]	40.81[12]	0.09[2]	0.19[0]	0.00[0]	7.62[4]	0.06[2]	0.09[2]	0.92	99.20		
	Opx	3	0.07[4]	32.08[38]	52.60[89]	6.95[54]	1.77[7]	0.11[5]	5.86[30]	0.51[5]	0.11[4]	0.91	98.47		
	Spinel	7	0.02[1]	20.48[86]	0.80[76]	42.56[100]	0.11[5]	0.18[1]	17.11[32]	18.63[141]	0.15[9]	0.68	98.10		0.53

Table 3.6 (continued)

Experiment	Phase	No.	Na_2O	MgO	SiO_2	Al_2O_3	CaO	TiO_2	FeO*	Cr_2O_3	MnO	Mg#	Total	K_D	Fe_2O_3/FeO^*
vn1235	Liq	9	2.29[4]	13.78[10]	47.73[18]	15.30[4]	11.46[8]	0.66[2]	8.69[6]	0.01[4]	0.11[2]	0.74	92.92	0.20	0.40
	Ol	45	0.02[0]	51.34[10]	41.72[6]	0.09[2]	0.21[0]	0.00[0]	6.59[6]	0.05[2]	0.07[2]	0.93	99.44		
	Opx	5	0.08[2]	31.88[25]	52.86[38]	7.09[17]	1.75[4]	0.09[2]	5.73[23]	0.49[6]	0.07[6]	0.91	99.00		
	Spinel	5	0.02[3]	20.16[100]	0.89[33]	36.58[117]	0.18[7]	0.20[2]	22.30[34]	19.63[158]	0.12[2]	0.62	97.49		0.66
vn1240	Liq	11	2.63[2]	12.86[8]	47.95[6]	16.05[8]	10.77[6]	0.76[2]	8.98[14]	0.07[2]	0.05[2]	0.72	91.57	0.17	0.50
	Ol	52	0.03[0]	52.11[12]	41.35[8]	0.14[4]	0.21[2]	0.00[0]	6.11[4]	0.05[2]	0.09[2]	0.94	98.61		
	Opx	3	0.07[5]	32.70[13]	53.42[18]	5.66[13]	1.57[6]	0.07[5]	5.85[12]	0.61[6]	0.07[8]	0.91	98.08		
	Spinel	6	0.02[2]	18.97[14]	0.26[6]	30.26[69]	0.18[8]	0.23[1]	28.03[17]	21.99[56]	0.14[4]	0.55	94.75		0.73
vn1250	Liq	8	1.79[4]	13.57[8]	48.35[22]	15.82[6]	11.97[8]	0.87[2]	7.60[20]	0.07[2]	0.03[4]	0.76	94.92	0.22	0.34
	Ol	21	0.01[0]	51.78[12]	41.41[8]	0.08[0]	0.23[2]	0.00[0]	6.45[6]	0.06[0]	0.05[0]	0.93	100.22		
	Opx	3	0.06[6]	31.74[13]	52.62[16]	8.07[35]	1.79[13]	0.15[0]	5.12[15]	0.38[5]	0.07[8]	0.92	100.68		
	Spinel	11	0.00[0]	21.62[25]	0.44[13]	46.73[83]	0.08[2]	0.19[1]	16.58[26]	14.31[64]	0.07[37]	0.70	98.51		0.60
vn1260	Liq	6	2.01[8]	13.10[8]	47.41[14]	16.82[6]	11.60[8]	1.04[2]	7.96[10]	0.02[2]	0.07[4]	0.75	94.30	0.23	0.29
	Ol	63	0.01[0]	50.93[10]	41.68[4]	0.10[2]	0.22[0]	0.00[0]	7.04[6]	0.04[0]	0.06[2]	0.93	99.95		
	Opx	4	0.21[3]	29.83[56]	52.91[56]	8.21[20]	2.32[31]	0.16[3]	5.86[23]	0.50[12]	0.02[2]	0.90	100.06		
	Spinel	9	0.01[1]	21.73[22]	0.31[8]	49.44[137]	0.09[1]	0.18[1]	16.91[30]	11.29[117]	0.06[3]	0.70	100.55		0.60
vn1270	Liq	15	1.87[2]	13.78[4]	48.21[6]	15.70[6]	11.88[4]	0.79[2]	7.61[6]	0.08[2]	0.13[2]	0.76	95.29	0.24	0.28
	Ol	91	0.01[0]	51.39[8]	41.38[4]	0.08[2]	0.22[0]	0.00[0]	6.87[4]	0.07[0]	0.05[10]	0.93	101.28		
	Opx	5	0.09[1]	32.13[17]	53.35[28]	6.69[40]	1.86[6]	0.07[2]	5.16[12]	0.64[6]	0.04[3]	0.92	101.44		
	Spinel	9	0.02[13]	21.20[23]	0.52[44]	45.24[178]	0.17[5]	0.16[2]	15.95[28]	16.74[3]	0.07[162]	0.70	98.08		0.56
vn1275	Liq	7	2.30[6]	14.23[10]	47.71[10]	14.85[6]	10.88[6]	0.66[2]	9.34[6]	0.07[2]	0.02[2]	0.73	93.88	0.19	0.44
	Ol	111	0.02[0]	51.79[8]	40.86[4]	0.44[2]	0.20[0]	0.01[0]	6.45[4]	0.06[0]	0.26[0]	0.93	100.45		
	Opx	7	0.05[2]	33.19[4]	53.77[8]	5.22[2]	1.50[3]	0.03[0]	5.35[14]	0.80[15]	0.12[0]	0.92	98.45		
	Spinel	8	0.02[1]	19.21[11]	0.27[4]	34.13[59]	0.11[3]	0.25[3]	31.45[27]	14.51[50]	0.12[49]	0.52	94.89		0.74
vn1290	Liq	8	1.86[4]	14.16[10]	48.70[12]	15.51[8]	11.61[4]	0.83[4]	7.07[4]	0.07[4]	0.15[4]	0.78	96.11	0.24	0.29
	Ol	34	0.02[0]	52.07[14]	41.30[8]	0.12[4]	0.23[2]	0.00[0]	6.24[6]	0.04[2]	0.05[2]	0.94	101.41		
	Opx	4	0.09[2]	31.54[3]	52.70[37]	8.25[15]	2.02[8]	0.16[2]	4.98[8]	0.27[12]	0.02[2]	0.92	100.81		
	Spinel	7	0.02[2]	21.33[32]	0.25[5]	44.36[238]	0.09[2]	0.17[1]	14.49[35]	19.25[272]	0.08[3]	0.72	98.99		0.56

Table 3.6 (continued)

Experiment	Phase	No.	Na_2O	MgO	SiO_2	Al_2O_3	CaO	TiO_2	FeO*	Cr_2O_3	MnO	Mg#	Total	K_D	Fe_2O_3/FeO^*
vn1300	Liq	7	1.85[4]	14.41[12]	47.21[12]	14.84[8]	11.76[6]	0.76[4]	9.01[10]	0.07[2]	0.03[2]	0.74	93.36	0.20	0.42
	Ol	30	0.01[0]	52.29[16]	40.97[10]	0.10[4]	0.22[2]	0.00[0]	6.39[4]	0.04[2]	0.07[2]	0.94	100.15		
	Opx	5	0.12[3]	31.78[5]	51.97[8]	7.90[23]	1.96[0]	0.15[2]	5.78[6]	0.32[6]	0.09[0]	0.91	99.77		
	Spinel	10	0.02[1]	20.62[26]	0.27[3]	39.60[100]	0.16[1]	0.21[1]	23.70[25]	15.42[90]	0.09[2]	0.61	97.06		0.72
vn1319	Liq	14	1.53[4]	16.09[8]	47.97[22]	14.16[8]	10.78[10]	0.68[2]	8.51[10]	0.06[4]	0.18[2]	0.77	93.95	0.21	0.38
	Ol	52	0.01[0]	52.35[16]	41.34[14]	0.15[10]	0.25[2]	0.00[0]	5.79[8]	0.11[6]	0.06[2]	0.94	99.48		
	Opx	2	0.07[3]	33.08[7]	53.02[114]	6.14[49]	1.71[5]	0.11[12]	5.08[17]	0.74[24]	0.08[5]	0.92	99.96		
	Spinel	3	0.01[1]	20.12[49]	0.36[27]	32.53[40]	0.14[5]	0.20[1]	22.13[7]	24.52[72]	0.05[6]	0.62	95.31		0.70

[a] All Fe as Fe^{2+}.

[b] Liq, liquid; Ol, olivine; Opx, orthopyroxene; Cpx, clinopyroxene; Amph, amphibole. Orthopyroxene and clinopyroxene analyses are rim compositions.

[c] Number of analyses of each phase.

[d] Mg# = molar MgO/(MgO+FeO*), assuming all Fe as Fe^{2+}.

[e] Origonal probe analysis total. All probe analyses have been normalised to 100wt%.

[f] $K_D = K_D^{Mg\text{-}Fe}$ olivine-melt = $(FeO^*/MgO)_{ol}/(FeO^*/MgO)_{melt}$, assuming all Fe as Fe^{2+}.

[g] Melt Fe^{3+} estimated such that $K_D^{Mg\text{-}Fe}$ olivine-melt gives agreement with model value (0.337 ± 0.004) at 1.5GPa. (Ulmer, 1989). Spinel Fe^{3+} estmated by stoichiometry (3 cations).

[h] Values in square brackets represent 2 standard errors of the analysed compositional range in terms of least units cited, e.g. 0.01[2] should be read as 0.01 ± 0.02.

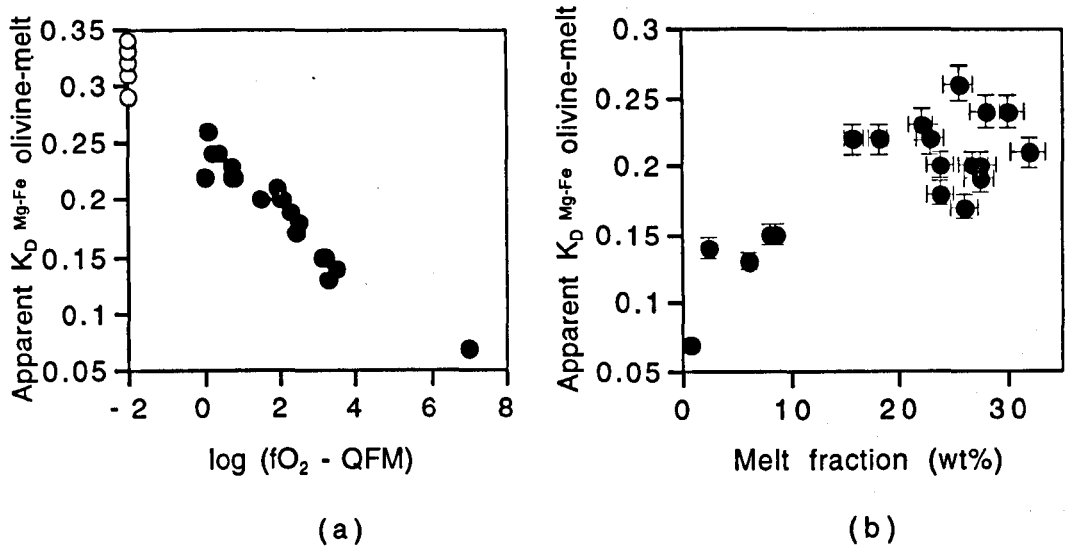

Figure 3.3 (a) Variation in apparent $K_D^{Mg\text{-}Fe}$ olivine-melt with fO_2 during melt generation, at 1.5GPa relative to the quartz-fayalite-magnetite (QFM) buffer. Black-filled circles = hydrous melts (this study), grey-filled circles = hydrous melts (Gaetani & Grove, 1998), open circles = anhydrous melts (Robinson *et al*, 1998). fO_2 estimates (this study) based on ol-opx-sp thermobarometry. Apparent $K_D^{Mg\text{-}Fe}$ olivine-melt = $(FeO^*/MgO)_{olivine}/(FeO^*/MgO)_{melt}$. (b) Variation in apparent $K_D^{Mg\text{-}Fe}$ olivine-melt with melt fraction at 1.5GPa.

Fe^{3+} (*e.g.* Dickenson & Hess, 1986). In the lowest temperature experiment in this study (1085°C), apparent $K_D^{Mg\text{-}Fe}$ ol-m is slightly lower than expected (0.07). This is probably due to Fe oxidation accompanying H_2 loss from the charge. Mass balance of Fe_2O_3 in this experiment suggests that Fe_2O_3 in the bulk composition of the charge increased by 2.75wt% during the run (equivalent to a relative H_2O loss of 11.35 ± 0.3%). Since the Fe^{3+} gained is accommodated at least partially in the melt, apparent $K_D^{Mg\text{-}Fe}$ ol-m is decreased.

3.4.2 Orthopyroxene

Adding H_2O to peridotite has a small effect on opx composition. At F<5wt% amphibole is present in the hydrous peridotite melting residue, and the co-existing opx is enriched in MgO relative to opx in anhydrous peridotite (see Figure 3.4). At F=10-20wt% CaO is lower in opx in hydrous peridotite, due to the sensitivity of co-existing opx and cpx compositions to temperature (see section 3.4.3). At F>22wt%, opx compositions are similar in hydrous and anhydrous peridotites.

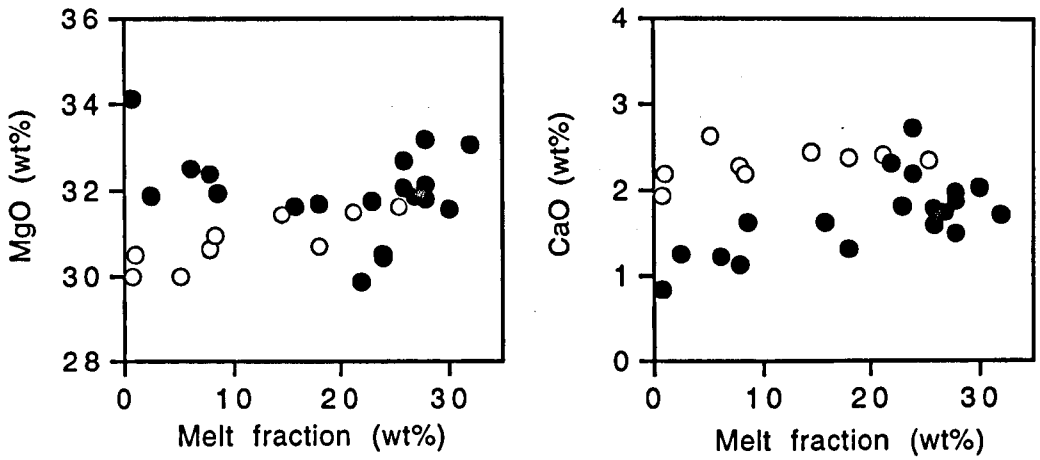

Figure 3.4 Variation in MgO and CaO with melt fraction in orthopyroxene at 1.5GPa. Filled circles = hydrous peridotite Leo3 (this study), open circles = anhydrous peridotite MPY (Robinson *et al*, 1998).

3.4.3 Clinopyroxene

Figure 3.5 shows cpx compositions recalculated as molecular olivine, diopside, Jd+CaTs and quartz and plotted using a Jd+CaTs projection (Falloon & Green, 1988). Compositions of cpx in hydrous partially molten peridotite at 1.5GPa (this study) and 1.6GPa (Gaetani & Grove, 1998) and in anhydrous partially molten peridotite at 1.5GPa (Robinson *et al.*, 1998) are plotted. Cpx compositions demonstrate that the Di component in cpx increases with decreasing temperature (Takahashi, 1986). Adding H_2O to peridotite lowers the temperature of melting, and therefore, for the same degree of melting, cpx in hydrous peridotite is Di-rich relative to cpx in an anhydrous peridotite.

Figure 3.6 shows variation in cpx composition with melt fraction for Al_2O_3 and Na_2O. Cpx in anhydrous peridotite is progressively enriched in Al_2O_3 and Na_2O with decreasing melt fraction. Cpx in hydrous peridotite shows similar trends at F>5wt% but, at smaller melt fractions, becomes relatively depleted in Al_2O_3 and Na_2O. This is due to the presence of pargasitic amphibole in the hydrous peridotite. Amphibole is richer in Na_2O and Al_2O_3 than cpx, so these oxides are progressively depleted in cpx as the proportion of amphibole in the melting residue increases near the solidus.

In summary, adding H_2O to peridotite has a significant effect on cpx composition. Firstly, cpx is enriched in Di component at all melt fractions due to the lower temperature of melting in hydrous peridotite. Secondly, cpx is depleted in Al_2O_3 and Na_2O (Jd+CaTs component) near the solidus relative to cpx in anhydrous peridotite, due to the presence of amphibole.

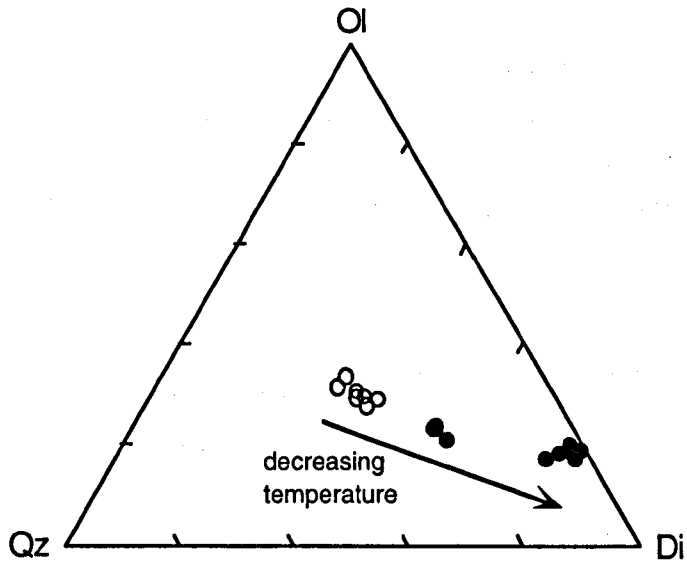

Figure 3.5 Projected clinopyroxene (cpx) compositions in peridotite melting residue at 1.5-1.6GPa, in the CIPW molecular normative tetrahedron. Projection from jadeite + calcium tschermakite (Jd+CaTs) onto the base olivine (Ol)-Diopside (Di)-Quartz (Qz). Black-filled circles = cpx in hydrous peridotite Leo3 at 1.5GPa (this study), grey-filled circles = cpx in hydrous peridotite at 1.6GPa (Gaetani & Grove, 1998), open circles = cpx in anhydrous peridotite MPY at 1.5GPa (Robinson *et al.*, 1998). Fe^{3+}/FeO^* assumed to be 0.1.

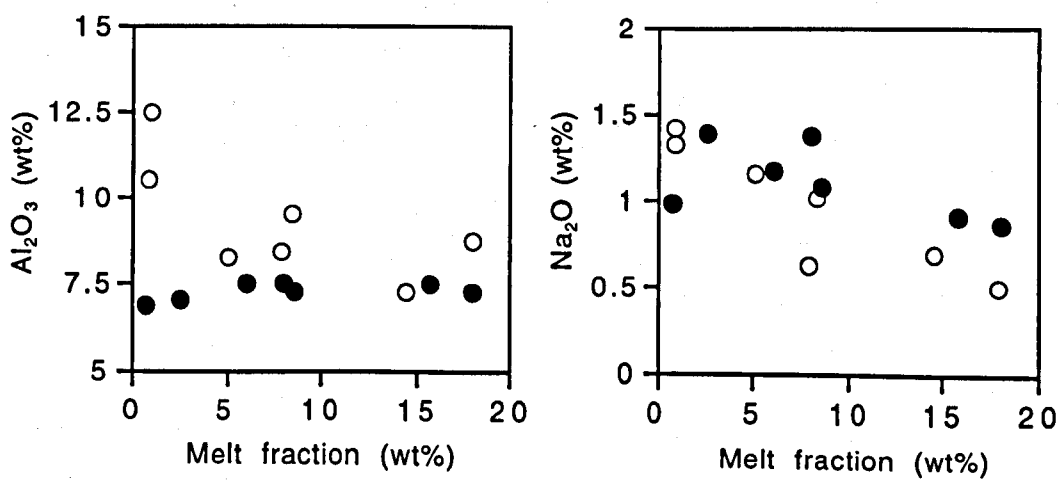

Figure 3.6 Variation in Al_2O_3 and Na_2O with melt fraction in clinopyroxene with melt fraction at 1.5GPa. Filled circles = hydrous peridotite Leo3 (this study), open circles = anhydrous peridotite MPY (Robinson *et al*, 1998).

3.4.4 Spinel

Since the experiments in this study were conducted under relatively oxidising conditions, the spinels present contain a significant proportion of Fe^{3+}. Spinel electronprobe analyses were recorded and corrected using ZAF procedures, and Fe^{3+} in the spinels was estimated from stoichiometry (3 cations). Cation ratios were calculated as follows:

X site: $Mg^* = Mg/(Mg + Fe^{2+})$
Y site: $Cr^* = Cr/(Cr + Al + Fe^{3+})$
$Al^* = Al/(Cr + Al + Fe^{3+})$
$Fe^* = Fe^{3+}/(Cr + Al + Fe^{3+})$

Figure 3.7 shows variation in Mg* with temperature for spinel in hydrous peridotite (this study) and in anhydrous peridotite MPY (Robinson *et al.*, 1998). Spinels in hydrous peridotite range in Mg* from 0.74-0.85, and form a general trend of increasing Mg* with increasing temperature. Mg* in spinels in anhydrous peridotite falls along the same trend at higher temperature. An exception to this trend is the spinel in the lowest temperature experiment in this study, which has high Mg*. Fe^{2+} may have been decreased in the spinel by oxidation due to H_2 loss from the charge, as discussed with reference to olivine-melt Mg-Fe partitioning in the same experiment (see section 3.4.1).

Figure 3.8 shows variation in Cr* in spinel with degree of melting. Cr* increases with increasing melt fraction, but the rate of increase is more rapid above cpx-out. Spinel Cr* is lower in hydrous peridotite than in anhydrous. Figure 3.9 shows variation in Al* and Fe* in spinel with degree of melting. Fe* rapidly decreases with increasing melt fraction until close to cpx-out. At larger melt fractions, the data show more scatter but suggest that Fe* remains constant or increases slightly. Al* forms a complementary trend to that of Fe*, increasing with increasing melt fraction until close to cpx-out, then decreasing with further degree of melting. Al* in anhydrous peridotite decreases steadily with increasing melt fraction (Robinson *et al.*, 1998). The spinels in the anhydrous peridotite MPY were generated under more reducing conditions ($fO_2 \approx$QFM-2) than those in this study, and stoichiometric analysis shows that they contain negligible Fe^{3+}. Al* appears to be strongly correlated with the presence or absence of Fe^{3+} in spinels and hence fO_2.

In summary, adding H_2O to peridotite decreases Mg* of spinel at a given melt fraction, due to the lower temperature of melting. Cr* and Al* are sensitive to Fe* and oxidation conditions in the peridotite melting environment. Hydrous peridotite in subduction zones is believed to be under more oxidising conditions than other tectonic environments. Spinel in hydrous peridotite is likely to have lower Al* and Cr* and higher Fe* than

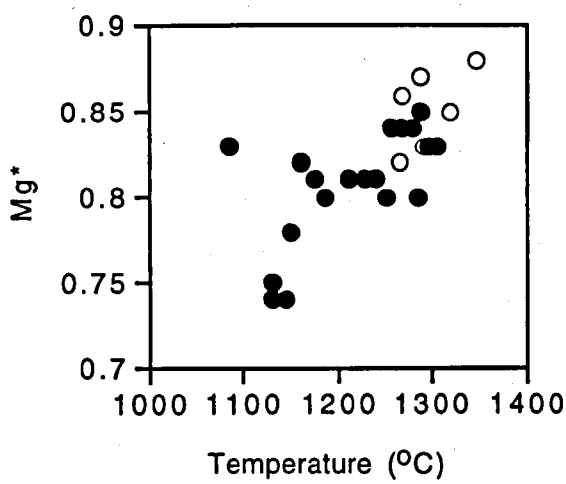

Figure 3.7 Variation in Mg* of spinel with temperature at 1.5GPa. Filled circles = hydrous peridotite Leo3 (this study), open circles = anhydrous peridotite MPY (Robinson *et al*, 1998). Mg* = $Mg/(Mg+Fe^{2+})$

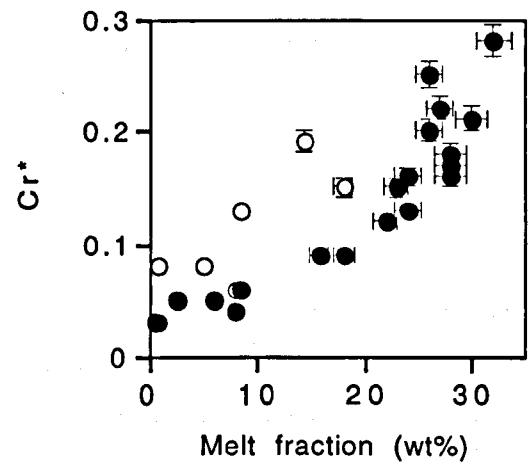

Figure 3.8 Variation in Cr* of spinel with melt fraction at 1.5GPa. Filled circles = hydrous peridotite Leo3 (this study), open circles = anhydrous peridotite MPY (Robinson *et al*, 1998). Cr* = $Cr^{3+}/(Cr^{3+}+Al^{3+}+Fe^{3+})$.

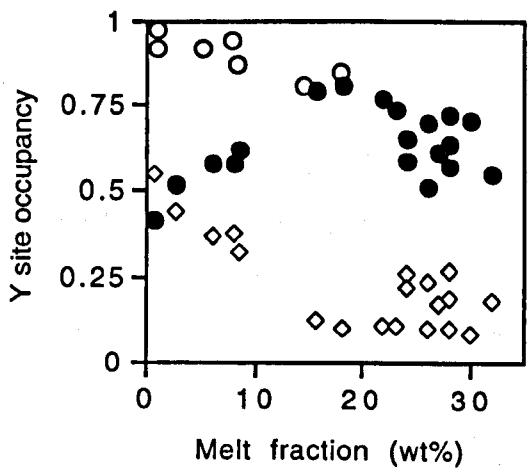

Figure 3.9 Variation in Y-site occupancy of spinel with melt fraction at 1.5GPa. Diamonds = Fe*, hydrous peridotite Leo3 (this study), filled circles = Al*, hydrous peridotite Leo3 (this study), open circles = Al*, anhydrous peridotite MPY (Robinson *et al*, 1998). Al* = $Al^{3+}/(Cr^{3+}+Al^{3+}+Fe^{3+})$, Fe* = $Fe^{3+}/(Cr^{3+}+Al^{3+}+Fe^{3+})$.

anhydrous peridotite in a more reducing environment.

3.4.5 Amphibole

In two low-temperature experiments (1085, 1130-10), amphibole is seen in equilibrium with melt. In both cases, the amphibole is considered to be stable (not a quench product) on the basis of crystal morphology and size, Mg* (Green, 1973) and consistent stoichiometric composition throughout charge. Stoichiometric composition was calculated on a 23-oxygen basis, and Fe_2O_3/FeO^* was assumed to be 0.3-0.4 given the relatively oxidising conditions in experiments 1085 and 1130-10 (Helz, 1982). In both experiments, amphibole composition is pargasitic with Na occupancy in the A-site (Na[A]) equal to nearly 1, and no Na in the M4 site. Al^{IV} in the amphiboles is =1.86-1.87 and Al^{VI} is 0.5-0.57. The amphibole compositions are similar to those generated by partial melting of a MORB pyrolite at 1050°C, 1.5-1.8GPa (Niida & Green; 1999). Na[A] is lower in amphiboles in MORB pyrolite (0.76-0.86), as expected given lower Na_2O (0.4wt%) in MORB pyrolite bulk composition.

3.5 Liquid composition

Liquid compositions are given in Table 3.6. Fe^{3+} in the melt was calculated such that $D^{Mg\text{-}Fe}$ ol-m agrees with the value predicted at 1.5GPa (0.337± 0.004) by Ulmer (1989). All liquid compositions are given on a volatile-free basis, i.e. oxides are totalled to 100wt%.

3.5.1 Variation in oxide content of the melt with F

Figure 3.10 shows the variation in melt composition with degree of melting, with all oxides shown on a volatile-free basis (i.e. oxide total = 100wt%). Variation in melt composition with degree of melting for anhydrous peridotite MPY (Robinson *et al.*, 1998) is shown for comparison. Contouring of the hydrous melt data according to peridotite H_2O content has not been attempted, though a continuum in melt composition between "anhydrous" and "hydrous" would be expected.

MgO content increases steadily in the liquid as extent of melting increases. In anhydrous partial melts, MgO increases more rapidly with increasing melt fraction until cpx-out (F=20wt%), then increases more slowly with further melting. As a result, MgO is similar in hydrous and anhydrous melts at F<5wt% and F>25wt%, but MgO is lower in hydrous melts at intermediate melt fractions.

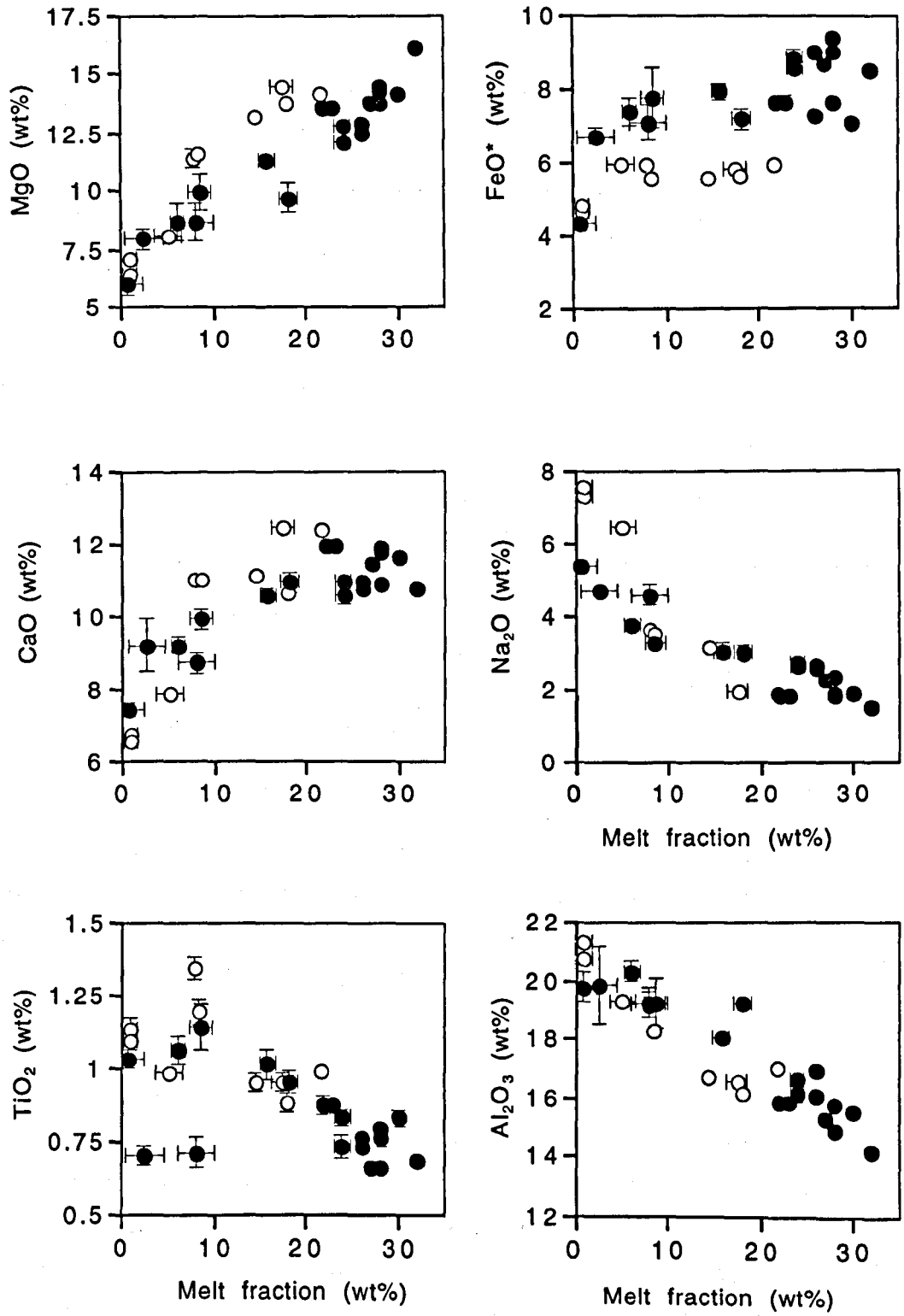

Figure 3.10 Variation in oxide content of liquid with melt fraction at 1.5GPa. Filled circles = hydrous peridotite Leo3 (this study), open circles = anhydrous peridotite MPY (Robinson *et al*, 1998). Melt H_2O contents are given in Table 3.3. Error bars represent 2 standard errors.

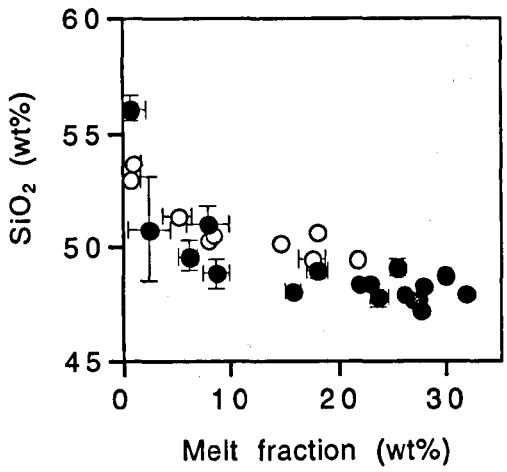

Figure 3.10 contd. Symbols as on previous page.

FeO* increases rapidly in hydrous liquids with increase in extent of melting just above the solidus, then very slowly at F>5wt%. A similar trend is seen in anhydrous liquids, but FeO* content of the hydrous liquids are ≈2wt% higher at all melt fractions. This may have 2 causes. The first is the difference in bulk composition between Leo3 and MPY, since Leo3 is more fertile and has higher FeO*. The second is difference in oxidation state with more oxidising conditions of this study ($fO_2 \geq QFM+2$) producing more FeO*-rich melts, which contain a significant proportion of Fe^{3+}.

CaO increases in the liquid with increase in extent of melting until cpx-out (F=22wt%), then decreases in the liquid with further melting due to dilution. CaO follows a similar trend in anhydrous liquids. CaO is slightly more abundant in hydrous melts than in anhydrous melts at F<5wt%, but is lower in hydrous melts at F=5-22wt%. CaO in hydrous melts at melt fractions close to or above cpx-out (F>22wt%) is similar to that in anhydrous melts.

Na_2O content of the liquid decreases with increasing degree in melting. At F>8wt%, Na_2O contents in partial melts of hydrous peridotite are similar to those of anhydrous peridotite. At smaller melt fractions, Na_2O in a hydrous liquid is lower than in ananhydrous liquid of equivalent melt fraction. The near-solidus high Na_2O liquids (Na_2O>6wt%) generated by partial melting of anhydrous peridotite (Hirschmann *et al.*, 1998; Robinson *et al.*, 1998) are not observed near the solidus of hydrous peridotite because of co-exisitng amphibole.

TiO_2 increases slightly in the liquid with increasing degree in melting until F=8wt%. TiO_2 then decreases in the liquid as melting continues, due to dilution. A similar trend in observed in anhydrous liquids. TiO_2 in two experiments (1130, 1130-10) is lower than expected, and may be due to small amounts (<1wt%) of ilmenite in the charge.

Al_2O_3 content stays relatively constant at ≈20wt% in the liquid as extent of melting increases from the solidus of hydrous peridotite to F=5wt%. Once amphibole is eliminated, Al_2O_3 decreases slowly due to dilution. Once cpx has been eliminated from the peridotite residue (F>22wt%), Al_2O_3 decreases more rapidly. Al_2O_3 in anhydrous melts decreases at a steady rate as melt fraction increases. At F<5wt% Al_2O_3 is lower in a hydrous melt than in an anhydrous one at the same F. At F=5wt%, trends in Al_2O_3 vs F for anhydrous and hydrous peridotite partial melts cross, so that for F=5-22wt% hydrous liquids have higher Al_2O_3 than anhydrous liquids. At F>22wt%, hydrous and anhydrous liquids have similar Al_2O_3 contents.

SiO_2 decreases rapidly as F increases from 0-5wt%, but decreases very slowly thereafter. SiO_2 is similar in hydrous and anhydrous melts at F>1wt%. SiO_2 is slightly higher in hydrous melts than anhydrous ones at F<1wt%, which may be due to the presence of amphibole in hydrous peridotite at small melt fractions. Amphibole-bearing peridotite has a lower bulk distribution coefficient for SiO_2 (D^{SiO2}) relative to anhydrous peridotite (see Table 3.7), and therefore higher SiO_2 in the co-existing melt.

3.5.2 Normative liquid compositions

Figure 3.11a shows melt compositions recalculated as molecular olivine, diopside, quartz and jadeite + calcium tschermakite, and plotted using a diopside projection (Falloon & Green, 1988). Enstatite (En) composition is shown on the Ol-Qz join. Points along the melting trends where a phase is eliminated from the peridotite residue are marked. The lowest-temperature liquid plots near the Qz-Jd+CaTs join, towards the Qz apex, and is quartz normative on a volatile-free basis. As melting continues, the liquid composition moves away from the Qz apex, becoming less SiO_2 rich. At melt fractions close to the point of amphibole elimination (amphibole-out), the liquid is SiO_2 undersaturated and nepheline (Ne) normative (experiment 1130-10). Once amphibole is eliminated, melts are olivine-hypersthene (ol-hy) normative at all melt fractions. With increasing melting, the liquid composition moves towards the Ol apex until cpx is eliminated from the peridotite residue. The liquid composition then moves towards the Ol-En join with increasing melt fraction.

Figure 3.11b shows liquid compositions for partial melting of Leo3 in comparison to liquids generated by partial melting of anhydrous peridotite MPY (Robinson *et al.*, 1998). Liquid compositions formed at small melt fractions from anhydrous peridotite plot towards the Jd-CaTs apex and are Ne normative. As melting increases, the anhydrous liquid composition moves away from the Jd+CaTs apex towards the Ol-Opx join. At

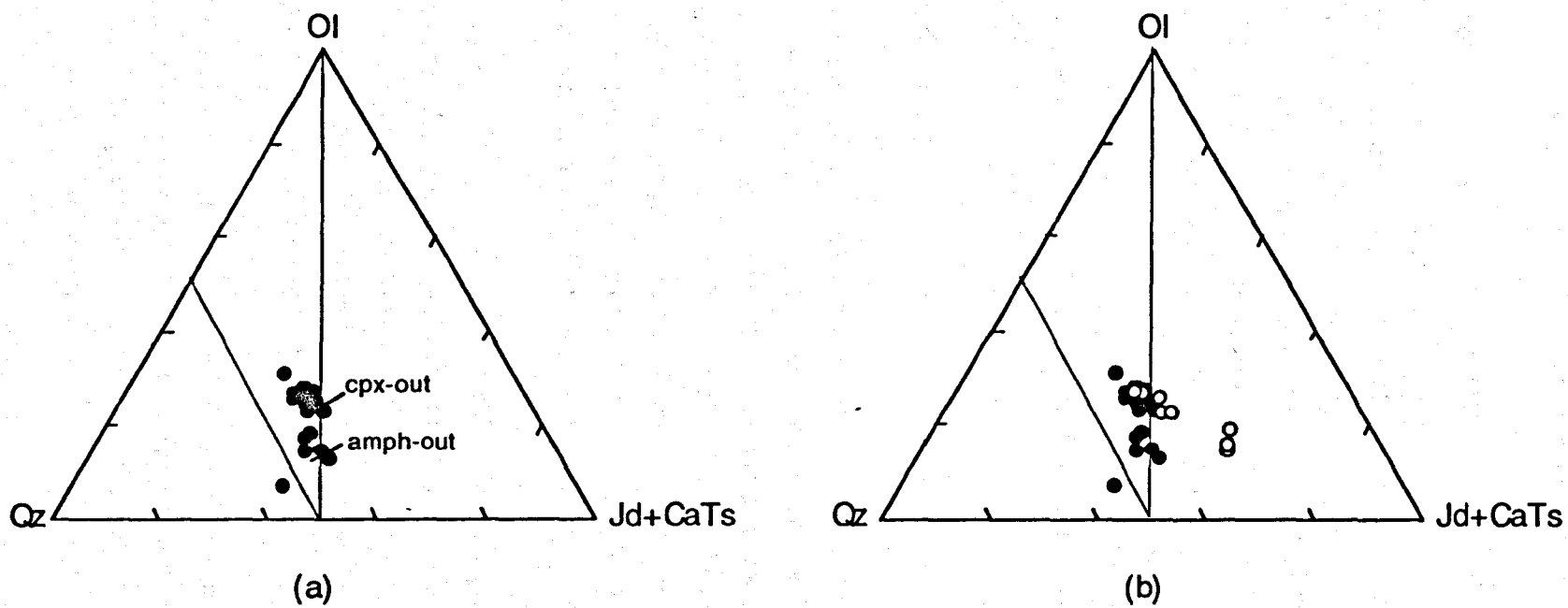

Figure 3.11 Projected liquid compositions at 1.5GPa, in the CIPW molecular normative tetrahedron. Projection from diopside (Di) onto the base olivine (Ol)-jadeite + calcium tschermakite (Jd+CaTs)-Quartz (Qz). Values for Fe^{3+}/FeO^* in hydrous liquids given in Table 3.5. (a) Liquid compositions for partial melting of Leo3. Grey lines indicate the point along the melting trend at which a solid phase is eliminated from the peridotite melting residue. Amph-out = point of amphibole elimination, cpx-out = point of clinopyroxene elimination. (b) Comparison of liquid compositions for partial melting of hydrous and anhydrous peridotite. Filled circles = hydrous partial melts of Leo3 (this study), open circles = anhydrous partial melts of MPY (Robinson et al, 1998). Fe^{3+}/FeO^* in anhydrous liquids assumed to be 0.1.

F>20wt%, (i.e. close to or above cpx-out), the hydrous and anhydrous liquid composition trends converge.

3.5.3 Primary andesitic melts from peridotite?

On a volatile-free basis, the first liquid derived by partial melting of Leo3+0.25wt% H_2O has SiO_2 = 56wt% and is quartz normative. This suggests that primary andesitic melts may be generated by partial melting of hydrous peridotite at 1.5 GPa. This is only likely to be possible if the melt fraction is very small (<1wt%) and a significant proportion of amphibole is present in the peridotite melting residue. These conditions are most likely to be satisfied if the peridotite is H_2O-saturated (see Fig. 3.2). If the peridotite is undersaturated, amphibole melts very rapidly and only a very narrow temperature interval (≈5°C) exists over which a melt fraction of <1wt% would be produced. Note that the normative calculation is sensitive to the accuracy of the melt composition analysis; *e.g.* if SiO_2 decreased from 56wt% to 53wt%, or Na_2O increased from 5.38wt% to 6wt%, the melt becomes ol-hy normative.

3.5.4 Summary

The differences between the hydrous and anhydrous melt composition trends with increasing melt fraction can be interpreted in terms of the solid phases present in the peridotite melting residue, and their contribution to the melting process.
(i) At F<5wt%, hydrous melts are depleted in Na_2O and Al_2O_3, and enriched in CaO and SiO_2 relative to anhydrous melts. This is due to the presence of amphibole in hydrous peridotite. Hydrous melts in equilibrium with amphibole at small melt fractions therefore plot further from the Jd+CaTs apex and closer to the Qz apex than anhydrous melts.

(ii) At F=5-20wt%, hydrous melts are depleted in MgO and CaO and enriched in Al_2O_3 relative to anhydrous melts at the same melt fraction. In normative space, hydrous melts are depleted in Ol relative to anhydrous melts. Differences between hydrous & anhydrous melts are due to differences in the melt reaction, as discussed below and diminish progressively as cpx is consumed.

(iii) At F>20wt%, when cpx is nearly or totally consumed, the major phases being melted in peridotite are opx and ol. These have similar compositions in hydrous and anhydrous peridotite at large melt fractions, therefore the melt composition trends for hydrous and anhydrous peridotite converge.

3.6 Melting reactions

Figure 3.12 illustrates the evolution in liquid composition with increasing degree of melting. Change in melt composition with increasing melt fraction is shown as a generalised trend, and the points along the trend where amphibole and cpx are eliminated from the peridotite residue are marked. Trends in opx, cpx and amphibole compositions (recalculated on the same basis) with increase in melt fraction are also shown. The evolution in liquid composition can be broken down into 3 parts, relating to 3 successive melting reactions.

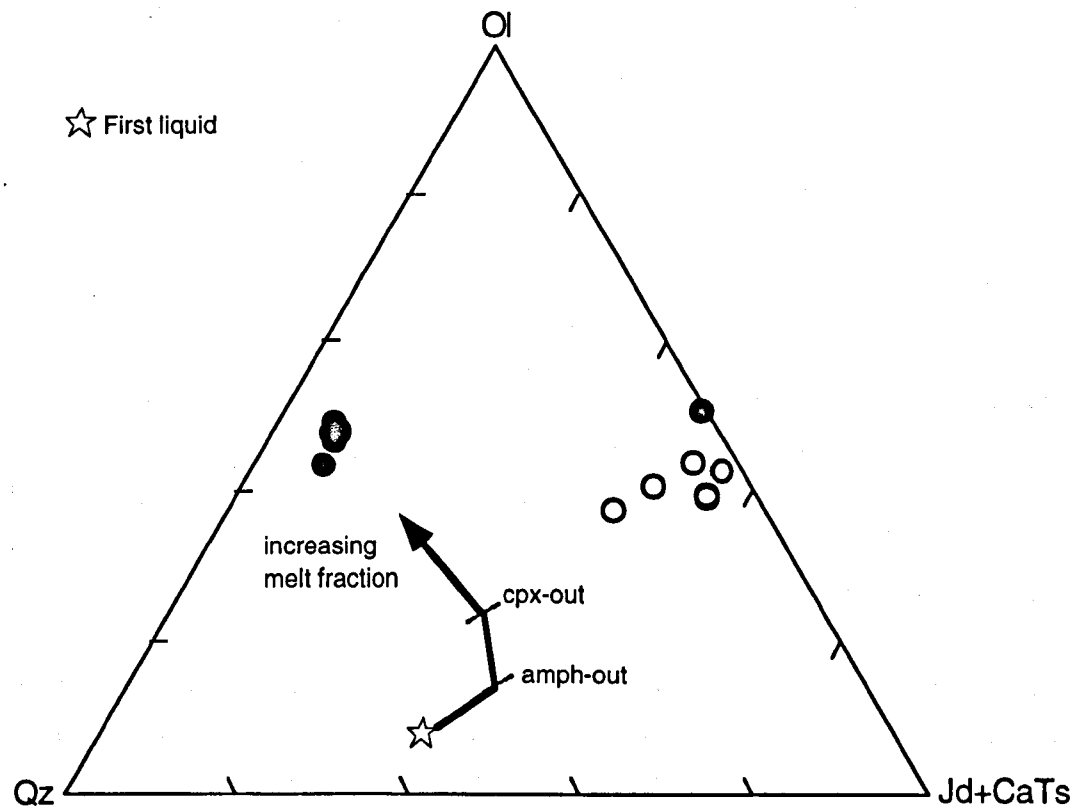

Figure 3.12 Projected trend in liquid composition with increasing degree of melting of hydrous peridotite at 1.5GPa, in the CIPW molecular normative tetrahedron. Projection from diopside (Di) onto the base olivine (Ol)-jadeite+calcium tschermakite (Jd+CaTs)-Quartz (Qz). Values for Fe^{3+}/FeO^* in hydrous liquids are given in Table 3.5. Compositions of solid phases co-existing with the liquid are also plotted. Black circles = orthopyroxene, grey circles = amphibole, open circles = clinopyroxene. Grey lines indicate the point along the melting trend at which a solid phase is eliminated from the peridotite melting residue. Amph-out = point of amphibole elimination, cpx-out = point of clinopyroxene elimination.

(i) Melting reaction in amphibole-bearing lherzolite (F<5wt%)

The first liquid produced by partial melting of amphibole-bearing lherzolite is Na_2O-poor and SiO_2-rich relative to the first liquid produced from anhydrous peridotite, and may be quartz-normative. As amphibole melts, the normative liquid composition evolves towards amphibole. Amphibole melts by the following reaction (Sen & Dunn, 1994; Sisson *et al.*, 1997):

amphibole + opx = olivine + cpx + spinel + liquid

The compositions of amphibole, cpx, opx and spinel all evolve during the amphibole melting interval, and the stoichiometry of the melting reaction is not expected to be

constant. The stoichiometry of the reaction is also likely to be sensitive to the bulk composition and H_2O content of the peridotite (Niida & Green, 1999). No realistic attempt to model such a complex reaction can be made with the available data.

(ii) Melting reaction in lherzolite (F=5-22%)

Once amphibole is eliminated from the residue, the liquid composition moves towards a tie-line between the co-existing opx and cpx compositions, and opx and cpx melt to produce liquid and olivine. Differences in the melt reaction between hydrous and anhydrous peridotite are illustrated by the variation in modal phase proportions with increasing melt fraction (see Figure 3.13). During hydrous peridotite melting, cpx is consumed less rapidly and opx more rapidly than under anhydrous conditions. More olivine is produced in the hydrous peridotite melt reaction than in the anhydrous one, for the same increase in melt proportion. Adding H_2O to peridotite firstly lowers the melting temperature, which increases the Di component in cpx and stabilises cpx relative to opx.Secondly, it favours depolymerization and stabilises a greater proportion of olivine than in anhydrous peridotite (Kushiro *et al.*, 1968). In effect, addition of H_2O to peridotite stabilises cpx and olivine at the expense of opx for moderate degrees of melting. This causes the observed differences in melt compositions between hydrous and anhydrous liquids at F=10-20wt%. Hydrous liquids have lower MgO and higher Al_2O_3, reflecting equilibrium with a larger proportion of olivine, and lower CaO, reflecting equilibrium with a larger proportion of more Ca-rich cpx.

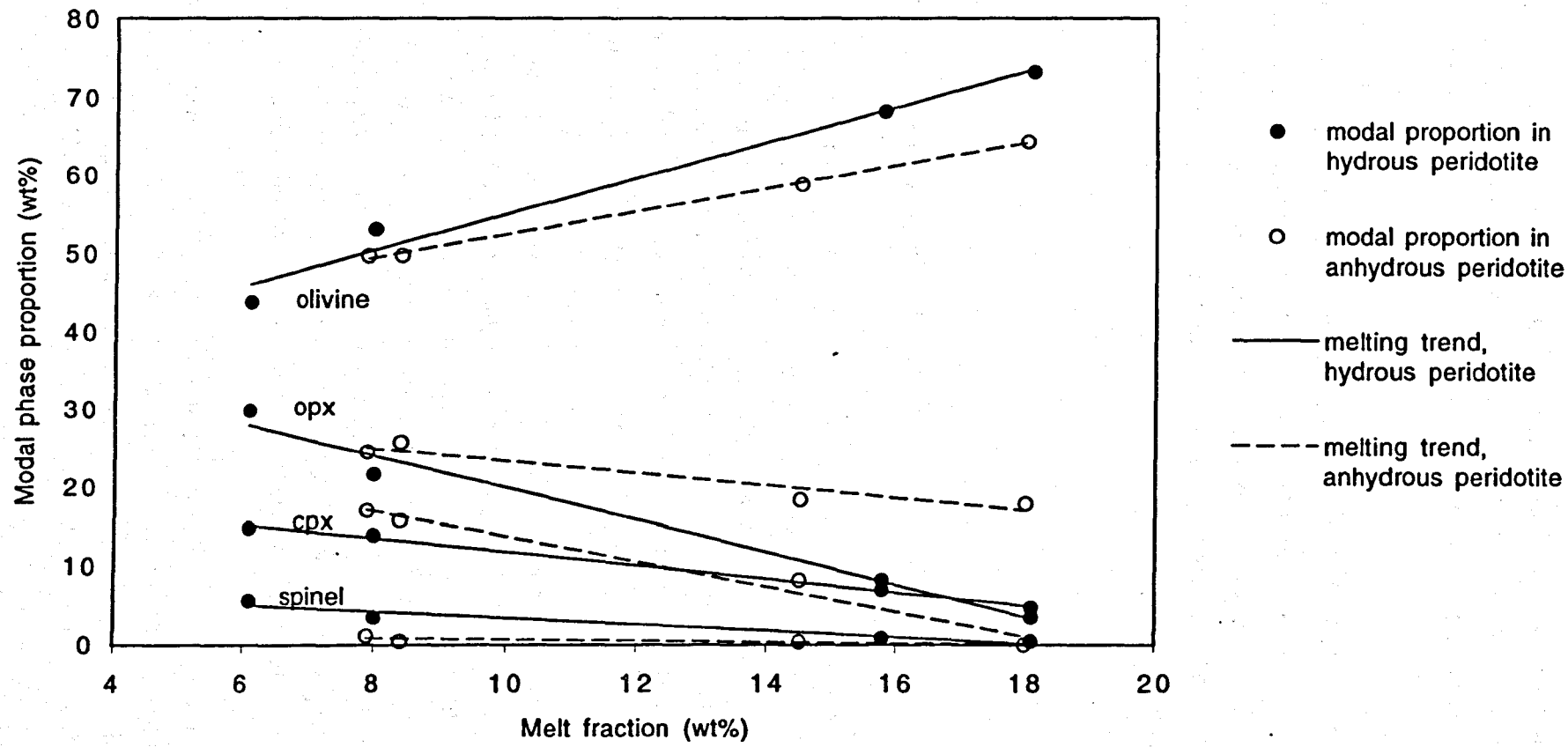

Figure 3.13 Variation in modal phase proportions with melt fraction for hydrous and anhydrous peridotite at 1.5GPa. Hydrous peridotite = Leo3 (this study), anhydrous peridotite = MPY90 (Robinson *et al* ., 1998)

(iii) Melting in harzburgite (F>22wt%)

Once cpx has been eliminated from the residue, the liquid moves towards a tie-line between olivine and opx composition. The melting reaction (using the two-liquid mass balance method and fictive solid phase compositions) is estimated to be:

0.12 ol + 0.41 opx + 0.04 sp = liquid

Olivine has changed from a product to a reactant in the reaction. Opx is the greatest contributor to the melting reaction, therefore the liquid composition evolves towards a composition on the ol-opx tie-line that is close to the opx cluster (see Figure 3.12). The anhydrous melting reaction is expected to be similar, since opx and ol compositions in anhydrous peridotite residue are similar to those in hydrous peridotite at large degrees of melting.

3.7 Conclusions

At 1.5GPa, adding H_2O to peridotite has the following effects.

1. The temperature required to generate a given melt fraction is decreased. At F>8wt%, the decrease in temperature is directly proportional to the amount of H_2O added. For a given H_2O content, the difference in temperature relative to anhydrous peridotite is diminished with increasing melt fraction. At F<8wt%, onset and rate of melting is controlled by amphibole stability. Melting starts at ≈1100°C in H_2O-undersaturated peridotite in association with the beginning of amphibole breakdown.

2. Amphibole forms in the peridotite melting residue below the solidus. Amphibole co-exists with liquid over a narrow temperature interval, and these liquids are Na_2O- and Al_2O_3-poor and SiO_2-rich relative to anhydrous liquids at the same melt fraction (<5wt%). The first melt may be quartz normative (on a volatile-free basis) but rapidly evolves to Ne-normative composition as amphibole melts. All hydrous melts are ol-hy normative once amphibole has been consumed. Cpx co-existing with amphibole is depleted in the Jd+CaTs component, relative to cpx in anhydrous peridotite at F<5wt%.

3. At any given melt fraction, cpx in hydrous peridotite is Di-rich and En-poor relative to cpx in anhydrous peridotite. This is due to the lower temperature of melting in hydrous peridotite. At F=5-22wt%, the change in cpx composition alters the stoichiometry of the melting reaction. Cpx and ol are stabilised at the expense of opx, relative to the melting reaction in anhydrous peridotite. As a result of the change in melting reaction, hydrous

melts at moderate melt fractions are depleted in MgO and CaO, and enriched in Al_2O_3 relative to anhydrous melts. The differences in composition between hydrous and anhydrous melts diminish as cpx is progressively eliminated from the peridotite melting residue.

4. At large melt fractions, hydrous and anhydrous melts are similar in composition. This is because cpx has been eliminated from the peridotite melting residue, and the difference in temperature relative to anhydrous peridotite is greatly decreased.

Hydrous peridotite in subduction zones is believed to be under more oxidising conditions than other tectonic environments (Wood *et al.*, 1990; Ballhaus, 1992). The effect of increased fO_2 on partial melting of peridotite is to increase Fe^{3+} and FeO* in the melt, so that $D^{Mg\text{-}Fe}$ ol-m is lower than the value predicted by Ulmer at 1.5GPa. Under more oxidising conditions, the spinel formed in peridotite is Fe^{3+}-bearing and therefore depleted in Al^{3+} relative to spinel in less oxidised peridotite.

CHAPTER 4

The Effect of H_2O on Peridotite Melting at 3GPa

Introduction

In a subduction zone, melting in the mantle wedge beneath the volcanic front is estimated to start at a depth of 100-120km (*e.g.* Gill, 1981). At this depth, equivalent to a pressure of 3-3.5GPa, garnet is the stable aluminous phase in peridotite. Trace-element and isotopic ratios in mid-ocean ridge basalts (MORB) indicate that melting initiates within the garnet facies (*e.g.* Salters & Hart, 1989; Johnson *et al.*, 1990), but at the temperatures required to initiate melting under dry conditions, prohibitively high melt fractions would be generated. It has been recently suggested (Hirth & Kohlstedt, 1998) that the presence of H_2O in the MORB source region could initiate melting at much lower temperature and provide a mechanism for producing the MORB garnet signature without extreme degrees of melting. Data on hydrous peridotite melting in the garnet lherzolite facies are therefore essential in understanding melting processes in both subduction zone and mid-ocean ridge systems.

I have conducted experiments at 3GPa to simulate partial melting of garnet-bearing hydrous peridotite at melt fractions ranging from 6wt% to >25wt%. I have used an AuPd-Pt double capsule design that has been demonstrated to minimise Fe and H_2O loss under relatively oxidising conditions (≥QFM+1) (see Chapter 2). Experiments were conducted using the sandwich technique, since this can be used successfully to study partial melting over a range of melt fractions (Robinson *et al.*, 1998), without engendering problems of polybaric melt accumulation (Falloon *et al.*, 1998). The peridotite (LeoP1) used in these experiments has a fertile composition similar to MORB pyrolite (Jaques & Green, 1979; Robinson *et al.*, 1998) and is K_2O-free (see Table 4.1). This provides a fundamental dataset on partial melting of hydrous garnet-bearing peridotite, against which results of more complex sysems (e.g. phlogopite- or amphibole-bearing garnet peridotite) can be compared. To investigate the effect of H_2O on partial melting of garnet lherzolite at 3GPa, I will compare my results to those for anhydrous peridotites: MORB pyrolite (MPY) and Tinaquillo Lherzolite (TL) (Robinson, unpubl.) and PHN-1611 (Kushiro, 1996). The compositions of MPY, TL and PHN-1611 are given in Table 4.1. To investigate the effect of increasing presure on hydrous peridotite melting, I will compare my results to those for peridotite Leo3 at 1.5GPa (composition of Leo3 is given in Table 3.1).

Previous studies (Green & Ringwood, 1967; Presnall *et al.*, 1978; Walter & Presnall, 1994; Kushiro, 1996) have demonstrated that the effects of increased pressure on peridotite phase equilibria are: (i) a reduction in the olivine liquidus volume relative to that of diopside, resulting in more olivine-rich and diopside-poor melt compositions at higher pressure, (ii) a change from spinel to garnet as the major aluminous in peridotite. These effects cause the melting reaction to change from:

$$opx + cpx + spinel = ol + liquid$$

at 1.5GPa, to

$$ol + cpx + garnet = opx + liquid$$

at 3.2GPa (Walter & Presnall, 1994).

4.1 Experimental and analytical methods

4.1.1 Experimental methods

Starting mixes were prepared by grinding analytical grade oxides (SiO_2, TiO_2, Al_2O_3, Fe_2O_3, Cr_2O_3, NiO and MgO) and carbonates (Na_2CO_3 and $CaCO_3$) under ethanol in an agate mortar. The mixtures were decarbonated at 1000°C in air, re-ground and reduced in a CO/CO_2 gas-mixing furnace at 1000°C at fO_2 equivalent to 1 log unit below the quartz-fayalite-magnetite buffer (QFM-1). This was chosen as a reasonable lower limit to oxidation conditions in a subduction zone mantle at a depth equivalent to 3GPa (Wood *et al.*, 1990; Ballhaus, 1992). The mixtures were then reground under ethanol until the grain size was ≤30μm. H_2O was added to starting mixes LeoP1, Leo12 and Leo13 as $Mg(OH)_2$, and to starting mix Leo16 as $Mg(OH)_2$ and $Al(OH)_3$. The mixes were reground and subsequently stored at 120°C prior to use. The compositions of all basaltic starting mixes were verified by fusing mixes at 1GPa, 1300°C, using a $Au_{80}Pd_{20}$ capsule inside a Pt capsule and run durations of 30mins. The resulting crystal-free glasses were analysed by electron microprobe. The analysed starting compositions are shown in Table 4.1.

Experiments were conducted in an end-loaded, solid media piston cylinder apparatus. CaF_2 outer sleeves were used in 1/2 inch diameter assemblies with crushable alumina inner sleeves and a graphite furnace. An $Au_{80}Pd_{20}$-Pt double capsule (see Figure 2.1) was used to minimise Fe and H_2O loss from the charge. The capsule was protected from

Table 4.1 Starting compositions used in experimental studies at 3GPa (all analyses are recalculated to 100wt%).

	LeoP1[a]	Leo12[b]	Leo13[b]	Leo16[b]	MPY[c]	TL[c]	PHN[d]
SiO_2	44.52	45.13	41.97	42.52	45.90	45.40	43.70
TiO_2	0.17	0.78	1.15	1.60	0.17	0.10	0.25
Al_2O_3	4.35	11.48	12.23	10.28	4.65	3.53	2.75
Cr_2O_3	0.45	0.02	0.01	0.11	0.57	0.26	0.28
FeO*	7.51	9.01	11.43	7.97	6.15	7.74	10.19
NiO	0.26	0.02	0.02	0.11	0.00	0.00	0.00
MgO	38.38	15.76	15.45	12.68	38.40	39.70	37.22
CaO	3.36	11.00	10.33	8.50	3.61	3.11	3.26
Na_2O	0.40	2.14	2.35	5.32	0.50	0.25	0.33
K_2O	0.00	0.00	0.00	0.00	0.00	0.00	0.14
H_2O[e]	0.50	5.00	5.00	10.90	0.00	0.00	0.00
Mg#[f]	0.90	0.76	0.71	0.74	0.89	0.90	0.87

* All Fe as Fe^{2+}.
[a] Nominal bulk composition.
[b] Probe analysis
[c] Robinson *et al.*, 1998. MPY = MORB pyrolite, TL = Tinaquillo Lherzolite.
[d] Kushiro, 1996. PHN = PHN-1611.
[e] Nominal H_2O content (wt%).
[f] Mg# = molar MgO/(MgO+FeO*), assuming all Fe as Fe^{2+}.

thermocouple intrusion by a 0.5mm thick Pt disc.

The hot piston-out method was used in all cases (Johannes *et al.*, 1971). Temperature was monitored and controlled to within ±1°C using a WRe_3/WRe_{25} (D-type) thermocouple. No correction for the effect of pressure on thermocouple e.m.f. was made. A pressure correction of -8% for the CaF_2 assembly, based on calibration of the quartz-albite-jadeite transition, was applied. Pressure was monitored and controlled to within ±0.05GPa using a Heise gauge. The temperature gradient close to the centre of the furnace within the assemblies is ≈3°C mm^{-1} based on calibrations using 2 thermocouples (H. Soulard, pers. comm.) At the end of each run, experiments were quenched at initial rates of ≈300°C s^{-1}. Experimental run conditions are given in Table 4.2.

4.1.2 Analytical methods

After quenching, capsules were extracted, mounted in Petropoxy™ resin, sectioned longitudinally and polished to a 0.1μm finish. In all experiments the liquid quenched to a mat of feathery clinopyroxene and/or amphibole crystals with interstitial glass. All phases were analysed at the University of Bristol using a four-spectrometer Jeol JXA-8600 electron microprobe in wavelength dispersive mode with a 15 kV accelerating voltage. Crystal phases were analysed using a 1μm spot and 15nA beam current. Liquids generated at ≥1365°C were analysed using a 10μm spot and 15nA beam current to limit alkali migration. Accuracy of the analysis technique was verified by using the same conditions to analyse a quench mat generated from a basalt of known composition (see Table 4.5, experiments L12 & M2). The quench mat composition agrees with the real composition within 2 standard errors for all

Table 4.2 Experimental run conditions at 3GPa.

Experiment	T[a] (°C)	Duration (h)	Basalt used	wt% basalt	F[b] (wt%)	Phases present[c]
515	1420	6	Leo12	9.5	25.9 ± 0.8	ol, opx, gt, qm
519	1380	12	Leo12	9.6	21.4 ± 1.2	ol, opx, gt, qm
522	1380	12	Leo12	9.8	19.9 ± 0.6	ol, opx, gt, qm
524	1370	13	Leo13	12.1	16.5 ± 1.0	ol, opx, gt, qm
525	1365	12	Leo13	15.3	12.0 ± 1.8	ol, opx, cpx, gt, qm
526	1350	12	Leo13	12.0	11.8 ± 0.6	ol, opx, cpx, gt, qm
527	1335	13	Leo13	15.4	11.4 ± 0.4	ol, opx, cpx, gt, qm
528	1320	21	Leo13	12.3	8.9 ± 0.6	ol, opx, cpx, gt, qm
529	1300	13	Leo13	12.7	7.9 ± 0.4	ol, opx, cpx, gt, qm
530	1280	12	Leo16	12.6	6.9 ± 0.6	ol, opx, cpx, gt, qm
531	1260	20	Leo16	11.9	5.8 ± 0.6	ol, opx, cpx, gt, qm

[a] Temperatures reported have been corrected for small variations in sample geometry using a thermal gradient of 3°C/mm, calibrated using 2 thermocouples (H. Soulard, pers. comm.).
[b] Melt fraction and 2 standard errors. See Appendix 4 for derivation.
[c] ol, olivine; opx, orthopyroxene; cpx, clinopyroxene; gt, garnet; qm, quench mat of crystals and interstitial glass.

oxide components except Al_2O_3, which is 13.5±8.0% relative higher in the quench mat analysis. Quenched liquids in lower temperature experiments were analysed using a rastered beam at 7500x magnification and a 3nA beam current. This was found to be the most effective method to limit alkali migration, when Na_2O content of the melt was relatively high. All analytical data were corrected using ZAF procedures.

H_2O in the liquid could not be measured directly because the liquid quenched to a mat of crystals and interstitial melt. Theoretical H_2O concentrations in the glasses were estimated using the bulk H_2O added to the charge and the proportion of liquid formed in the charge (see Appendix 1). Theoretical H_2O concentrations, adjusted for estimated H_2O loss (see below) are given in Table 4.3.

Table 4.3 H_2O content of melt and peridotite, and estimated H_2O loss in experiments at 3GPa.

Experiment	Melt H_2O[a] (wt%)	Peridotite H_2O[a] (wt%)	H_2O loss[b] (relative %)
515	2.87 ± 0.02	0.74 ± 0.03	1.91 ± 1.12
519	2.99 ± 0.03	0.64 ± 0.06	-10.95 ± 2.14
522	2.63 ± 0.03	0.52 ± 0.03	-5.83 ± 2.29
524	2.96 ± 0.04	0.49 ± 0.06	-10.44 ± 2.13
525	3.80 ± 0.04	0.46 ± 0.15	-6.32 ± 1.13
526	3.91 ± 0.02	0.46 ± 0.05	-5.71 ± 1.21
527	4.03 ± 0.01	0.46 ± 0.04	-9.07 ± 1.06
528	4.57 ± 0.01	0.41 ± 0.07	0.27 ± 1.06
529	5.15 ± 0.07	0.41 ± 0.10	-1.91 ± 1.07
530	6.99 ± 0.09	0.48 ± 0.09	-4.05 ± 0.94
531	8.30 ± 0.02	0.48 ± 0.10	-1.02 ± 0.82

[a] Theoretical H_2O content and 2 standard errors. Theoretical H_2O contents have been adjusted for estimated H_2O loss.
[b] Estimated H_2O loss and 2 standard errors. See Appendix 3 for derivation.

4.1.3 H_2O loss

Estimation of H_2O loss was based on the assumption that all H_2O loss occurs due to H_2 loss from the charge and accompanying Fe oxidation. H_2O loss (or gain) is therefore directly proportional to change in Fe_2O_3 in the bulk composition of the charge during the experiment. Change in Fe_2O_3 was estimated by mass balance (see Appendix 2), assuming Fe loss from the charge was negligible. Estimations of H_2O loss (in relative %) for all experiments are shown in Table 4.3. Changes in H_2O are small and range from a gain of 1.91% relative to a loss of 10.95% relative. Mean H_2O loss for all experiments is 4.83 ± 2.39wt% relative. H_2O loss shows no correlation with H_2O content of the liquid.

4.1.4 Peridotite H_2O

During a sandwich experiment, H_2O will be exchanged between melt in the peridotite layer and melt in the basalt layer until equilibrium is established. The H_2O content of the melt at the end of the experiment depends not only on the initial H_2O content of the peridotite starting mix, but also on the H_2O content of the basalt starting mix. The theoretical peridotite H_2O content required to produce the final melt H_2O content can be estimated using the H_2O content of the melt and the estimated degree of melting in the peridotite (see Appendix 3). Estimations of peridotite H_2O content for all experiments are given in Table 4.3.

H_2O saturation of LeoP1

In the subsolidus state, H_2O saturation of a peridotite defines the maximum H_2O content that can be stored in the equilibrium crystalline phases without the formation of a separate fluid phase. This depends on the abundance and identity of H_2O-bearing minerals present. The principal hydrous phase in the mantle at 3GPa is phlogopite, $K_2(Mg,Fe^{2+})_6Si_6Al_2O_{20}(OH)_4$ (Kushiro, 1970) but in a K_2O-free peridotite such as LeoP1, there is no major hydrous mineral stable at near-solidus temperatures and 3GPa. H_2O storage in LeoP1 at 3GPa is limited to the nominally anhydrous minerals (NAMs) olivine, opx, cpx and garnet, and is likely to have an upper limit of 0.1-0.15wt% (based on NAM H_2O contents estimated by Bell & Rossman (1992) and Kohn (1996)).

4.1.5 fO_2

Oxygen fugacity (fO_2) in these runs has been estimated from Fe^{3+}/FeO^* (total iron) ratios required for agreement between measured olivine-melt molar FeO-MgO distribution

coefficients and model values predicted by Ulmer (1989). fO_2 was calculated from the Fe^{3+}/FeO^* ratios in the glasses using the expression of Holloway *et al.* (1992), and results are shown in Table 4.4. Values of fO_2 are quoted relative to the QFM buffer at the experimental run temperature. The estimated range in is QFM+0.4 to QFM+3.0.

Table 4.4 Oxygen fugacity (fO_2) in experiments at 3GPa

Experiment	T[a](°C)	fO_2[b]
515	1420	0.4
519	1380	2.6
522	1380	1
523	1375	2.6
524	1370	2.5
525	1365	1.9
526	1350	2.4
527	1335	2.9
528	1320	1.1
529	1300	2.3
530	1280	3
531	1260	2.3

[a] Temperatures reported have been corrected for small variations in sample geometry using a thermal gradient of 3°C/mm, calibrated using 2 thermocouples (H. Soulard, pers. comm.).
[b] fO_2 relative to the quartz-fayalite-magnetite buffer at run temperature and 3GPa, and 2 standard errors. fO_2 estimated using the method of Holloway, Pan & Gudmundsson (1992). Fe^{3+}/FeO^* values used are given in Table 4.5.

4.2 Approach to equilibrium

All experiments except 515 were run for over 12 hrs and show effectively constant liquid composition. Run temperatures in these experiments are higher than those at 1.5GPa (see Table 3.2) so shorter run times were used to minimise thermocouple deterioration and softening of the AuPd capsule, which could increase Fe and H_2O loss. Experiment 515 was run for 6 hrs since the run temperature (1420°C) is close to the melting point of AuPd. Reaction kinetics are faster at higher pressure and temperature, however, aiding the approach to equilibrium.

Olivine crystals show no evidence of zoning and have a constant composition throughout the charge. Orthpyroxene (opx) and clinopyroxene (cpx) crystals are zoned in all these experiments. Cpx analyses show a trend from core to equilibrium rim of increasing Ca^{2+} and Al^{3+}, and opx analyses show a trend of increasing Al^{3+}, but little change in Ca^{2+}, as at 1.5GPa. Cpx and opx rim compositions were identified using the method discussed in section 3.2. Garnet typically forms large homogeneous crystals (0.2-1mm diameter), with numerous small (up to 10μm) inclusions of olivine, opx and cpx. This phenomenon is probably related to the nucleation kinetics of garnet.

4.3 Degree of Partial Melting as a Function of Temperature

The degree of partial melting in these experiments is estimated by a 2-stage mass balance method (see Appendix 4). The method is based on that of Robinson *et al.* (1998) and discussed in more detail in section 3.3. Results are presented in Table 4.2.

Melt fraction (F) is plotted against temperature in Figure 4.1. Temperature uncertainty for the piston cylinder apparatus at Bristol University is ±10-15°C, based on reproducibility of melt composition in sandwich experiments (Robinson *et al.*, 1998). Contours show estimated H_2O content in the peridotite. Data are also shown for anhydrous peridotite PHN-1611 (Kushiro, 1996), and for the estimated partial melting behaviour of LeoP1 under anhydrous conditions. For simplicity it was assumed that change in peridotite bulk composition affects the degree of melting at a given temperature, but does not affect (i) the composition of the melt and solid phases produced, or (ii) the relative abundances of the solid phases. Degree of melting in anhydrous LeoP1 was estimated by the two-stage mass balance method (Appendix 4), using phase composition data for partial melting of peridotites MPY and Tinaquillo Lherzolite (TL) (Robinson, unpubl.). For each experiment in this study, the relative abundances of the solid phases were estimated by mass balance of all phase compositions with the bulk composition of the parent peridotite (MPY or TL). Degree of melting in anhydrous LeoP1 at the same temperature was estimated by mass balancing all phase compositions and solid phase relative abundances to the bulk composition of LeoP1.

At F=5-12wt% in LeoP1+0.5wt% H_2O, melt fraction increases slowly with temperature, ≈1wt% per 15°C. With further melting, increase in F with temperature becomes very rapid, ≈1wt% per 4°C until cpx is eliminated from the peridotite melting residue. This appears to occur at a similar melt fraction (F=16-18wt%) irrespective of peridotite H_2O content. Melt fraction then increases more slowly with increasing temperature, ≈1wt% per 15°C. Garnet remains stable throughout the melting range studied. Data on hydrous peridotite melting rates at small melt fractions are not available. It is assumed that for a peridotite with 0.5wt% H_2O, melting will start at the H_2O-saturated solidus at ≈1000°C (Kushiro, 1970; Green, 1973; Milhollen *et al.*, 1974) and will gradually become more rapid with increasing temperature. In anhydrous peridotite, F increases very rapidly (≈1wt% per 3°C) from the solidus until cpx is eliminated. At larger melt fractions, increase in F with temperature is similar to that in hydrous peridotite (≈1wt% per 15°C). Garnet is eliminated from the anhydrous peridotite residue at F≈10wt%, but the anhydrous melting data suggest that there is no inflection in the slope of F vs temperature at this point.

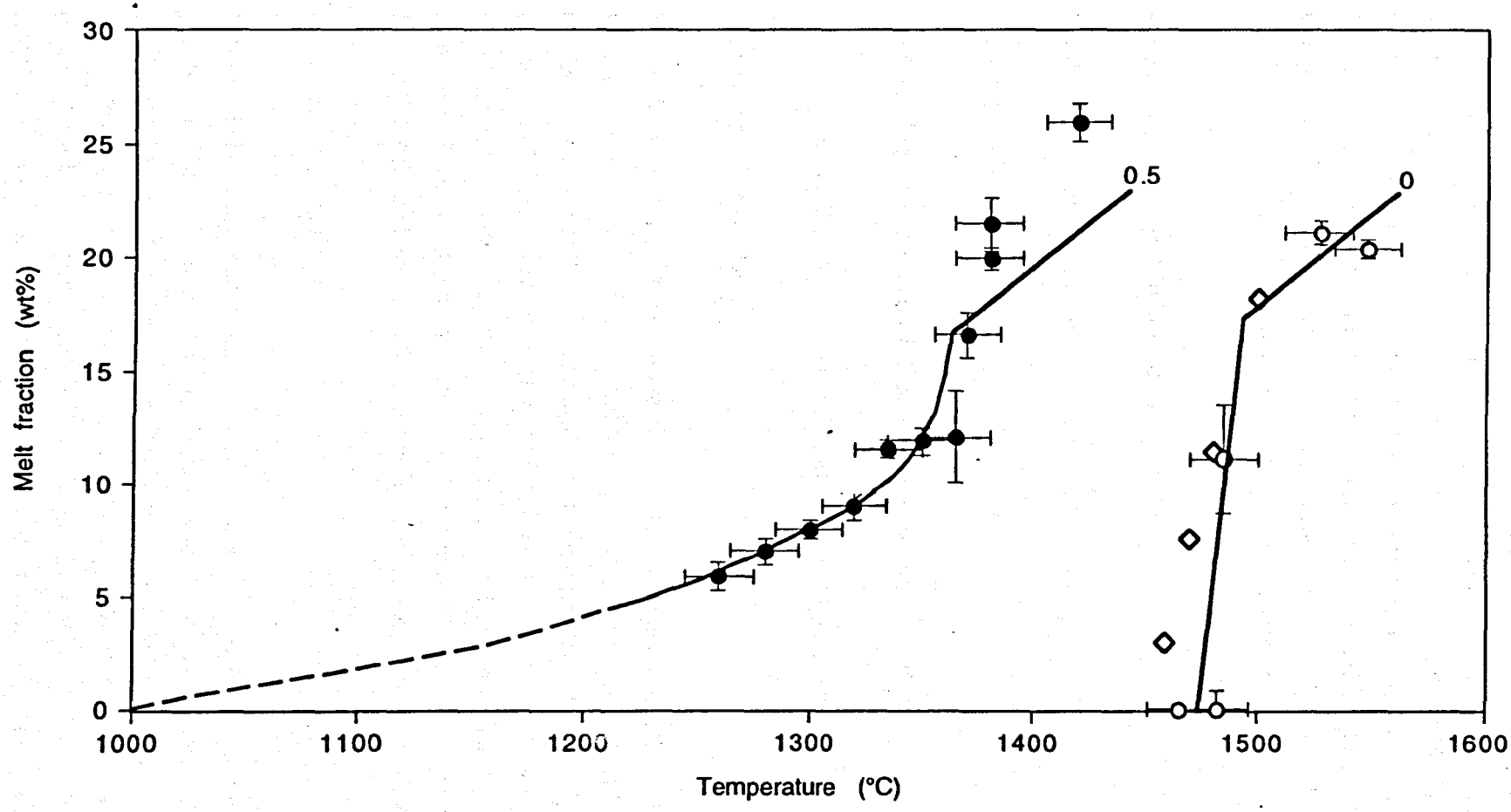

Figure 4.1 Degree of melting as a function of temperature and peridotite H_2O content at 3GPa. Contour values show peridotite H_2O in wt%. Broken lines indicate approximate location of contour. Black-filled circles = LeoP1+ 0.6-0.79 wt% H_2O, grey-filled circles = LeoP1+ 0.4-0.59 wt% H_2O, open circles = anhydrous equivalent of LeoP1(see text for details), diamonds = PHN-1611, anhydrous (Kushiro, 1996). Error bars for melt fraction represent 2 standard errors.

In general terms, the addition of water to peridotite at 3GPa has a similar effect on F vs temperature as at 1.5GPa: (i) for a given melt fraction, melting occurs at a lower temperature, i.e. the contour for F vs temperature is shifted down-temperature, (ii) the scale of the down temperature shift in F vs temperature is greatest at the solidus and decreases with degree of melting. A significant difference, however, is that at 3GPa there is no major hydrous phase controlling onset of melting in LeoP1, as amphibole does in Leo3 at 1.5GPa. Melting of hydrous peridotite at 3GPa will start at the H_2O-saturated solidus, irrespective of peridotite H_2O content. An exception to this might be a K_2O-enriched peridotite in which onset of melting is buffered by phlogopite stability.

4.4 Solid phase equilibria and composition

Solid phase compositions are given in Table 4.5.

4.4.1 Olivine

Apparent Mg-Fe partition coefficients for olivine and melt ($K_D^{Mg\text{-}Fe}$ ol-m) are calculated as:

$$\text{apparent } K_D^{Mg\text{-}Fe} \text{ ol-m} = (MgO/FeO^*)_{melt} / (MgO/FeO^*)_{olivine}$$

assuming all Fe to be Fe^{2+}.

Values for apparent $K_D^{Mg\text{-}Fe}$ ol-m are given in Table 4.5 and range from 0.19-0.29. These values are lower than those predicted for $K_D^{Mg\text{-}Fe}$ ol-m at 3GPa (0.376±0.006) by Ulmer (1989). This is due to the presence of Fe^{3+} in the melt under the relatively oxidising conditions of these experiments (fO_2>QFM+0.4). Apparent $K_D^{Mg\text{-}Fe}$ ol-m does not change significantly with increasing melt fraction, except for 1 experiment at high melt fraction (see Figure 4.2). Small-scale variations in apparent $K_D^{Mg\text{-}Fe}$ are likely to be correlated with Fe^{3+} in the melt, and due to differences in fO_2 conditions among experiments.

4.4.2 Orthopyroxene

Figure 4.3 shows opx compositions recalculated as molecular olivine (Ol), diopside (Di), jadeite+calcium tschermakite (Jd+CaTs) and quartz (Qz), and plotted using a Di projection (Falloon & Green, 1988). Opx compositions in hydrous and anhydrous peridotite are very similar, though opx in hydrous peridotite is slightly richer in enstatite (En, $MgFeSi_2O_6$) and poorer in Jd+CaTs. Higher En content is due to the lower temperature of melting in hydrous peridotite, and the sensitivity of co-existing opx and

Table 4.5 Experimental phase compositions produced at 3GPa

Experiment	Phase[a]	No.[b]	Na_2O	MgO	SiO_2	Al_2O_3	CaO	TiO_2	FeO*	Cr_2O_3	NiO	Mg#[c]	Total[d]	K_D[e]	Fe_2O_3/FeO*[f]
515	Liq	66	1.52[8][g]	19.59[40]	45.70[80]	12.66[42]	10.80[18]	0.63[4]	8.81[36]	0.23[2]	0.06[2]	0.80	94.37	0.29	0.22
	Ol	20	0.03[2]	50.79[28]	41.75[10]	0.14[4]	0.26[10]	0.00[0]	6.76[6]	0.07[2]	0.09[2]	0.93	102.35		
	Opx	4	0.20[4]	32.10[72]	55.20[130]	4.76[38]	2.42[24]	0.02[2]	4.60[8]	0.63[8]	0.07[4]	0.93	100.47		
	Garnet	17	0.03[2]	21.88[30]	42.96[46]	22.12[68]	5.48[32]	0.13[2]	5.49[28]	1.76[24]	0.04[2]	0.88	102.08		
519	Liq	113	1.62[12]	17.44[38]	44.67[80]	12.56[44]	10.99[38]	0.81[6]	11.72[48]	0.12[2]	0.08[2]	0.75	95.23	0.21	0.43
	Ol	20	0.03[2]	51.69[18]	41.10[12]	0.11[2]	0.18[2]	0.00[0]	6.51[8]	0.03[2]	0.34[2]	0.93	100.11		
	Opx	2	0.19[6]	31.80[28]	52.48[50]	6.99[16]	1.76[8]	0.07[2]	6.26[28]	0.29[6]	0.14[10]	0.90	99.75		
	Garnet	13	0.03[2]	22.38[20]	42.02[14]	21.78[16]	6.17[18]	0.13[2]	6.20[16]	1.14[16]	0.05[2]	0.87	100.12		
522	Liq	145	2.30[12]	17.36[22]	45.42[46]	11.99[26]	11.09[20]	1.15[4]	10.47[24]	0.13[0]	0.08[0]	0.77	94.66	0.28	0.27
	Ol	11	0.03[2]	50.97[22]	40.70[12]	0.09[2]	0.18[2]	0.00[0]	7.64[14]	0.05[2]	0.35[4]	0.92	100.36		
	Opx	3	0.25[0]	31.65[28]	53.57[32]	6.06[18]	1.65[2]	0.05[2]	6.02[8]	0.65[10]	0.17[4]	0.91	98.87		
	Garnet	10	0.05[2]	22.39[18]	42.57[36]	22.43[20]	4.98[14]	0.18[4]	6.23[16]	1.05[8]	0.03[4]	0.87	97.67		
524	Liq	28	2.32[36]	17.03[56]	43.88[144]	13.21[54]	9.90[60]	1.22[14]	12.21[128]	0.13[2]	0.09[2]	0.73	92.21	0.22	0.42
	Ol	77	0.04[0]	50.71[10]	41.27[8]	0.12[2]	0.20[2]	0.00[0]	7.36[4]	0.04[0]	0.30[2]	0.92	99.63		
	Opx	4	0.29[14]	31.76[52]	53.65[38]	5.96[36]	1.70[14]	0.09[6]	5.96[18]	0.48[8]	0.12[4]	0.91	99.60		
	Garnet	40	0.04[2]	22.14[14]	42.81[30]	21.28[38]	5.88[28]	0.16[2]	6.66[12]	1.05[4]	0.04[0]	0.86	98.28		
525	Liq	150	2.10[[12]	14.89[38]	40.53[58]	14.42[34]	9.42[20]	1.21[4]	11.28[34]	0.15[2]	0.12[2]	0.74	93.18	0.24	0.36
	Ol	132	0.03[0]	51.05[8]	40.60[8]	0.12[2]	0.19[2]	0.00[0]	7.68[4]	0.00[0]	0.33[2]	0.92	99.16		
	Opx	2	0.19[4]	32.67[2]	53.45[10]	5.41[12]	1.45[8]	0.05[6]	6.34[10]	0.50[14]	0.14[14]	0.91	98.79		
	Cpx	4	1.30[6]	18.40[22]	51.97[24]	5.41[30]	17.28[12]	0.13[2]	4.97[20]	0.51[10]	0.05[4]	0.87	98.51		
	Garnet	41	0.03[0]	22.57[8]	42.21[6]	22.07[6]	5.46[6]	0.15[0]	6.62[10]	0.91[4]	0.04[2]	0.86	99.44		
526	Liq	123	2.44[10]	15.99[38]	45.49[66]	13.45[36]	10.06[28]	1.19[4]	11.12[26]	0.16[2]	0.16[2]	0.72	87.48	0.22	0.42
	Ol	69	0.03[0]	50.84[10]	40.94[8]	0.11[2]	0.21[4]	0.00[0]	7.57[4]	0.04[0]	0.31[2]	0.92	100.78		
	Opx	4	0.21[2]	31.94[22]	53.13[62]	6.54[14]	1.47[6]	0.07[2]	6.22[24]	0.32[8]	0.13[8]	0.90	99.08		
	Cpx	3	1.34[2]	19.02[14]	52.52[18]	4.81[8]	17.06[14]	0.12[4]	4.66[14]	0.47[6]	0.11[6]	0.88	98.09		
	Garnet	10	0.02[2]	21.92[18]	42.36[20]	22.12[12]	5.66[12]	0.15[0]	6.60[18]	1.17[8]	0.02[2]	0.86	98.85		

Table 4.5 (continued)

Experiment	Phase	No.	Na_2O	MgO	SiO_2	Al_2O_3	CaO	TiO_2	FeO*	Cr_2O_3	NiO	Mg#	Total	K_D	Fe_2O_3/FeO^*
527	Liq	104	2.39[8]	16.38[24]	44.00[38]	13.62[28]	10.23[14]	1.25[4]	12.02[26]	0.13[2]	0.11[2]	0.71	89.77	0.19	0.48
	Ol	116	0.03[0]	51.32[10]	40.66[6]	0.15[4]	0.20[2]	0.00[0]	7.34[4]	0.04[0]	0.30[2]	0.93	101.29		
	Opx	2	0.23[4]	31.70[60]	53.32[26]	6.19[32]	1.54[8]	0.08[4]	6.28[18]	0.54[10]	0.17[10]	0.90	99.30		
	Cpx	4	1.29[6]	18.81[58]	52.64[52]	5.10[38]	17.04[22]	0.12[2]	4.56[26]	0.41[18]	0.08[2]	0.88	99.42		
	Garnet	9	0.03[2]	22.28[18]	42.21[10]	22.25[18]	5.49[14]	0.18[4]	6.74[26]	0.83[16]	0.04[2]	0.85	100.33		
528	Liq	72	2.31[20]	15.91[66]	44.91[90]	14.90[38]	10.39[44]	1.41[16]	10.07[78]	0.14[2]	0.11[2]	0.74	89.19	0.26	0.30
	Ol	82	0.03[0]	50.03[8]	41.01[8]	0.09[2]	0.17[2]	0.00[0]	8.35[4]	0.04[0]	0.32[2]	0.91	100.18		
	Opx	2	0.22[2]	31.74[56]	53.79[60]	6.08[98]	1.51[22]	0.06[6]	6.18[32]	0.42[4]	0.04[2]	0.90	99.55		
	Cpx	3	1.33[2]	18.00[22]	52.76[40]	5.34[22]	17.40[26]	0.10[4]	4.25[36]	0.77[14]	0.10[8]	0.88	99.64		
	Garnet	33	0.02[0]	21.88[8]	42.46[14]	22.25[10]	5.41[4]	0.18[2]	6.64[10]	1.17[6]	0.04[2]	0.85	99.62		
529	Liq	112	2.36[6]	16.75[38]	43.96[54]	13.57[22]	9.89[14]	1.22[4]	12.01[24]	0.12[2]	0.12[2]	0.71	90.03	0.22	0.40
	Ol	115	0.04[0]	50.32[8]	40.76[6]	0.12[4]	0.18[2]	0.01[0]	8.19[4]	0.04[0]	0.38[2]	0.92	99.73		
	Opx	4	0.25[6]	32.17[36]	53.30[52]	5.82[18]	1.44[14]	0.06[2]	6.45[12]	0.36[10]	0.18[6]	0.90	99.96		
	Cpx	3	1.42[2]	17.64[22]	51.98[40]	5.54[22]	17.61[26]	0.14[4]	5.13[36]	0.45[14]	0.07[8]	0.86	98.50		
	Garnet	19	0.03[2]	21.78[10]	42.20[18]	22.47[6]	5.44[6]	0.16[0]	6.91[10]	1.01[4]	0.05[2]	0.85	99.23		
530	Liq	133	3.49[8]	15.56[44]	43.50[52]	16.18[48]	8.37[14]	1.49[4]	11.14[24]	0.15[2]	0.12[2]	0.71	89.73	0.19	0.49
	Ol	53	0.03[0]	50.53[8]	41.77[8]	0.10[4]	0.14[2]	0.01[0]	6.94[4]	0.04[2]	0.50[2]	0.93	101.22		
	Opx	3	0.24[2]	32.20[40]	55.22[10]	4.77[16]	1.18[8]	0.10[8]	5.86[16]	0.38[6]	0.09[6]	0.91	100.68		
	Cpx	3	1.87[14]	17.05[10]	53.68[36]	4.87[8]	17.01[10]	0.17[4]	4.77[12]	0.50[8]	0.08[2]	0.86	100.33		
	Garnet	22	0.04[2]	21.63[18]	42.41[8]	21.90[10]	5.52[16]	0.18[2]	7.05[10]	1.27[8]	0.06[2]	0.85	99.92		
531	Liq	47	3.63[10]	14.21[72]	44.27[88]	17.98[88]	8.25[30]	1.52[6]	9.89[36]	0.13[2]	0.11[4]	0.71	88.70	0.22	0.42
	Ol	87	0.03[0]	50.11[12]	41.29[10]	0.07[2]	0.15[2]	0.01[0]	7.87[4]	0.04[0]	0.48[1]	0.92	100.64		
	Opx	3	0.21[2]	32.25[50]	54.00[30]	5.49[44]	1.28[12]	0.04[0]	6.12[30]	0.54[6]	0.17[18]	0.90	99.68		
	Cpx	4	1.68[10]	17.15[18]	52.82[24]	4.91[48]	17.89[36]	0.13[4]	4.68[20]	0.70[6]	0.04[6]	0.86	99.58		
	Garnet	20	0.02[2]	22.12[10]	42.49[8]	21.69[10]	5.37[10]	0.18[2]	6.75[12]	1.39[6]	0.05[2]	0.85	99.13		

Table 4.5 (continued)

Experiment	Phase	No.	Na_2O	MgO	SiO_2	Al_2O_3	CaO	TiO_2	FeO*	Cr_2O_3	NiO	Mg#	Total	K_D	Fe_2O_3/FeO^*
L12[h]	Glass	10	2.14[4]	15.76[9]	45.13[20]	11.48[7]	11.00[6]	0.78[2]	9.01[13]	0.02[2]	0.02[2]	0.76	95.32		
M2[i]	Qm	45	2.12[24]	16.34[69]	44.98[104]	13.03[85]	10.93[59]	0.77[10]	8.74[59]	0.02[1]	0.03[1]	0.77	96.90		

[a] All Fe as Fe^{2+}.

[b] Liq, liquid; Ol, olivine; Opx, orthopyroxene; Cpx, clinopyroxene; Qm = quench mat. Orthopyroxene and clinopyroxene analyses are rim compositions.

[c] Number of analyses of each phase.

[d] Mg# = molar MgO/(MgO+FeO*), assuming all Fe as Fe^{2+}.

[e] Original probe analysis total. All probe analyses have been normalised to 100wt%.

[f] $K_D = K_D^{Mg\text{-}Fe}$ olivine-melt = $(FeO^*/MgO)_{ol}/(FeO^*/MgO)_{melt}$, assuming all Fe as Fe^{2+}.

[g] Fe^{3+} estimated such that $K_D^{Mg\text{-}Fe}$ olivine-melt gives agreement with model value (0.337 ± 0.004) at 3.0GPa (Ulmer, 1989).

[h] Values in square brackets represent 2 standard errors of the analysed compositional range in terms of least units cited, e.g. 1.52[8] should be read as 1.52 ± 0.08.

[i] Starting mix Leo12 run at 0.5GPa, 1300°C, 0.5hrs, and quenched to glass.

[j] Starting mix Leo12 run at 3GPa, 1300°C, 0.5hrs, and quenched to mat of crystals and interstitial glass.

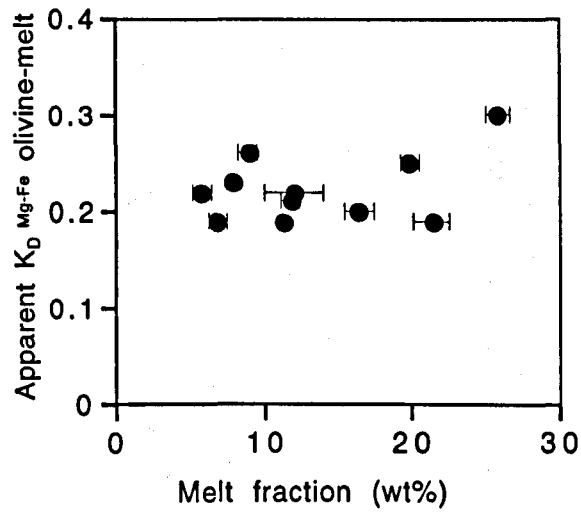

Figure 4.2 Variation in apparent $K_D^{Mg\text{-}Fe}$ olivine-melt with melt fraction at 3GPa. Apparent $K_D^{Mg\text{-}Fe}$ olivine-melt = $(FeO^*/MgO)_{olivine}/(FeO^*/MgO)_{melt}$.

cpx compositions to temperature. Lower Jd+CaTs content is likely to be due to a change in partitioning of Al_2O_3 between opx, cpx and garnet with decrease in temperature of melting. In general, however, adding H_2O to peridotite has little effect on opx composition.

The effect of increasing pressure is to increase the extent of En solid solution in cpx (Takahashi, 1986), and to slightly decrease the MgTs component in opx by stabilising garnet. In general, opx composition does not change much with increasing pressure, but it becomes less abundant.

4.4.3 Clinopyroxene

Figure 4.4 shows cpx compositions recalculated as molecular olivine, diopside, Jd+CaTs and quartz, and plotted using a Jd+CaTs projection (Falloon & Green, 1988). Cpx compositions in hydrous peridotite at 3GPa are enriched in Di and depleted in En relative to cpx in anhydrous peridotite, since addition of water lowers the temperature of peridotite melting. Cpx compositions at 3GPa are plotted in terms of Al_2O_3 vs melt fraction in Figure 4.5. Cpx in hydrous peridotite is depleted in Al_2O_3 (CaTs) relative to cpx in anhydrous peridotite. This may result from a change in partitioning of Al_2O_3 between cpx, opx and garnet due to the lower temperatureof melting in hydrous peridotite.

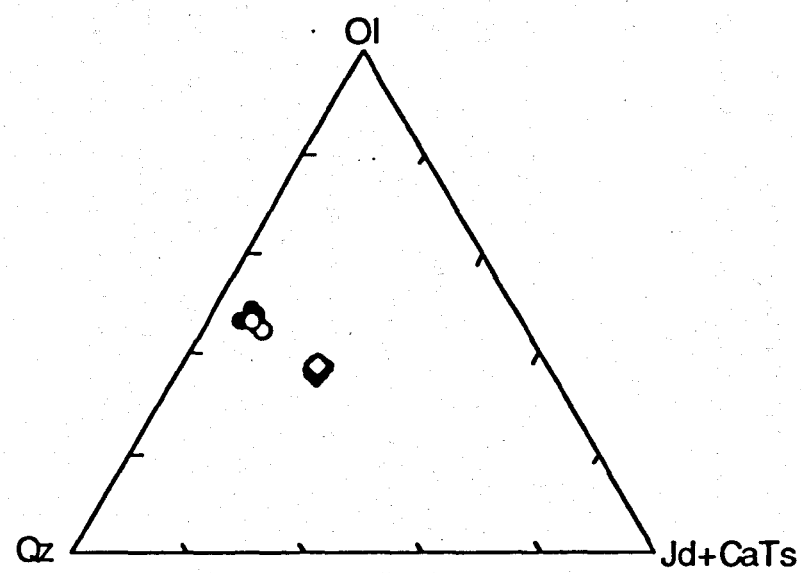

Figure 4.3 Projected orthopyroxene (opx) and garnet compositions in peridotite at 3GPa, in the CIPW molecular normative tetrahedron. Projection from diopside (Di) onto the base olivine (Ol)-jadeite + calcium tschermakite (Jd+CaTs)-Quartz (Qz). Filled circles = opx in LeoP1, open circles = opx in MPY and TL (Robinson, unpubl.), filled diamonds = garnet in LeoP1, open diamonds = garnet in MPY and TL.

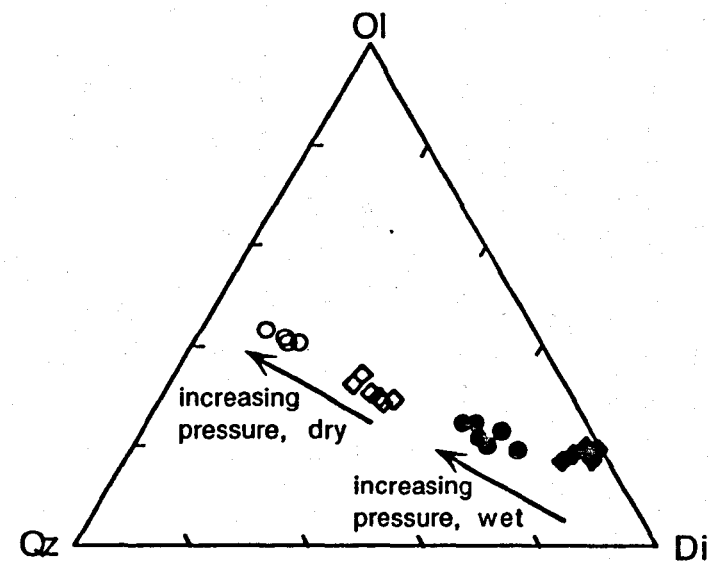

Figure 4.4 Projected clinopyroxene (cpx) compositions in peridotite at 1.5-3GPa, in the CIPW molecular normative tetrahedron. Projection from jadeite + calcium tschermakite (Jd+CaTs) onto the base olivine (Ol)-Diopside (Di)-Quartz (Qz). Filled circles = LeoP1 at 3.0GPa, open circles = MPY and TQ at 3GPa (Robinson, unpubl.), filled diamonds = LeoP1 at 1.5GPa, open diamonds = MPY at 1.5GPa (Robinson et al, 1998). Fe^{3+}/FeO^* assumed to be 0.1. * All Fe as FeO.

Cpx compositions in Figure 4.4 demonstrate that the effect of increasing pressure is to increase the extent of En solid solution in cpx (Takahashi, 1986). Figure 4.6 shows cpx compositions in hydrous peridotite at 3GPa and 1.5GPa in terms of Na_2O and Al_2O_3 vs melt fraction. At 3GPa, cpx is enriched in Na_2O (≈0.25wt%) and depleted in Al_2O_3 (≈2wt%) relative to cpx at 1.5GPa. This is due to the increased stability of the cpx Jd component with pressure (Blundy *et al.*, 1995) and the decreased stability of the cpx CaTs component relative to the grossular component in garnet (Gudfinnsson & Presnall, 1996).

The melt fraction at which cpx is eliminated from the peridotite residue (cpx-out) is similar (F=16-18wt%) for hydrous LeoP1 and anhydrous MPY at 3GPa. This reflects the fact that LeoP1 and MPY have very similar CaO/Al_2O_3 ratios (see Table 4.1). Cpx is stable to higher melt fractions (F=20-22wt%) for hydrous Leo3 and anhydrous MPY at 1.5GPa (see section 3.3.1). This is because the lherzolite melting reactions at 1.5GPa and 3GPa differ (see section 4.6), so that the stoichiometric proportion of cpx entering the melt is greater at 3GPa than at 1.5GPa.

In summary, adding H_2O to peridotite at 3GPa has a significant effect on cpx composition by lowering the temperature of melting. This enriches cpx in the Di component, and stabilises garnet so that cpx is depleted in Al_2O_3 relative to cpx in anhydrous peridotite at 3GPa. The effect of increasing pressure from 1.5GPa to 3GPa is to increase the En and Jd components in cpx in hydrous peridotite, to decrease the CaTs component and to change the peridotite melting reaction so that cpx-out occurs at smaller melt fraction.

4.4.4 Garnet

Figure 4.3 shows garnet compositions recalculated as molecular olivine, diopside, Jd+CaTs and quartz, and plotted using a Di projection (Falloon & Green, 1988). Compositions of garnet in hydrous peridotite (this study) and in anhydrous peridotite (Robinson, unpubl.) are very similar ($py_{78}al_8gr_{14}$), and show little variation with extent of melting. In hydrous peridotite LeoP1, garnet is stable throughout the melting range studied (F=5-23wt%). In anhydrous peridotite, garnet is eliminated from the peridotite residue at F≈10-12wt%. Garnet stability is likely to be sensitive to temperature, and garnet may remain stable to higher melt fractions in hydrous peridotite due to the lower temperature of melting. In summary, adding H_2O to peridotite at 3GPa has no significant effect on garnet composition, but garnet remains stable to a larger degree of melting.

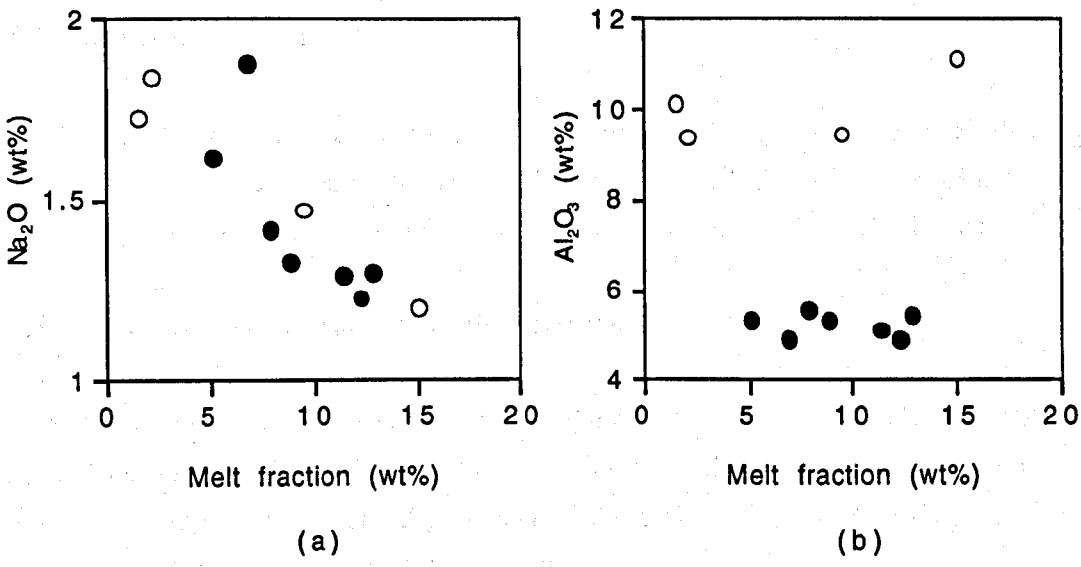

Figure 4.5 Variation in (a) Na_2O and (b) Al_2O_3 in clinopyroxene at 3.0GPa. Black-filled circles = hydrous peridotite LeoP1, open circles = anhydrous peridotites MPY and TL (Robinson, unpubl.),

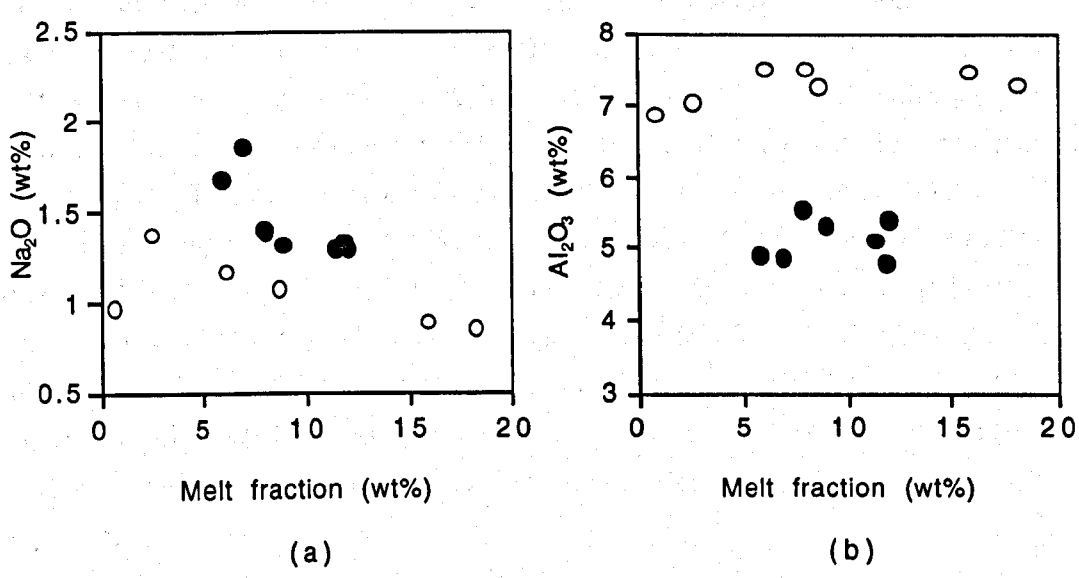

Figure 4.6 Variation in (a) Na_2O and (b) Al_2O_3 in clinopyroxene in hydrous peridotite at 1.5GPa and 3.0GPa. Black-filled circles = LeoP1 at 3.0GPa, open circles = Leo3 at 1.5GPa.

4.5 Liquid composition

Liquid compositions are given in Table 4.5. Fe^{3+} in the melt was calculated such that $K_D^{Mg\text{-}Fe}$ ol-m agrees with the value predicted at 3GPa (0.376±0.006) by Ulmer (1989). All liquid compositions are given on a volatile-free basis, i.e. for oxide totals=100wt%.

4.5.1 Variation in oxide content of the melt with F

Figure 4.7 shows variation in oxide content of the melt with degree of melting for MgO, FeO*, CaO, Na_2O, TiO_2, Al_2O_3 and SiO_2. Variation in oxide content of the melt with degree of melting is shown for anhydrous peridotites MPY, TL and PHN-1611 (Robinson, unpubl.; Kushiro, 1996) for comparison.

MgO content increases steadily in the liquid as extent of melting increases. MgO is similar in hydrous and anhydrous melts at all melt fractions.

FeO* increases slightly in hydrous liquids with increase in extent of melting until F=10wt%, then remains approximately constant. Melt in the highest temperature experiment (515) is anomalously low in FeO*, and mass balance calculations suggest that FeO* has been lost from the charge. Anhydrous melts of MPY and TL show a broadly similar trend with little variation in FeO* content, but values are ~5wt% lower than in the hydrous liquids. This difference can be explained by differences in oxidation state, with the more oxidising conditions of this study ($fO_2 \geq$QFM+0.4) producing more FeO*-rich melts which contain significant amounts of Fe^{3+}. Experiments using PHN-1611 were carried out under more reducing conditions (approximately fO_2=QFM-2), but this effect is offset by the high FeO* content of PHN-1611 relative to LeoP1. The observed variation in melt FeO* between hydrous and anhydrous peridotites is therefore likely due to differences in peridotite bulk composition, and in oxidation conditions during melt generation.

CaO increases in the liquid with increase in extent of melting. until cpx is eliminated from the peridotite residue, at F~17wt%. CaO decreases in the liquid as melting increases above F=17wt%, due to dilution. CaO is similar in hydrous and anhydrous melts at allmelt fractions.

Na_2O content of the liquid decreases with increasing degree in melting. At moderate and large melt fractions (F>10wt%), Na_2O contents in partial melts of hydrous peridotite are similar to those of anhydrous peridotite. At smaller melt fractions, Na_2O in the hydrous

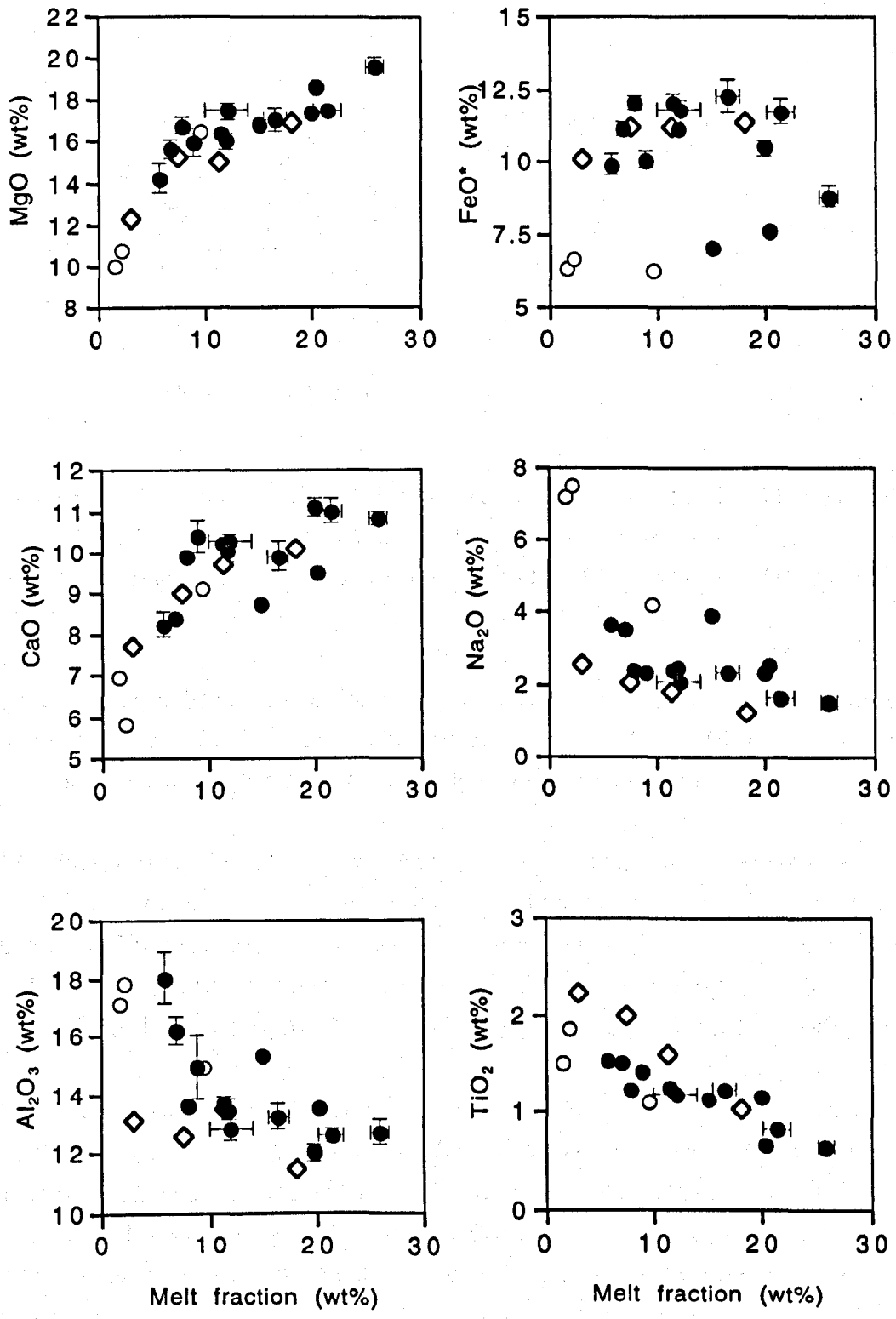

Figure 4.7 Variation in oxide content of liquid with melt fraction at 3.0GPa. Black-filled circles = LeoP1 (this study), open circles = MPY (Robinson, unpubl.), grey-filled circles = TL (Robinson, unpubl.), diamonds = PHN-1611 (Kushiro, 1996). Melt H_2O contents are given in Table 4.5. Error bars represent 2 standard errors.* All Fe as Fe^{2+}.

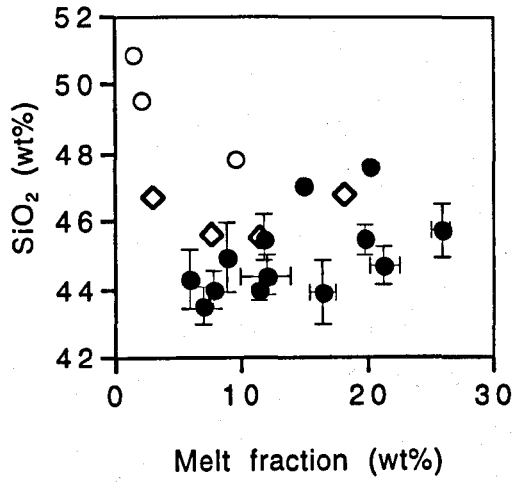

Figure 4.7 contd. Symbols as on previous page.

liquid is lower than in melts of MPY but greater than in melts of PHN-1611 at equivalent melt fraction. This is likely to be due to differences in peridotite bulk composition, since LeoP1 has an intermediate Na_2O content (0.4wt%) to MPY (0.5wt%) and PHN-1611 (0.3wt%).

TiO_2 decreases in the liquid with increasing degree of melting. A similar trend in observed in anhydrous melts. Slightly higher TiO_2 contents in melts of PHN-1611 at small melt fractions result from higher TiO_2 in the peridotite bulk composition.

Al_2O_3 decreases rapidly in the liquid with increasing melting until cpx-out (F≈16wt%), then decreases more slowly with further melting. Al_2O_3 is slightly lower than in melts of TL at F=10-20wt%, due to the stabilisation of garnet to larger melt fractions in hydrous peridotite. Al_2O_3 content is similar in melts of MPY at F<10wt%. Al_2O_3 is much lower in melts of PHN-1611 and is probably due to low Al_2O_3 in the peridotite bulk composition.

SiO_2 remains roughly constant in the liquid until cpx-out (F≈16wt%) and increases slightly with further melting. SiO_2 in anhydrous liquids decreases with extent of melting until cpx-out, then increases slightly with further melting. Melting trends in SiO_2 are similar in hydrous and anhydrous liquids for F>10wt%. More data on hydrous melt compositions are needed to adequately compare SiO_2 melt contents at smaller melt fractions.

4.5.2 Normative liquid compositions

Figure 4.8 shows melt compositions recalculated as molecular olivine, diopside, quartz and jadeite + calcium tschermakite, and plotted using a diopside projection (Falloon & Green, 1988). Enstatite (En) composition is shown on the Ol-Qz join. Liquid

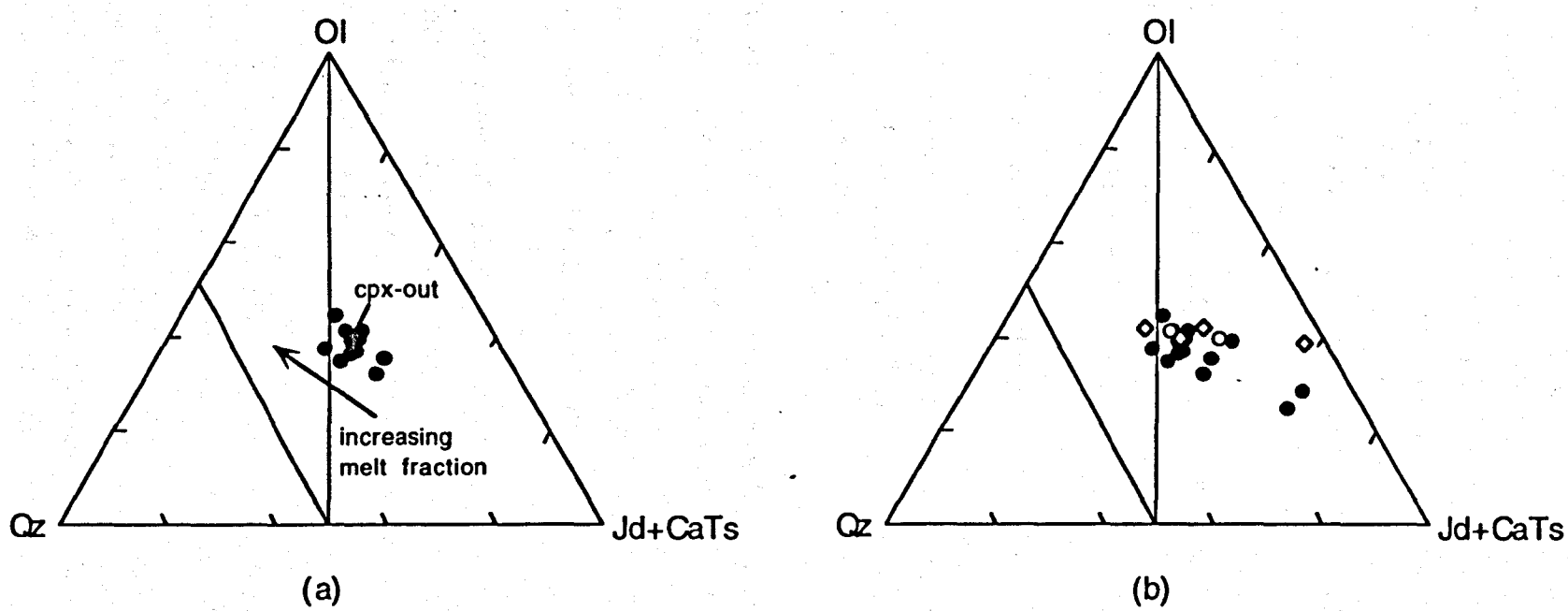

Figure 4.8 Projected liquid compositions at 3GPa, in the CIPW molecular normative tetrahedron. Projection from diopside (Di) onto the base olivine (Ol)-jadeite + calcium tschermakite (Jd+CaTs)-Quartz (Qz). En = enstatite. Values for Fe^{3+}/FeO^* in hydrous liquids given in Table 4.5. * All Fe as FeO. (a) Liquid compositions for partial melting of LeoP1. Cpx-out = point of clinopyroxene elimination. (b) Comparison of liquid compositions for partial melting of hydrous and anhydrous peridotite. Filled circles = hydrous partial melts of LeoP1 (this study), open circles = anhydrous partial melts of TL (Robinson, unpubl.), open circles = anhydrous partial melts of MPY (Robinson, unpubl.), diamonds = anhydrous partial melts of PHN-1611 (Kushiro, 1996). Fe^{3+}/FeO^* in anhydrous liquids assumed to be 0.1.

compositions formed at small melt fractions (F=6wt%) from hydrous peridotite plot towards the Ol-Jd-CaTs join and are Ne normative. As melting increases, the liquid composition moves towards the Ol-Opx join (Figure 4.8a). Liquids formed from hydrous and anhydrous peridotite have similar normative compositions (Figure 4.8b), but the hydrous liquids appear slightly depleted in Ol relative to the anhydrous. This is due to higher Fe_2O_3/FeO* in the more oxidised hydrous melts (see section 4.5) which increases normative magnetite at the expense of ol. Variation in normative liquid composition at small melt fractions is primarily controlled by melt Na_2O content and therefore peridotite bulk composition.

In summary, hydrous and anhydrous melts have similar compositions at 3GPa. Melt composition is more sensitive to variation in peridotite bulk composition and fO_2 than to peridotite H_2O content at this pressure.

4.5.3 Effect of pressure on liquid composition

Figure 4.9 shows variation in oxide content of the melt with degree of melting for hydrous peridotite Leo3 at 1.5GPa and LeoP1 at 3GPa. Peridotite bulk compositions are given in Tables 3.1 and 4.1.

MgO and **FeO*** content increases in the liquid with increasing pressure. MgO is increased by ≈5wt% and FeO* is increased by ≈2.5wt% at all F. Increase in pressure decreases the olivine liquidus phase volume (Presnall *et al.*, 1978), therefore liquids at a higher pressure contain a greater olivine component. The trends in MgO vs F and FeO* vs F are similar at 1.5GPa and 3GPa.

CaO content of the liquid decreases slightly (≈1wt%) with increasing pressure due to the increase in the olivine component in the melt. The trend in CaO vs F is similar at 1.5GPa and 3GPa: CaO increases with melting to a maximum at cpx-out, then decreases with further melting. Cpx-out occurs at a smaller degree of melting with increasing pressure.

Na_2O is decreased in the liquid with increasing pressure. This is due to the increased stability of Jd in cpx with pressure (Blundy *et al.*, 1995). Na_2O is also likely to be slightly higher in melts of Leo3since the peridotite bulk composition is Na_2O-enriched. At F<5wt% at 1.5GPa amphibole is stable, increasing D^{Na2O} peridotite-melt and producing an inflection in the Na_2O vs F trend. At 3GPa amphibole is not stable, therefore Na_2O is expected to continue to increase with decreasing F, and may approach the values observed in near-solidus melts at lower pressure.

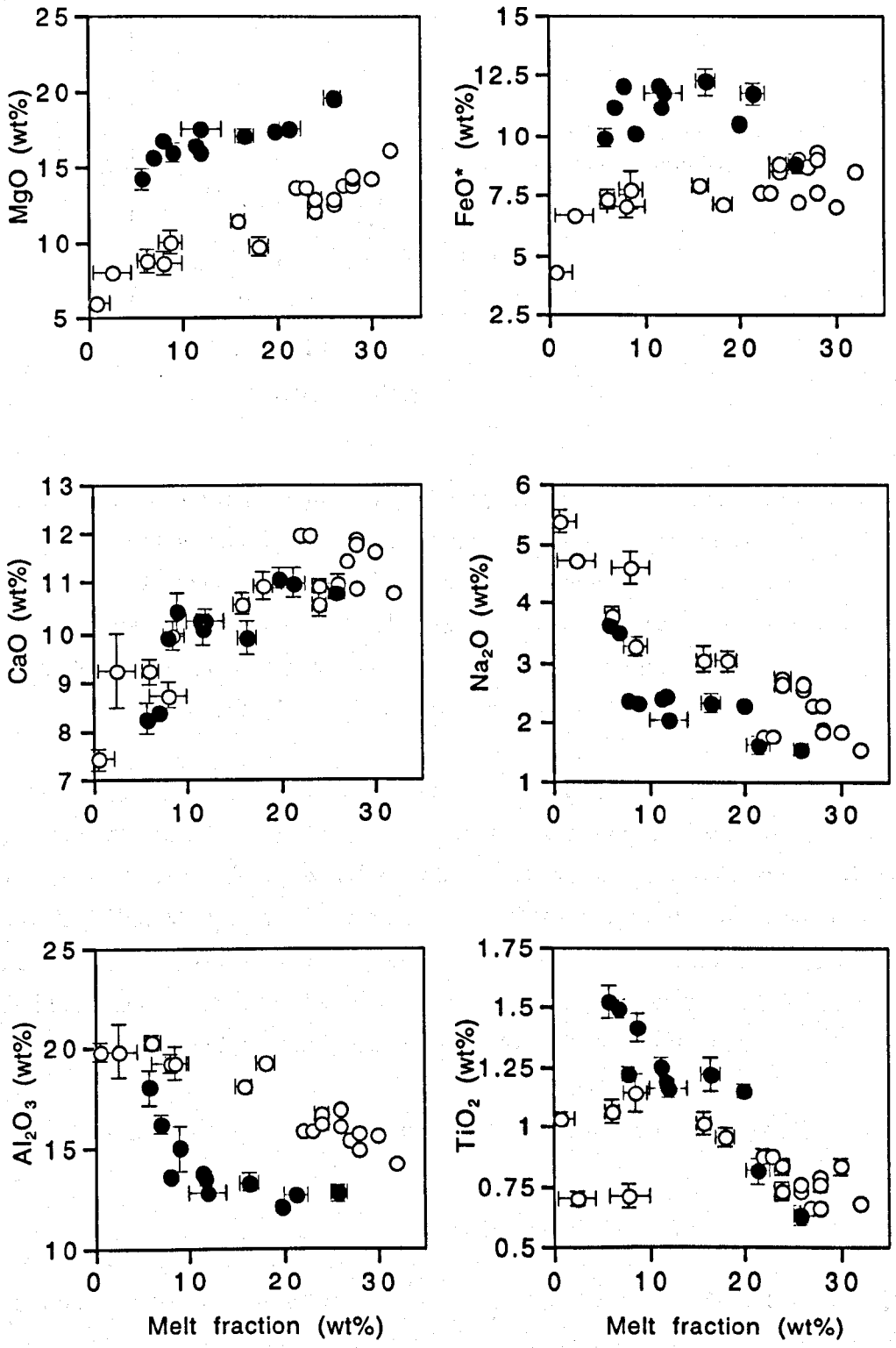

Figure 4.9 Variation in oxide content of partial melts of hydrous peridotite at 1.5GPa and 3.0GPa. Black-filled circles = LeoP1 at 3.0GPa, open circles = Leo3 at 1.5GPa. Melt compositions are given in Tables 3.5 and 4.5. Error bars represent 2 standard errors.

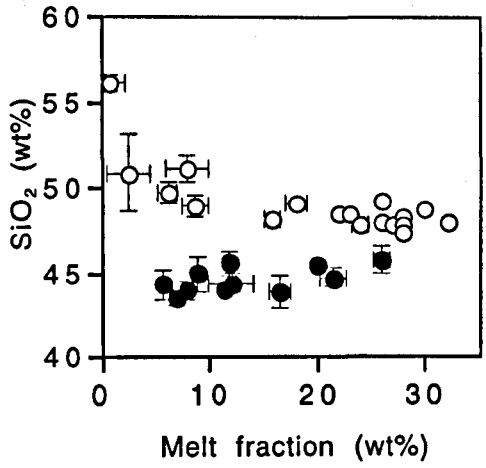

Figure 4.9 contd. Symbols as on previous page.

TiO_2 does not vary significantly in the liquid with pressure for F>8wt%. At F<8wt%, melt TiO_2 content at 1.5GPa dips approaching the solidus, due to the formation of amphibole which increases D^{TiO2} peridotite-melt. At 3GPa amphibole is not stable, and TiO_2 continues to increase with decreasing F, becoming progressively enriched relative to melts at 1.5GPa. Note that in two experiments at 1.5GPa, melt is anomalously TiO_2-poor (<0.75wt%) and are not included in the comparison with melts at 3GPa.

Al_2O_3 decreases in the liquid with increasing pressure, due to the increase in olivine component in the melt. The trend in Al_2O_3 content with melting is also changed. At 1.5GPa Al_2O_3 decreases slowly with F until cpx-out then decreases more rapidly due to dilution. At 3GPa, Al_2O_3 decreases much more rapidly with F until cpx-out, since the CaTs component in cpx decreases with pressure, and therefore less Al_2O_3 is contributed to the liquid during cpx melting. Al_2O_3 decreases more slowly above cpx-out at 3GPa than at 1.5GPa, since garnet melting continues to supply Al_2O_3 to the melt.

SiO_2 decreases in the liquid with increasing pressure, due to the increase in olivine component in the melt.

To summarise: Increase in the proportion of olivine entering the melt with pressure causes melt composition to increase in MgO and FeO*, and to decrease in SiO_2, CaO and Al_2O_3. Change from spinel to garnet at higher pressure decreases the CaTs component in cpx, so that Al_2O_3 is diluted more rapidly in the liquid during garnet lherzolite melting. At 1.5GPa, formation of amphibole at small F (<5wt%) causes depletion of the liquid in Na_2O and TiO_2, and enrichment in SiO_2 relative to anhydrous liquids. This is not observed at 3GPa as amphibole is not a stable phase. Figure 4.10 shows the effect of pressure on normative liquid composition. With increase in pressure from 1.5GPa to 3GPa, the melt is increased in olivine and decreased in Qz. Melt composition change from olivine- hypersthene (ol-

hy) normative to nepheline (Ne) normative. The Qz-normative melts formed at F<1wt% at 1.5GPa are not observed at 3GPa.

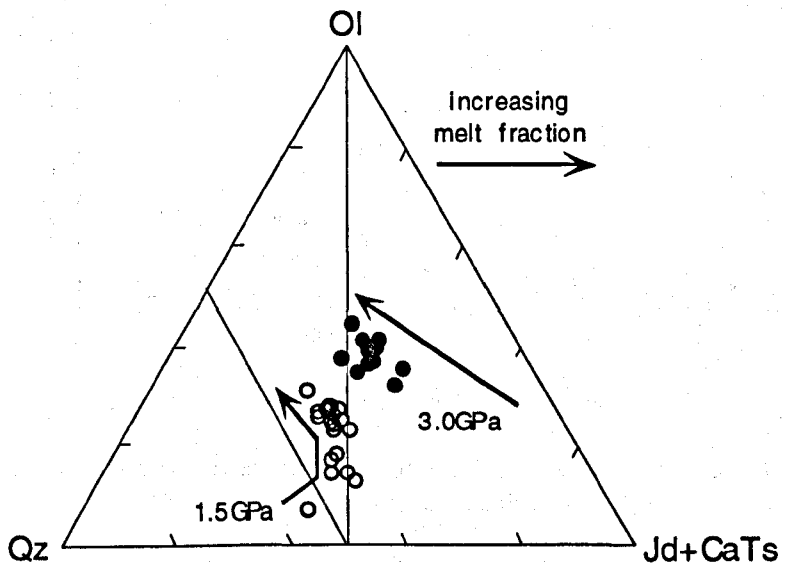

Figure 4.10 Projected liquid compositions for partial melting of hydrous peridotite at 1.5GPa and 3GPa, in the CIPW molecular normative tetrahedron. Projection from diopside (Di) onto the base olivine (Ol)-jadeite+calcium tschermakite (Jd+CaTs)-Quartz (Qz). Values for Fe^{3+}/FeO^* in hydrous liquids given in Tables 3.5 and 4.5. * All Fe as FeO. Filled circles = LeoP1 at 3GPa, open circles = Leo3 at 1.5GPa.

4.6 Melting reactions

The nature of the melting reaction in hydrous peridotite at 3GPa is illustrated by the variation in solid phase modal proportions with F (see Figure 4.11). Modes were calculated for each experiment by least squares mass balance of all phases to the bulk composition of LeoP1. The general melting reaction below cpx-out is:

olivine + cpx + garnet = opx + liquid

This is consistent with the melting reaction determined for anhydrous peridotite in the CMASN system by Walter & Presnall (1984). Since hydrous and anhydrous melt compositions are similar at 3GPa, the melting reactions for hydrous and anhydrous peridotite are likely to have a similar stoichiometries. Garnet in hydrous peridotite is likely to contribute a slightly smaller proportion to the melt, since it persists to larger melt fractions compared to garnet in anhydrous peridotite. Once cpx has been eliminated from

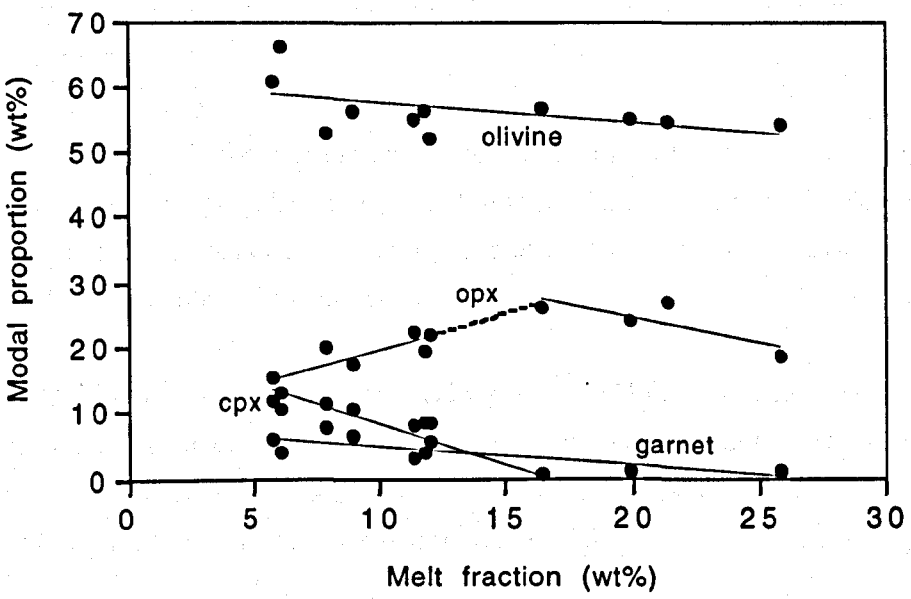

Figure 4.11 Variation in modal proportions of phases in LeoP1 with melt fraction at 3GPa.

the hydrous peridotite melting residue, the melting reaction changes to:

ol + opx + gt = liquid.

At 1.5GPa, the melting reaction in hydrous and anhydrous peridotite is:

opx + cpx + spinel = olivine + liquid

The lower temperature of melting in hydrous peridotite decreases the contribution of cpx to the melt relative to opx. Hydrous melts are depleted in MgO and CaO and enriched in Al_2O_3 relative to anhydrous melts at moderate melt fractions. The effect of increasing pressure is to increase the olivine contribution to the melt relative to pyroxene, and to decrease sensitivity of melt composition to temperature. Hydrous and anhydrous melts become increasingly similar with increasing pressure.

4.7 Conclusions

4.7.1 Effect of H_2O on peridotite melting

At 3GPa, the effect of adding H_2O to peridotite is:

1. At any given melt fraction, the temperature of melting is decreased. The scale of the down-temperature shift in F is greatest at the solidus and decreases with increased melt fraction. The rate of increase in F with increasing temperature is slower than that for

partial melting of anhydrous peridotite for F<15wt%, but is similar for melt fractions close to and above cpx-out.

2. Garnet is stabilised to higher melt fractions, due to the lower temperature of melting. At any given melt fraction, cpx in hydrous peridotite is Di-rich, En-poor and CaTs-poor relative to cpx in anhydrous peridotite. This is due to the lower temperature of melting in hydrous peridotite, and the stabilisation of garnet.

3. Melt composition is essentially unaffected by peridotite H_2O content, except that hydrous melts are slightly depleted in Al_2O_3 at moderate melt fractions due to garnet stabilisation. This is because the melting reaction in both hydrous and anhydrous peridotite is dominated by olivine contribution to the liquid.

4.7.2 Effect of pressure on hydrous peridotite melting

The effects on hydrous peridotite melting of increasing pressure from 1.5GPa to 3GPa are:

1. The general effect of H_2O on melting temperature does not change; temperature of melting is decreased and shows maximum depression near the solidus. Onset of melting is no longer controlled by amphibole stability and, for most hydrous peridotites, (H_2O >0.1wt%) melting starts at the H_2O-saturated solidus.

2. Opx becomes less abundant and slightly depleted in MgTs. Cpx is enriched in En and Jd components and depleted in CaTs component. Cpx is eliminated from the peridotite melting at a smaller melt fraction.

3. The melt composition is enriched in Mg and Fe, and depleted in SiO_2, CaO and Al_2O_3. Melt composition changes from ol-hy normative to Ne normative. Approaching the solidus at 1.5GPa, the melt reaction changes due to the formation of amphibole, and hydrous melts are SiO_2-rich and Al_2O_3- and Na_2O-poor relative to anhydrous melts. At 3GPa, there is no major hydrous phase is stable at near-solidus temperatures, and the melt reaction is approximately constant throughout the melting interval where cpx is present

4. Hydrous and anhydrous melt compositions converge. This is due to the increasing domination of olivine over pyroxene contribution to the melt and the absence of amphibole in hydrous peridotite at small melt fractions.

CHAPTER 5

Constraints on The Origin of Island Arc Magmas

5.1 Summary of results

Adding H_2O to peridotite has the following effects.

1. The temperature required to generate a given melt fraction is decreased. For a given peridotite H_2O content, the difference in temperature relative to anhydrous peridotite is diminished with increasing melt fraction. At 1.5GPa, onset and rate of melting at F<8wt% is controlled by amphibole stability. At F>8wt% the rate of melting is similar to that in anhydrous peridotite, and decrease in temperature relative to anhydrous conditions is directly proportional to peridotite H_2O content. At 3GPa, melting starts at the H_2O-saturated solidus (≈1000°C) for most hydrous peridotites (H_2O>0.1wt%). The rate of melting in hydrous peridotite at 3GPa is lower than that for partial melting of anhydrous peridotite for F<15wt%, but is similar for melt fractions close to and above cpx-out.

2. At 1.5GPa and F<5wt%, hydrous melts are Na_2O- and Al_2O_3-poor and SiO_2-rich relative to anhydrous melts, due to the presence of co-existing amphibole. At F=5-22wt%, hydrous melts are depleted in MgO and CaO, and enriched in Al_2O_3 relative to anhydrous melts, since cpx and ol are stabilised at the expense of opx in hydrous peridotite. At F>22wt%, hydrous and anhydrous melts are similar in composition. With increase in pressure to 3GPa, hydrous melt compositions become enriched in Mg and Fe, and depleted in SiO_2, CaO and Al_2O_3. Hydrous melt compositions become progressively closer to anhydrous melt compositions, due to the increasing domination of olivine over pyroxene contribution to the melt and instability of amphibole at pressures greater than ≈2.7GPa. At 3GPa, hydrous melts are slightly depleted in Al_2O_3 at F=10-20wt% due to garnet stabilisation in hydrous peridotite.

3. At 1.5GPa, cpx in hydrous peridotite is Di-rich and En-poor relative to cpx in anhydrous peridotite, due to lower temperature of melting. With increase in pressure, cpx is enriched in En and Jd components and opx becomes less abundant. At 3GPa, garnet is stabilised to higher melt fractions in hydrous peridotite than in anhydrous peridotite, due to lower temperature of melting. Opx is therefore depleted in the MgTs component and cpx in CaTs in hydrous peridotite.

4. Hydrous peridotite in subduction zones is believed to be under more oxidising conditions than other tectonic environments (Ballhaus, 1992; Wood *et al.*, 1990). The effect of increased fO_2 on partial melting of peridotite is to increase Fe^{3+} and FeO* in the melt, so that apparent $K_D^{Mg\text{-}Fe}$ olivine-melt is lower than the value predicted by Ulmer (1989) at 1.5GPa. Under more oxidising conditions, the spinel formed in peridotite is Fe^{3+}-bearing and therefore depleted in Al^{3+} relative to spinel in less oxidised peridotite.

5.2 Origin of island arc high MgO basalts

In island arcs a broad spectrum of magma compositions are erupted, which can be divided into 4 types in terms of their major element chemistry: high-MgO basalt (HMB, MgO>7wt%), high-Al_2O_3 basalt (HAB, Al_2O_3>17wt%, MgO<7wt% and SiO_2<54wt%), boninite (SiO_2>55% and MgO>7wt%) and evolved calc-alkaline compositions (*e.g.* andesite, dacite and rhyolite). Of these 4 types, only HMBs and boninites are considered to be primary magmas formed by partial melting of peridotite in the mantle wedge. Boninites are thought to form under very specific conditions (partial melting of depleted, harzburgitic mantle wedge fluxed by a slab-derived, LILE-bearing fluid at ≈1GPa (Crawford, 1989)), which are beyond the scope of this study.

It should be remembered that the range of primary magma compositions erupted at island arc is probably limited compared to the range of compositions generated in the mantle wedge. Some magmas may never reach the surface but evolve in composition during their ascent, either through re-equilibration with the surrounding mantle at shallower depth, or by subsequent differentiation/mixing processes in the crust. To identify compositional characteristics of the primary mantle melting signature, we must filter the erupted magma compositions to remove the effects of these crustal level processes.

Pressure, temperature and H_2O conditions in the source region of island arc magmas can be constrained by comparing primitive HMB compositions with those of experimentally-produced liquids. For this purpose, primitive HMB compositions were defined to be those with Mg*>68 (Green, 1967) and are all glass analyses.

5.2.1 Pressure

Figure 5.1 shows that the arc magmas have a similar range in composition to that of liquids generated by partial melting of hydrous peridotites KLB-1 and Leo3 at 1-1.5GPa (Hirose & Kawamoto, 1995; this study). This confirms that KLB-1 and Leo3 are close approximations to the peridotite bulk composition in the mantle wedge beneath island

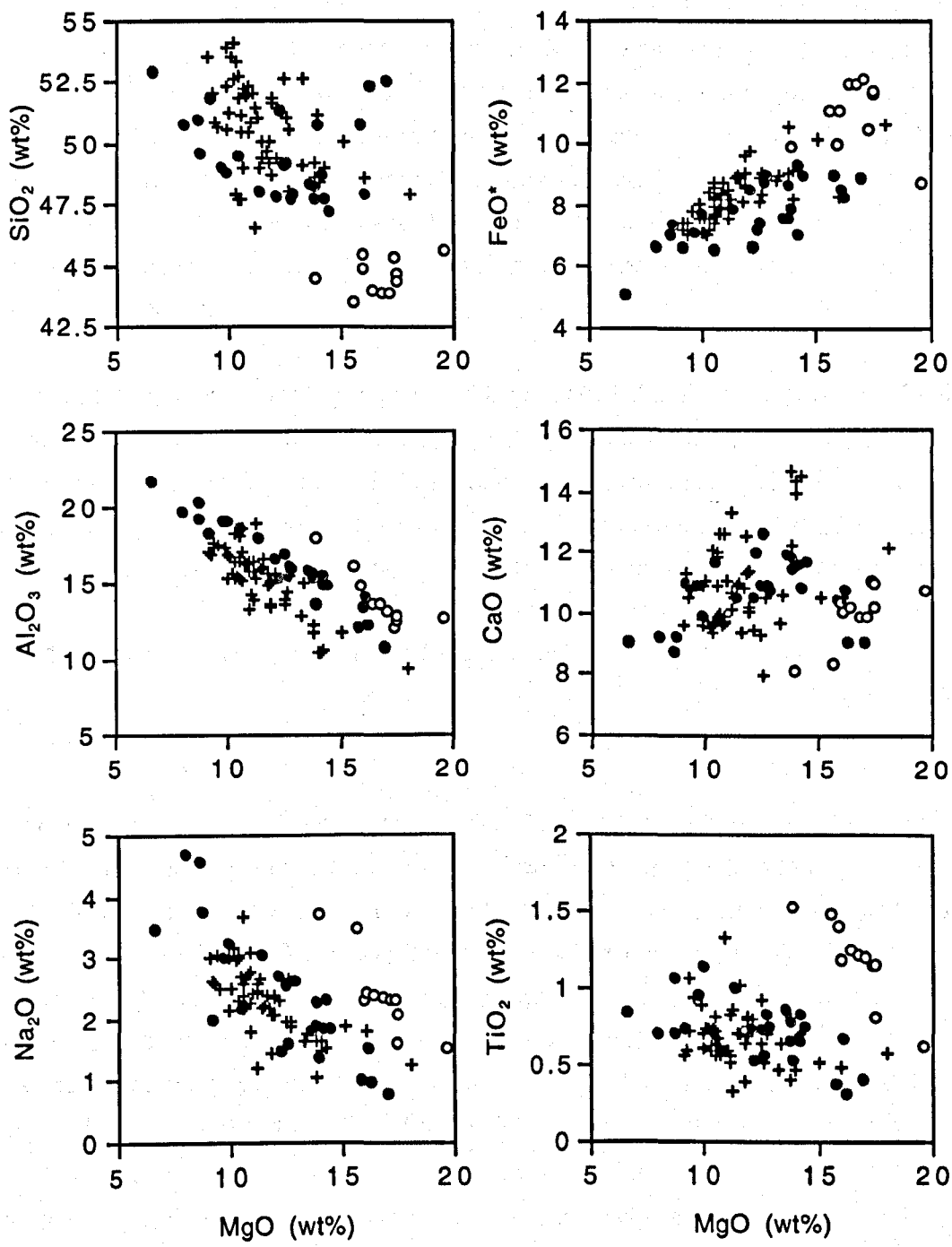

Figure 5.1 MgO variation diagrams showing oxide composition for primitive arc magmas and experimentally produced hydrous melts. Crosses = primitive arc magmas, grey-filled circles = melts of KLB1+0.2-0.5wt% H_2O at 1GPa (Hirose & Kawamoto, 1995), black-filled circles = melts of Leo3+0.4-0.8wt% H_2O at 1.5GPa, open circles = melts of LeoP1+0.5wt% H_2O at 3GPa (this study).

arcs. HMBs are likely to have equilibrated last with the mantle at 1-1.5GPa (30-45km depth) before segregation and ascent to the surface. Magma will segregate from the mantle where local conditions reach critical levels such that vertical ascent of magma starts to dominate over lateral transport of melt and crystals due to mantle wedge convection. The rheological behaviour of the lithosphere is believed to change from elastic to ductile at a depth of 30-50km (Davies & Stevenson, 1990, and references therein). It is probable that conditions favouring melt segregation are developed in association with this change in rheological behaviour.

In general, HMBs have lower MgO than liquids generated at 3GPa from peridotite LeoP1. Melting may be initiated in the mantle wedge at 2.7-3GPa (≈100km depth) due to amphibole breakdown (Tatsumi *et al.*, 1983) or compressional melting (Iwamori *et al.*, 1995), but it appears that these melts tend to re-equilibrate at shallower depth. Evidence of garnet-facies melting is therefore overprinted in terms of their major-element chemistry.

5.2.2 Melt Fraction, Temperature and Peridotite H_2O

Constraints from HMB composition

HMB compositions form a main cluster with MgO≤15wt%, with 2 more mafic samples. The melt fraction and temperature intervals required to generate the MgO range of the main HMB cluster can be estimated from peridotite partial melting experiments at 1 and 1.5GPa (see Figure 5.2 and Table 5.1). The melting interval required is F≈8-28wt% irrespective of peridotite H_2O content, but can be generated at progressively lower temperature with increasing peridotite H_2O content, *e.g.* at 1GPa, the maximum temperature required to generate the observed range in HMB compositions is 1280°C from a peridotite with 0.5wt% H_2O or 1380°C from an anhydrous peridotite.

Table 5.1 Mantle melting conditions required to generate observed range in primitive arc magma compositions

Pressure (GPa)	1[a]	1[a]	1[a]
H_2O (wt%)	0	0.1-0.3	0.4-0.6
Temperature (°C)	1280-1380	1180-1320	1100-1280
Melt fraction (wt%)	8-28	10-26	13-28
Melt H_2O (wt%)	0	0.4-3	1.4-4.6
Pressure (GPa)	1.5[b]	1.5[b]	1.5[b]
H_2O (wt%)	0	0.4-0.6	0.7-1
Temperature (°C)	1290-1340	1150-1300	1140-1300
Melt fraction (wt%)	6-25	8-28	8-30
Melt H_2O (wt%)	0	1.4-7.5	2.3-7.5

a Hirose & Kawamoto, 1995.
b This study.

Two HMB samples have MgO>15wt% and could have been formed at large melt fractions at 1-1.5GPa - this requires higher temperature (1350°C) or higher H_2O (>0.5wt% at 1GPa or >1wt% at 1.5GPa). Alternatively, higher MgO and FeO* suggest that these

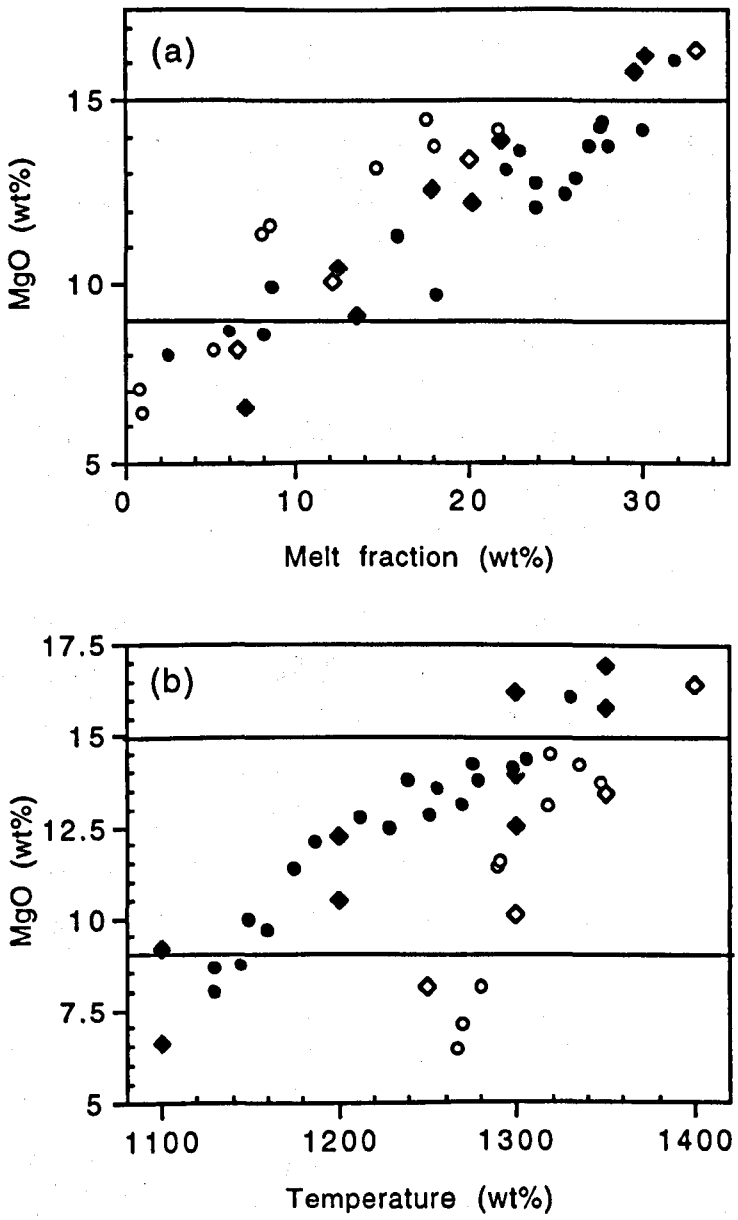

Figure 5.2 Variation in MgO with (a) melt fraction and (b) temperature in experimentally-produced liquids at 1-1.5GPa. Diamonds = partial melts of KLB-1 at 1GPa (Hirose & Kushiro, 1993; Hirose & Kawamoto, 1995), circles = partial melts of Leo3 and MPY at 1.5GPa (Robinson *et al.*, 1998; this study). Open = anhydrous peridotite, light grey = peridotite + 0.1-0.3wt% H_2O, dark grey = peridotite + 0.4-0.6wt% H_2O, black = peridotite + 0.7-1wt% H_2O.

samples might have formed at higher pressure, though their SiO_2, Al_2O_3, Na_2O and TiO_2 contents do not appear to be consistent with this. It is also possible that these samples do not represent primitive compositions, but have undergone crustal-level differentiation.

Constraints from kinematic/dynamic models

Petrological constraints suggest that the majority of HMBs are formed by 8-28wt% partial melting of the mantle wedge at 1-1.5GPa (30-45km). At this pressure, melting will start at the breakdown point of amphibole (the effective solidus, see section 3.3.1) which is ≈1100°C. Kinematic (*e.g.* Davies & Stevenson, 1992; Iwamori, 1997) and dynamic (*e.g.* Kincaid & Sacks, 1997) models have been used to predict the thermal structure of the mantle wedge. Results vary in detail according to the parameters used and assumptions made, but show that at a depth of 30-45km the maximum mantle temperature is 800°C and conditions are subsolidus. Melting in the source region of HMBs is thought to occur by local upwelling of hotter material from ≈90km depth in the mantle wedge, where partial melting is initiated by the pressure-dependent breakdown of amphibole. The hotter material may consist of buoyant diapirs of crystal/melt mush (Tatsumi *et al.*, 1993), or melt travelling by porous and/or channel flow (*e.g.* McKenzie, 1984; McKenzie, 1985; Iwamori, 1993). Models predict that the maximum temperature at 90km depth in the mantle wedge is 1200-1250°C (Davies & Stevenson, 1992; Iwamori, 1995; Kincaid & Sacks, 1997). Assuming an adiabatic gradient of 0.6°C/km (Davies & Stevenson, 1992), melt at 1250°C at 90km depth will have cooled to 1210-1220°C at 30-45km. Primitive HMB compositions, however, suggest that temperatures at 30-45km depth reach 1320°C, assuming a mantle H_2O content of 0.3wt% since it is consistent with primitive HMB H_2O contents. This discrepancy in temperature could have two explanations:

(i) Temperatures in the mantle wedge are ≈100°C higher than estimated by models. Iwamori (1997) suggested that additional heat might be supplied by radioactive decay of elements expelled from the downgoing slab into the overlying mantle by dehydration and decarbonation reactions, or by influx of hot plume material from the lower mantle. Davies & Stevenson (1992) observed that cyclic, short-term temperature increases could be produced in the mantle wedge due to flow reversal associated with wedge-slab decoupling.

(ii) Water content in the mantle is higher than that suggested by primitive HMB H_2O contents. Previous studies may have underestimated the degree of primary H_2O loss from HMB samples due to crystallization and differentiation during magmas ascent. Experimental results at 1GPa suggest that increasing peridotite H_2O content from 0.3 to 0.5wt% would decrease the temperature required to produce 22wt% melting from 1320°C to 1280°C. Assuming that temperature decrease is directly proportional to peridotite H_2O

content (see section 3.3.1), 22wt% melting could be produced at 1220°C and 1GPa from a peridotite with 0.8wt% H_2O.

Perhaps a more realistic scenario is a combination of these two possibilities. Steady-state temperature in the mantle wedge at ≈90km is 1250°C and steady-state mantle H_2O content is 0.3wt%. As hot material from 90km upwells to 30-45km, melting occurs in the source region of HMBs at 1100-1220°C and F≈8-20wt%. Periodic increases in mantle temperature and/or H_2O content allow larger melt fractions (F=20-28wt%) to be produced at 30-45km over short-term periods.

The experimental studies used to model HMB petrogenesis (Hirose & Kushiro, 1993; Hirose & Kawamoto, 1995; Robinson *et al.*, 1998; this study) simulate partial melting of peridotite as a batch melting process. Theoretical, experimental and geochemical studies (e.g. McKenzie, 1984; Johnson *et al.*, 1990; Iwamori, 1993) favour a near-fractional melting process at mid-ocean ridges. For an anhydrous peridotite, aggregates of incremental melts are similar in composition to batch melts but require a higher temperature (Hirose & Kushiro, 1998) since the melting residue becomes progressively more refractory as melt increments are removed. In subduction zones, however, fluids enriched in incompatible elements are released by dehydration and decarbonation reactions in the downgoing slab (Tatsumi, 1989) and periodically refertilise peridotite in the overlying the mantle wedge. Results of this study suggest that although melting may initiate at depth in the mantle wedge, primary arc magmas re-equilibrate at 30-45km before segregation from the mantle, and are therefore essentially batch melts. Mantle melting processes in subduction zones may be very complex, but it appears that primary arc magma compositions can be reproduced successfully by the relatively simple process of batch melting.

5.2.3 Re-evaluation of previous studies on the origin of island arc HMBs

Estimates of pressure-temperature conditions in the source region of arc magmas have been made by Baker *et al.* (1994) and Tatsumi *et al.* (1983). Baker *et al.* studied the compositions of hydrous primitive glasses from the Mt. Shasta region in California, which they termed HABs, but which are in fact high-Al_2O_3 HMBs. They compared the Mt Shasta HMB compositions to those of experimentally-produced anhydrous and hydrous liquids at 1.1-1.5GPa. One drawback to their experimental approach was that they determined temperatures and compositions of hydrous basalts saturated with harzburgite residue, but not with lherzolite residue. A second drawback was that they performed the hydrous basalt saturation experiments using graphite capsules. The experiments are likely to have produced CO_3^{2-}-bearing melts with variable H_2O contents (see section 2.3.2).

They conclude that the Mt Shasta HMBs were produced by melting of nearly anhydrous peridotite at 1350°C and 1.1GPa. Figure 5.2 shows Mt Shasta HMBs compared to more recent data on hydrous and anhydrous melt compositions generated from peridotite KLB-1 at 1GPa (Hirose & Kushiro, 1993; Hirose & Kawamoto, 1995). The data suggest that the Mt Shasta HMBs can be generated by ≈10-15wt% melting of peridotite with H_2O content ranging from anhydrous to 0.2wt%. The Mt Shasta HMBs have H_2O contents ranging from 0.5-1.1wt%, indicating a peridotite H_2O content of ≈0.1wt. Melting temperature decreases from 1300°C for anhydrous KLB-1 to 1200°C for KLB-1+0.2wt% H_2O. The Mt Shasta HABs are therefore likely to have been generated at ≈1250°C, 1GPa and F=10-15wt% from peridotite with 0.1wt% H_2O.

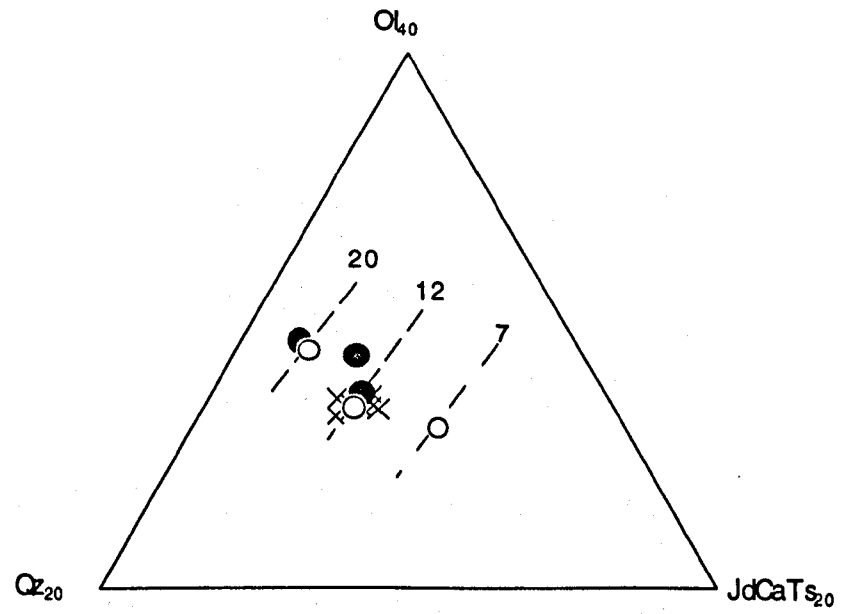

Figure 5.3 Projected normative compositions of Mt Shasta high-Al basalts (HABs) and partial melts of peridotite KLB-1 at 1GPa in the CIPW molecular normative tetrahedron. Data taken from Hirose & Kushiro (1993) and Hirose & Kawamoto (1995). Projection from diopside (Di) onto the base olivine (Ol)-jadeite+calcium tschermakite (Jd+CaTs)-Quartz (Qz). Crosses = HABs (Baker *et al.*, 1994), grey circles = melts of KLB-1+0.1-0.2wt% H_2O, open circles = melts of anhydrous KLB-1. Data are contoured for melt fraction.

Tatsumi *et al.* (1983) studied the petrogenesis of three basalts from the Northeastern Japan arc. They classified the three compositions as alkali olivine basalt (AOB), HAB and olivine tholeiite (OTB), although all 3 qualify as HMBs. They assumed 3wt% H_2O in the AOB, 1.5wt% H_2O in the "HAB" and 0.6-0.7wt% in the OTB, based on observed across-arc variations in magma H_2O and K_2O content. They performed hydrous and anhydrous multiple saturation experiments, and concluded that the 3 basalts were generated at 1320°C and 1.1GPa (OTB), 1.7GPA (HAB) and 2.3GPa (AOB). By

comparison with experimentally-produced melts (see Figure 5.4) it can be seen that all 3 basalts could be generated over a shallower pressure range of 1-1.5GPa. The OTB is estimated to have formed at 1300°C, 1GPa with ≈0.9wt% H_2O, which is consistent with Tatsumi *et al.*'s conclusions. The HAB could have formed at 1300°C, 1.5GPa with ≈1.6wt% H_2O (as predicted by Tatsumi *et al.*) or could have formed at 1300°C, 1GPa with ≈0.6wt% H_2O. The AOB is likely to have formed at 1.5GPa, at temperature ranging from 1200°C from peridotite+0.8wt% (AOB H_2O = 3.5wt%) to 1250°C from peridotite+0.5wt% (AOB H_2O = 2.5wt%). This suggests that Tatsumi *et al.* may have over-estimated the pressure and temperature required to generate the AOB under hydrous conditions.

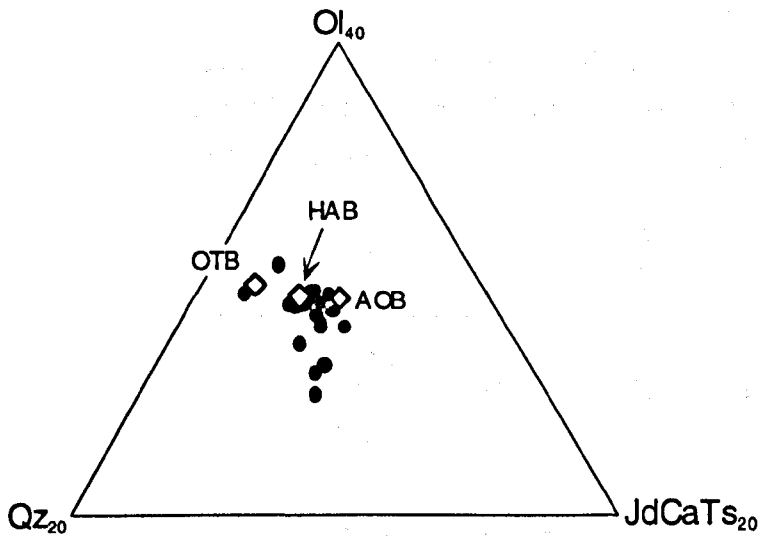

Figure 5.4 Projected normative compositions of basalts from the Northeastern Japan arc and partial melts of peridotite KLB-1 at 1GPa and peridotite Leo3 at 1.5GPa in the CIPW molecular normative tetrahedron. Data taken from Hirose & Kawamoto (1995) and this study. Projection from diopside (Di) onto the base olivine (Ol)-jadeite+calcium tschermakite (Jd+CaTs)-Quartz (Qz). Diamonds = arc basalts, where AOB = alkali olivine basalt, HAB = high alumina basalt, OTB = olivine tholieiite basalt (Tatsumi *et al.*, 1983). Grey circles = melts of KLB-1+0.1-0.2wt% H_2O, filled circles = melts of Leo3+0.4-1wt% H_2O.

Stolper & Newman (1994) used the chemistry of the Mariana Trough basalts to estimate the effect of water on mantle melting. They assumed that the basalts had undergone olivine-only fractionation, and estimated the composition of the parental liquids by incremental addition of olivine. They observed that the trace element compositions of the estimated parental liquids formed a trend between NMORB composition and the Mariana arc magma compositions. They suggest that the parental liquids of the Trough basalts can be formed by melting mixtures of NMORB source mantle and a hydrous component enriched in incompatible trace elements including Na_2O and K_2O. Liquids representing

higher degrees of melting would be formed from mixtures with a greater proportion of the hydrous component. Trends in the major element composition of the estimated parental liquids, however, are not consistent with the results of experimental studies of hydrous peridotite melting at 1-3GPa (Hirose & Kawamoto, 1995; this study). In the estimated parental liquids, MgO and FeO* decrease and Al_2O_3 increases with increasing H_2O and melt fraction. Results of experimental studies show the reverse is true, i.e. MgO and FeO* increase and Al_2O_3 decreases with increasing melt fraction, at 1, 1.5 and 3GPa. Stolper & Newman suggest that decrease in MgO and FeO* with increasing H_2O and F is due to a progressive expansion in the olivine liquidus volume with increasing H_2O content. They acknowledge, however, that the effect of increasing H_2O is in competition with the effect of increasing F, which increases normative olivine in the melt for a peridotite of constant composition. Figure 5.5 shows the range in TiO_2 and MgO observed in the Mariana Trough parental liquids. At pressures of 1.5GPa and higher, the increase in H_2O and F required to produce the same range in TiO_2 will result in an increase in MgO in the melt. At lower pressures, the effect of H_2O may become more significant, but the available data are not conclusive.

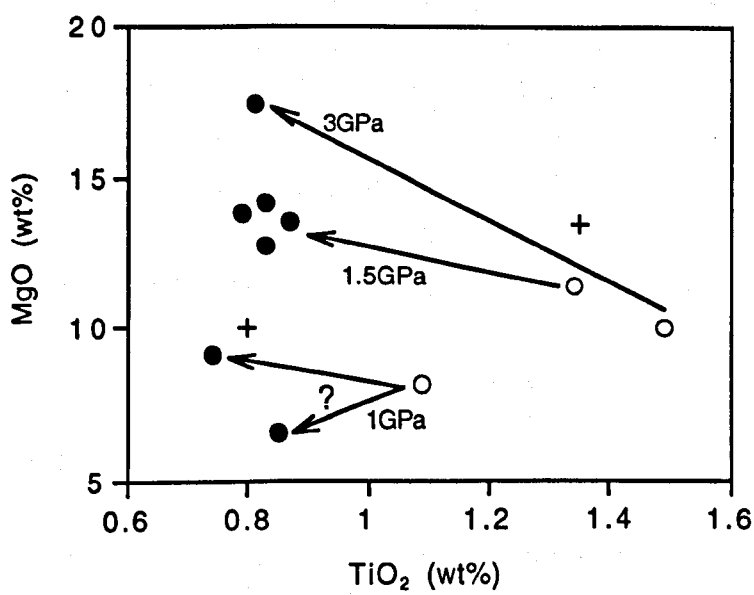

Figure 5.5 Change in MgO and TiO_2 with increase in H_2O in Mariana Trough parental liquids, and experimentally-produced liquids at 1-3GPa. Crosses = Mariana Trough parental liquids (Stolper & Newman, 1994), open circles = anhydrous melts, black circles = hydrous melts.

Alternative explanations for the apparent inconsistency in the major composition of the Mariana Trough parental liquids might be:

(i) The Mariana Trough parental liquids have undergone some process (e.g. poly-phase fractionation, disequilibrium reaction) subsequent to segregation from the mantle that has overprinted the effects of hydrous melting in terms of their major element composition, but has not affected their trace element composition.

(ii) There is a problem in Stolper & Newman's method of estimating parental liquid composition, *e.g.* their assumption of olivine-only fractionation, and that all parental liquids are in equilibrium with Fo_{90}. Liquids at high melt fraction (F>15wt%) or under relatively oxidising conditions (fO_2>QFM+1) may be in equilibrium with more refractory olivine (*e.g.* Robinson *et al.*, 1998; this study).

5.3 Origin of Mid-Ocean Ridge Basalts (MORB)

Trace element and isotopic ratios in mid-ocean ridge basalts (MORB) indicate that melting initiates within the garnet facies (*e.g.* Salters & Hart, 1989; Johnson *et al.*, 1990), but at the temperatures required to initiate melting under dry conditions, prohibitively high melt fractions would be generated. It has been recently suggested (Hirth & Kohlstedt, 1998) that the presence of H_2O in the MORB source region could initiate melting at much lower temperature and provide a mechanism for producing the MORB garnet signature without extreme degrees of melting. Results of this study suggest that hydrous melting is likely to start at the H_2O-saturated solidus temperature of ≈1000°C. Hydrous melt compositions are very close to those of anhydrous melts at 3GPa for F>5wt%, and are expected to be similar at F<5wt% for most hydrous peridotites (H_2O>0.1wt%) since no major hydrous solid phase is present at the solidus.

5.4 Directions for the Future

The results described in this thesis, in combination with other experimental and observational data, help place more stringent quantitative constraints on the conditions of magma genesis from hydrous peridotite. However, a number of significant questions remain, and future studies need to address at least the following points:

1. Elaboration of the discrepancy between mantle wedge temperatures predicted from models and those from experimental studies of primary arc magma petrogenesis. Further refinement of models is needed to study possible sources and effects of short-term variations in heat flow and/or H_2O content in the mantle wedge. Detailed experimental

studies are needed to quantify more precisely the effect of peridotite H_2O on melt composition for H_2O contents of 0.1-0.8wt% at 1-1.5GPa.

2. Modelling of melting path of liquid during ascent from depth in the mantle wedge to the source region of primary arc magmas. Melting is believed to be initiated in the mantle wedge at ≈2.7-2.9GPa due to pressure-sensitive breakdown of amphibole in the garnet field (Tatsumi *et al.*, 1983). Current work has quantified the effect of H_2O on peridotite melting at 30-45km and ≈100km, but experimental studies are needed on hydrous peridotite melting at intermediate depths of 50-80km, *i.e.* 2-2.7GPa.

3. Exploration of the role of small degree, high pressure, hydrous melts in MORB genesis. Data on melt compositions and temperatures at F<3wt% are needed for hydrous melting of peridotite in the garnet field of stability.

LIST OF REFERENCES

Anderson D.K. 1989 Theory of the Earth, 366 p., Blackwell, Oxford.

Anderson D.L. 1982 The chemical composition and evolution of the mantle: advances in Earth and planetary sciences. *In* Akimoto S. & Manghnani M.H. (eds), High-pressure research in geophysics. Reidel, 301-318.

Anderson D.L. 1979 The upper mantle transition region: eclogite? *Geophysical. Research Letters*, 6: 433-436.

Baker M.B., Grove T.L. & Price R. 1994 Primitive basalts and andesites from the Mt Shasta region, N. California: Products of varying melt fraction and H_2O content. *Contributions to Mineral.ogy and Petrology*, 118: 111-129.

Baker M.B., Hirschmann M.M., Ghiorso M.S. & Stolper E. 1995 Compositions of near-solidus peridotite melts from experiments and thermodynamic calculations. *Nature*, 375: 308-311.

Baker M.B., Newman S., Beckett J.R. & Stolper E. 1992 Separating liquid from crystals in high-pressure melting experiments using diamond aggregates. *Geological. Society of America Abstracts with Program*, 24: A256.

Baker M.B. & Stolper E. 1994 Determining the composition of high-pressure mantle melts using diamond aggregates. *Geochimica et Cosmochimica Acta*, 58: 2811-2827.

Ballhaus C. 1992 Redox States of Lithospheric and asthenospheric upper mantle. *Contributions to Mineral.ogy and Petrology*, 114: 331-348.

Bell D.R. & Rossman G.R. 1992 Water in the mantle: the role of nominally anhydrous minerals. *Science*, 255: 1391-1397.

Blundy J.D., Falloon T.J., Wood B.J. & Dalton J.A. 1995 Sodium partitioning between clinopyroxene and silicate melts. *Journal. of Geophysical. Research*, 100: 15501-15515.

Bowen N.L. 1928 The evolution of the igneous rocks, 332 p., Princeton University Press, Princeton, New Jersey.

Boyd F.R. & England J.L. 1960 Apparatus for phase equilibrium measurements at pressures up to 50 kilobars and temperatures up to 1750°C. *Journal. of Geophysical. Research*, 65: 741-748.

Coleman R.G. 1977 Ophiolites, 229 p., Springer-Verlag, Berlin.

Crawford A.E. 1989 Boninites, Unwin Hyman, London.

Daly R.A. 1933 Igneous rocks and the depth of the Earth, 598 p., McGraw-Hill, New York.

Davies J.H. & Stevenson D.J. 1992 Physical model of source region of subduction zone volcanics. *Journal. of Geophysical. Research*, 97: 2037-2070.

Dawson J.B. 1980 Kimberlites and their Xenoliths, 252 p., Springer-Verlag, Berlin.

Dickenson M.P. & Hess P.C. 1986 The structural role and homogeneous equilibria of iron in peraluminous, metalaluminous and peralkaline silicate melts. *Contributions to Mineral.ogy and Petrology*, 92: 207-217.

Dixon J.E., Stolper E. & Delaney J.R. 1988 Infrared spectroscopic measurements of CO_2 and H_2O in Juan de Fuca basaltic glasses. *Earth and Planetary Science Letters*, 90: 87-104.

Dixon J.E., Stolper E. & Holloway J.R. 1995 An experimental study of water and carbon dioxide solubilities in mid-ocean ridge basaltic liquids I: Calibration and solubility models. *Journal. of Petrology*, 36: 1607-1631.

Dobson P.F., Skogby H. & Rossman G.R. 1995 Water in boninite glass and coexisitng orthopyroxene: concentration and partitioning. *Contributions to Mineral.ogy and Petrology*, 118: 414-419.

Falloon T.J. & Green D.H. 1987 Anhydrous partial meling of MORB pyrolite and other peridotite compositions at 10kb: Omplications for the origin of primitive MORB glasses. *Contributions to Mineral.ogy and Petrology*, 37: 181-219.

Falloon T.J., Green D.H., Hatton C.J. & Harris K.L. 1988 Anhydrous partial melting of a fertile and depleted peridotite from 2-30kb and application to basalt petrogenesis. *Journal. of Petrology*, 29: 1257-1282.

Falloon T.J., Green D.H., O'Neill H.S. & Ballhaus C.G. 1996 Quest for low-degree partial melts. *Nature*, 381: 285.

Frey F.A. & Prinz M. 1978 Ultramafic inclusions from San Carlos, Arizona - Petrologic and geochemical data bearing on their petrogenesis. *Earth and Planetary Science Letters*, 38: 129-179.

Fujii T. & Scarfe C.M. 1985 Composition of liquids coexising with spinel lherzolite at 10kbar and the genesis of MORBs. *Contributions to Mineral.ogy and Petrology*, 90: 18-28.

Gaetani G.A. & Grove T.L. 1998 The influence of water on mantle melting. *Contributions to Mineral.ogy and Petrology*, 131: 323-345.

Gasparik T. 1993 The role of volatiles in the transition zone. *Journal. of Geophysical. Research*, 98: 4287-4299.

Gasparik T. 1992 Enstatite-Jadeite join and its role in the Earth's mantle. *Contributions to Mineral.ogy and Petrology*, 111: 283-298.

Gass I.G., Lippard S.J. & Shelton A.W. 1984 Ophiolites and oceanic lithosphere, 431 p., Blackwell Scientific, Oxford.

Gill J.B. 1981 Orogenic andesites and plate tectonics, 358 p., Springer-Verlag, Berlin.

Grashoff G.J., Pilkington C.E. & Conti C.W. 1983 The purification of hydrogen. *Platinum Metal.s Review*, 27: 157-169.

Green D.H. 1973 Experimental melting studies on a model upper mantle composition at high pressure under water-saturated and water-undersaturated conditions. *Earth and Planetary Science Letters*, 19: 37-53.

Green D.H. 1976 Experimental testing of "equilibrium" partial melting of peridotite under water-saturated, high-pressure conditions. *Canadian Mineral.ogist*, 14: 255-268.

Green D.H. & Ringwood A.E. 1967 The genesis of basaltic magmas. *Contributions to Mineral.ogy and Petrology*, 15: 103-190.

Green D.H. & Ringwood A.E. 1964 Fractionation of basaltic magmas at high pressures. *Nature*, 201: 1276.

Grove T.L. 1981 Use of FePt alloys to eliminate the iron loss problem in 1atm gas mixing experiments: Theoretical and practical considerations. *Contributions to Mineral.ogy and Petrology*, 78: 298-304.

Gudfinnsson G.H. & Presnall D.C. 1996 Melting relations of model lherzolite in the system CaO-MgO-Al_2O_3-SiO_2 at 2.4-3.4GPa and the generation of komatiites. *Journal. of Geophysical. Research*, 101: 27701-27709.

Gurney J.J. & Harte B. 1980 Chemical variations in upper mantle nodules from South African kimberlites. *Philosophical. Transactions of the Royal. Society of London*, A297: 273-293.

Helz R.T. 1982 Phase relations and compositions of amphiboles produced in studies of the melting behaviour of rocks. *In* Veblen D.R. & Ribbe P.H. (eds), Amphiboles: Petrology and experimental phase relations. Mineralogical Society of America, 9B: 279-346.

Hirose K. 1997 Melting experiments on lherzolite KLB-1 under hydrous conditions and generation of high-magnesian andesitic melts. *Geology*, 25: 42-44.

Hirose K. & Kawamoto T. 1995 Hydrous partial melting of lherzolite at 1GPa: The effect of H_2O on the genesis of basaltic magmas. *Earth and Planetary Science Letters*, 133: 463-473.

Hirose K. & Kawamura K. 1994 A new experimental approach for incremental batch melting of peridotite at 1.5GPa. *Geophysical. Research Letters*, 21: 2139-2142.

Hirose K. & Kushiro I. 1998 The effect of melt segregation on polybaric mantle melting: Estimation from the incremental melting experiments. *Earth and Planetary Science Letters*, 107: 111-118.

Hirose K. & Kushiro I. 1993 Partial melting of dry peridotites at high pressures: Determination of compositions using aggregates of diamond. *Earth and Planetary Science Letters*, 114: 477-489.

Hirschmann M.M., Baker M.B. & Stolper E. 1998 The effect of alkalis on the silica content of mantle-derived melts. *Geochimica et Cosmochimica Acta*, 62: 883-902.

Hirth G. & Kohlstedt D.L. 1996 Water in the oceanic upper mantle: Implications for rheology, melt extraction and the evolution of the lithosphere. *Earth and Planetary Science Letters*, 144: 93-108.

Holloway J.R. 1981 Volatile interaction in magmas. *In* Newton R.C., Navrotsky A. & Wood B.J. (eds), Thermodynamics of Minerals and melts. Springer-Verlag,

Holloway J.R., Pan V. & Gudmundsson G. 1992 High pressure fluid-absent melting experiments in the presence of graphite: Oxygen fugacity, ferric/ferrous ratio and dissolved CO_2. *European Journal. of Mineral.ogy*, 4: 105-114.

Hoover J.D. & Presnall D.C. 1982 Melting relations of simplified peridotite in the SiO_2-CaO-Al_2O_3-MgO-Na_2O (SCAMN) system from 1atm. to 20kb II: Results and application to basalt generation. *Geological. Society of America Abstracts with Progr*, 14: 517.

Ito K. & Kennedy G.C. 1967 Melting and phase relations in a natural peridotite up to 40kb. *American Journal. of Science*, 265: 519-538.

Iwamori H. 1993 A model for disequilibrium mantle melting incorporating melt transport by porous and channel flows. *Nature*, 366: 734-737.

Iwamori H. 1997 Heat sources and melting in subduction zones. *Journal. of Geophysical. Research,* 102: 14803-14820.

Iwamori H., McKenzie D. & Takahashi E. 1995 Melt generation by isentropic mantle upwelling. *Earth and Planetary Science Letters,* 134: 253-266.

Jaques A.L. & Green D.H. 1980 Anhydrous melting of peridotite at 0-15kb pressure and the genesis of tholeiitic basalts. *Contributions to Mineral.ogy and Petrology,* 73: 287-310.

Jaques A.L. & Green D.H. 1979 Determination of liquid compositions in high-pressure melting of peridotite. *American Mineral.ogist,* 64: 1312-1321.

Johannes W., Bell P.M., Boettcher A.L., Chipman D.W., Hays J.F., Mao H.K., Newton R.C. & Seifert F. 1971 An interlaboratory comparison of piston cylinder calibration using the albite breakdown. *Contributions to Mineral.ogy and Petrology,* 32: 24-38.

Johnson K.T.M., Dick H.J.B. & Shimizu N. 1990 Melting in the oceanic upper mantle: An ion microprobe study of diopsides in abyssal peridotites. *Journal. of Geophysical. Research,* 95: 2661-2678.

Johnson K.T.M. & Kushiro I. 1992 Segregation of high-pressure partial melts from peridotite using aggregates of diamond: A new experimental approach. *Geophysical. Research Letters,* 19: 1703-1706.

Juster T.C., Grove T.L. & Perfit M.R. 1989 Experimental constraints on the generation of FeTi basalts, andesites and rhyodacites at the Galapagos spreading centre, 85°W and 95°W. *Journal. of Geophysical. Research,* 94: 9251-9274.

Kawamoto T. 1996 Experimental constraints on differentiation and H_2O abundance of calc-alkaline magmas. *Earth and Planetary Science Letters,* 144: 577-589.

Kawamoto T. & Hirose K. 1994 Au-Pd sample containers for melting experiments on iron and water bearing systems. *European Journal. of Mineral.ogy,* 6: 381-385.

Kennedy W.Q. & Anderson E.M. 1938 Crustal layers and the origin of the magmas. *Bulletin of Volcanology,* 2-3: 23-82.

Kincaid C. & Sacks I.S. 1997 Thermal and dynamical evolution of the upper mantle in subduction zones. *Journal. of Geophysical. Research,* 102: 12295-12315.

Kinzler R.J. & Grove T.L. 1992b Primary magmas of mid-ocean ridge basalts 2. Applications. *Journal. of Geophysical. Research,* 97: 6907-6926.

Kinzler R.J. & Grove T.L. 1993 Corrections and further discussion of the primary magmas of mid-ocean ridge basalts, 1 and 2. *Journal. of Geophysical. Research,* 98: 22339-22347.

Kinzler R.J. & Grove T.L. 1992a Primary magmas of mid-ocean ridge basalts 1. Experiments and methods. *Journal. of Geophysical. Research,* 97: 6885-6906.

Klein E.M. & Langmuir C.H. 1987 Global correlations of ocean ridge basalt chemistry with axial depth and crustal thickness. *Journal. of Geophysical. Research,* 92:

Kohn S.C. 1996 Solubility of H_2O in nominally anhydrous minerals using ^1H MAS NMR. *American Mineral.ogist,* 81: 1523-1526.

Kress V.C. & Carmichael I.S.E. 1991 The compressibility of silicate liquids containing Fe_2O_3 and the effect of composition, temperature, oxygen fugacity and pressure on their redox states. *Contributions to Mineral.ogy and Petrology,* 108: 82-92.

Kress V.V. & Carmichael I.S.E. 1991 The compressibility of silicate liquids containing Fe_2O_3 and the effect of composition, temperature, oxygen fugacity and pressure on their redox states.

Kuno H. 1960 High-alumina basalt. *Journal. of Petrology,* 1: 121-145.

Kushiro I. 1968 Compositions of magmas formed by melting of the Earth's upper mantle. *Journal. of Geophysical. Research,* 73: 619-634.

Kushiro I. 1996 Partial melting of a fertile mantle peridotite at high pressures: An experimental study using aggregates of diamond. *In* Basu A.S. & Hart S. (eds), Earth Processes: Reading the Isotopic Code. American Geophysical Union, Geophysical Monograph, 109-122.

Kushiro I. 1990 Partial melting of mantle wedge and evolution of island arc crust. *Journal. of Geophysical. Research,* 95: 15929-15939.

Kushiro I. 1972 Effect of water on the compositions of magmas formed at high pressures. *Journal. of Petrology,* 13: 311-334.

Kushiro I. 1970 Stability of amphibole and phlogopite in the upper mantle. *Carnegie Institute of Washington Yearbook,* 68: 245-247.

Kushiro I., Shimizu N., Nakamura Y. & Akimoto S. 1972 Compositions of coexisting liquid and solid phases formed upon melting of natural garnet and spinel lherzolites at high pressures: A preliminary report. *Earth and Planetary Science Letters,* 14: 19-25.

Kushiro I. & Yoder H.S.J. 1974 Formation of eclogite from garnet lherzolite liquidus relations in a portion of the system $MgSiO_3$-CaSi O_3-Al_2O_3. *Carnegie Institute of Washington Yearbook,* 73: 266-269.

Kushiro I., Yoder H.S.J. & Nishikawa M. 1968 Effect of water on melting of enstatite. *Geological. Society of America Bulletin,* 79: 1685-1692.

Luth R.W., Virgo D., Boyd F.R. & Wood B.J. 1990 Ferric iron in mantle-derived garnets: implications for thermobarometry and for the oxidation state of the mantle. *Contributions to Mineral.ogy and Petrology,* 104: 56-72.

McKenzie D. 1984 The generation and compaction of partially molten rock. *Journal. of Petrology,* 25: 713-765.

McKenzie D. 1985 The extraction of magma from the crust and mantle. *Earth and Planetary Science Letters,* 74: 81-91.

McKenzie D. & Bickle M.J. 1988 The volume and composition of melt generated by extension of the lithosphere. *Journal. of Petrology,* 29:

Menzies M.A. 1983 Mantle ultramafic xenoliths in alkaline magmas: evidence for mantle heterogencity modified by magmatic activity. *In* Hawkesworth C.J. & Norry M.J. (eds), Continental basalts and mantle xenoliths. Shiva, 92-110.

Michael P.J. 1988 The concentration, behaviour and storage of H_2O in the suboceanic upper mantle: implications for mantle metasomatism. *Geochimica et Cosmochimica Acta,* 52: 555-566.

Michael P.J. & Bonatti E. 1985 Peridotite composition from the North Atlantic: Regional and tectonic variations and implications for partial melting. *Earth and Planetary Science Letters,* 73: 91-104.

Milhollen G.L., Irving A.J. & Wyllie P.J. 1974 Melting interval of peridotite with 5.7 per cent water to 30 kilobars. *Journal. of Geology,* 82: 575-587.

Mitchell R.H. 1986 Kimberlites: Mineralogy, Geochemistry, Petrology, p., Plenum, New York.

Mysen B.O. & Boettcher A.L. 1973 Phase relations in peridotite H_2O-CO_2 systems with controlled H_2O and fO_2. *American Geophysical. Union Transactions Abstract,* 54: 480.

Mysen B.O. & Boettcher A.L. 1975a Melting of a hydrous mantle I: Phase relations of natural peridotite at high pressures and temperatures with controlled activities of water, carbon dioxide and hydrogen. *Journal. of Petrology,* 16: 520-548.

Mysen B.O. & Boettcher A.L. 1975b Melting of a hydrous mantle II: Geochemistry of crystals and liquids formed by anatexis of mantle peridotite at high pressures and temperatures as function of controlled activities of water, hydrogen and carbon dioxide. *Journal. of Petrology,* 16: 549-593.

Mysen B.O. & Boettcher A.L. 1972 Melting of a hydrous mantle: Phase relations in peridotite H_2O-CO_2 systems. *Geological. Society of America Abstracts with Programs,* 4: 608.

Mysen B.O. & Kushiro I. 1977 Compositional variations of coexisting phases with degree of melting of peridotite in the upper mantle. *American Mineral.ogist,* 62: 843-865.

Navon O., Hutcheon I.D., Rossman G.R. & Wasserburg G.J. 1988 Mantle-derived fluids in diamond micro-inclusions. *Nature,* 335: 784-789.

Nell J. & Wood B.J. 1989 Thermodynamic properties in a multicomponent solid solution involving cation disorder: Fe_3O_4-MgF e_2O_4-$FeAl_3O_4$-Mg Al_3O_4 spinels. *American Mineral.ogist,* 74: 1000-1015.

Nicholls I.A. & Green D.H. 1973 Effect of water on olivine stability on tholeiites and the production of silica-saturated magmas in the island-arc environment. *Journal. of Geology,* 8: 285-300.

Niida K. & Green D.H. 1999 Stability and chemical composition of pargasitic amphibole in MORB pyrolite under upper mantle conditions. *Contributions to Mineral.ogy and Petrology,* 135: 18-40.

Niu Y. & Batiza R. 1991 An empirical method for calculating melt compositions produced beneath mid-ocean ridges: Application for axis and off-axis (seamounts) melting. *Journal. of Geophysical. Research,* 21: 21753-21777.

Nixon P.H. 1987 Mantle Xenoliths, 844 p., Wiley, Chichester.

O'Hara M.J. 1965 Primary magmas and the origin of basalts. *Scottish Journal. of Geology,* 1: 19-40.

O'Neill H.S. 1987 Quartz-fayalite-iron and quartz-fayalite-magnetite equilibria and the free energy of formation of fayalite (Fe_2SiO_4) and magnetite (Fe_3O_4). *American Mineral.ogist,* 72: 67-75.

Olafsson M. & Eggler D.H. 1983 Phase relations of amphibole, amphibole-carbonate and phlogopite-carbonate peridotite: petrolgic constraints on the asthenosphere. *Earth and Planetary Science Letters,* 64: 305-315.

Osborn E.F. & Tait D.B. 1952 The system diopside-forsterite-anorthite. *American Journal. of Science,* Bowen Vol.: 413-433.

Patino Douce A.E. & Beard J.S. 1994 H_2O loss from hydrous melts during fluid-absent piston cylinder experiments. *American Mineral.ogist,* 79: 585-588.

Peacock S.M. 1990 Fluid processes in subduction zones. *Science,* 248: 329-337.

Perfit M.R., Gust D.A., Bence A.E., Arculus R.J. & Taylor S.R. 1980 Chemical characteristics of island arc basalts: implications for mantle sources. *Chemical. Geology,* 30: 227-256.

Poldevaart A. 1955 Chemistry of the Earth's crust. *Geological. Society of America Special. Paper,* 2: 119-144.

Presnall D.C., Dixon S.A., Dixon J.R., O'Donnell T.H., Brenner N.L., Schrock R.L. & Dycus D.W. 1978 Liquidus phase relations on the join diopside-forsterite-anorthite from 1atm. to 20kbar: their bearing on the generation and crystallization of basaltic magma. *Contributions to Mineral.ogy and Petrology,* 66: 203-220.

Ringwood A.E. 1975 Composition and petrology of the Earth's mantle, 618 p., McGraw-Hill, New York.

Ringwood A.E. 1962b A model for the upper mantle. *Journal. of Geophysical. Research,* 67: 4473-4477.

Ringwood A.E. 1982 Phase transformations and differentation in subducted lithosphere: Implications for mantle dynamics, basalt petrogenesis and crustal evolution. *Journal. of Geology,* 90: 611-643.

Ringwood A.E. 1962a A model for the upper mantle. *Journal. of Geophysical. Research,* 67: 857-867.

Robinson J.A.C., 1997. Partial melting of anhydrous peridotite at 1.5 and 3GPa. Ph.D. thesis, Faculty of Science, University of Bristol

Robinson J.A.C., Wood B.J. & Blundy J.D. 1998 The beginning of melting of fertile and depleted peridotite at 1.5GPa. *Earth and Planetary Science Letters,* 155: 97-111.

Salters V.J.M. & Hart S. 1989 The hafnium paradox and the role of garnet in the source of mid-ocean ridge basalts. *Nature,* 342: 420-422.

Schmidt M.W. & Poli S. 1998 Experimentally-based water budgets for dehydrating slabs and consequences for arc magma generation. *Earth and Planetary Science Letters,* 163: 361-379.

Schrauder M. & Navon O. 1994 Hydrous carbonatitic fluids in fibrous diamonds from Jwaneng, Botswana. *Geochimica Cosmochimica Acta,* 58: 761-771.

Sen C. & Dunn T. 1994 Dehydration melting pf a basaltic composition amphibolite at 1.5 and 2.0GPa - implications for the origin of adakites. *Contributions to Mineral.ogy and Petrology,* 117: 394-409.

Sisson T.W., Hankins W.B. & Presnall D.C. 1997 Melting of amphibole lherzolite investigated in the system CMASN-H_2O. *American Geophysical. Union EOS Transactions Abstract,* 78: F835.

Sobolev A.J. & Chaussidon M. 1996 H_2O concentrations in primary melts from supra-subduction zones and mid-ocean ridges: implications for H_2O storage and recycling in the mantle. *Earth and Planetary Science Letters,* 137: 45-55.

Sobolev N.V. 1977 Deep-seated inclusions in kimberlites and the problem of the composition of the upper mantle, 279 p., American Geophysical Union,
Washington D.C.

Stern C.R. & Wyllie P.J. 1975 Effect of iron absorption by noble metal capsules on phase boundaries in rock-melting experiments at 30kb. *American Mineral.ogist,* 60: 681-689.

Stolper E. 1980 A phase diagram for mid-ocean ridge basalts: preliminary results and implications for petrogenesis. *Contributions to Mineral.ogy and Petrology,* 74: 13-27.

Stolper E. & Newman S. 1994 The role of water in the petrogenesis of Mariana trough magmas. *Earth and Planetary Science Letters,* 121: 293-325.

Takahashi E. 1986 Melting of dry peridotite KLB-1 up to 14GPa: Implications on the origin of peridotitic upper mantle. *Journal. of Geophysical. Research,* 91: 9367-9382.

Takahashi E. & Kushiro I. 1983 Melting of a dry peridotite at high pressures and basalt magma genesis. *American Mineral.ogist,* 68: 859-879.

Tatsumi Y. 1989 Migration of fluid phases and genesis of basalt magmas in subduction zones. *Journal. of Geophysical. Research,* 94: 4697-4707.

Tatsumi Y. 1983 Generation of arc basalt magmas and thermal structure of the mantle wedge in subduction zones. *Journal. of Geophysical. Research,* 88: 5815-5825.

Ulmer P. 1989 The dependence of the Fe^{2+}-Mg cation partitioning between olivine and basaltic liquid on pressure, temperature and composition: An experimental study to 30kb. *Contributions to Mineral.ogy and Petrology,* 101: 261-273.

van der Laan S.R. & van Groos A.F.K. 1991 PtFe alloys in experimental petrology applied to high-pressure research on Fe-bearing systems. *American Mineral.ogist,* 76: 1940-1949.

Walker D., Shiabata T. & Delong S.E. 1979 Abyssal tholeiites from the Oceanographer Fracture Zone II: Phase equilibria and mixing. *Contributions to Mineral.ogy and Petrology,* 70: 111-125.

Walter M.J. & Presnall D.C. 1994 Melting behaviour of simplified lherzolite in the system CaO-MgO-Al_2O_3-SiO_2-NaO from 7 to 35kb. *Journal. of Petrology,* 35: 329-359.

Walter M.J., Sisson T.W. & Presnall D.C. 1995 A mass proportion method for calculating melting reactions and application to melting of model upper mantle lherzolite. *Earth and Planetary Science Letters,* 135: 77-90.

Wood B.J. 1990 An experimental test of the spinel peridotite oxygen barometer. *Journal. of Geophysical. Research,* 95: 15845-15851.

Wood B.J., Bryndzia L.T. & Johnson K.E. 1990 Mantle oxidation state and its relationship to tectonic environment and fluid speciation. *Science,* 248: 337-345.

Wyllie P.J. 1967 Ultramafic and related rocks, 464 p., Wiley, New York.

Wyllie P.J. 1981 Plate tectonics and magma genesis. *Geol. Rundsch.,* 70: 128-153.

Yoder H.S.J. 1969 Calcalkalic andesites: experimental data bearing on the origin of their assumed characteristics. *In* Birney A.R. (eds), Proceedings of the Andesite Conference. Oreg. Dep. Geol. Miner. Ind. Bull., 65: 77-89.

Yoder H.S.J. & Tilley C.S. 1962 Origin of basalt magmas: an experimental study of natural and synthetic rock systems. *Carnegie Institute of Washington Yearbook,* 56: 156-161.

APPENDIX 1

Estimation of Melt H_2O Content

Where melt H_2O could not be measured directly using SIMS methods, theoretical H_2O concentrations in the glasses were calculated using the batch melting equation:

$$F = (C_o/C_l\text{-}D)/(1\text{-}D)$$

where F = melt fraction in the charge
C_o = bulk H_2O content in the charge
C_l = melt H_2O
D = Nernst partition coefficient, $H_2O_{peridotite}/H_2O_{melt}$

For simplicity D was assumed to be zero. Olivine, opx and cpx can contain small amounts of H_2O (Bell & Rossman, 1992; Kohn, 1996) resulting in a very small but positive D. The errors introduced by assuming D=0 are significantly less than those derived from the calculation of melt fraction in the charge. The batch melting equation then becomes:

$$\text{Melt } H_2O = \text{melt fraction in the charge} \times \text{bulk } H_2O \text{ content in the charge}$$

Melt fraction in the charge was estimated by mass balance, using the analysed compositions of all phases and the bulk composition of the whole capsule (see Appendix 4). Bulk H_2O content in the charge was calculated from the proportions and H_2O contents of the starting mixes used. Error in estimated melt fraction in the charge was propagated to give the error in the theoretical H_2O concentration in the glass.

Amphibole can contain moderate amounts of H_2O (≈2wt%). For experiments with stable amphibole, D will be significantly greater than zero. Due to lack of data for H_2O partitioning between amphibole and melt in peridotite, we have simply decreased the bulk H_2O according to the proportion estimated to be held by the amphibole in the charge. Amphibole proportion in the charge was estimated by mass balance (see Appendix 4) and amphibole H_2O content was estimated by stoichiometry. Melt H_2O was calculated assuming D for the remaining phases (olivine, opx, cpx and spinel) to be zero, as before.

APPENDIX 2

Estimation of H_2O loss from Fe_2O_3 Mass Balance

1. All H_2O loss was assumed to occur by H_2 loss and accompanying Fe oxidation. This methods disregards any contribution to H_2O loss by diffusion of molecular H_2O from the charge.

2. Fe_2O_3 in starting materials (wt%)

Fe_2O_3/FeO* in the basalt starting mix was calculated using the equation of Kress & Carmichael. The nominal value for fO_2 at which the basalt mix was reduced at 1atm was used. The real (rather than nominal) basalt composition was used on a volatile-free basis, i.e. summed to 100wt%. Fe_2O_3/FeO* in the peridotite was estimated to be 0.1. Fe_2O_3 content (in wt%) of the basalt and peridotite mixes was calculated using their measured FeO* contents.

3. Fe_2O_3 in run products (wt%)

Fe_2O_3/FeO* in the melt was calculated such that $D^{Mg\text{-}Fe}$ ol-m agrees with Ulmer's predicted value at 1.5GPa. Fe_2O_3/FeO* in the spinel was calculated such that, on a molar basis, the sum of the cations equals 3 (per 4 oxygens). Fe_2O_3/FeO* in cpx was estimated to be 0.1. Fe_2O_3/FeO* in opx and ol was assumed to be negligible. Fe_2O_3 content (in wt%) of melt, spinel and cpx was calculated using FeO* contents analysed for each phase by EMP.

4. Phase proportions (wt%)

The relative proportions of the starting mixes used were those added to the charge. The relative proportions of the run products were calculated by mass balance, using all phase compositions and the bulk composition of the charge.

5. H_2O loss (relative %)

Change in Fe_2O_3 content of the bulk composition of the charge during the experiment was calculated. Molar change in H_2O was assumed to be equal to molar change in Fe_2O_3, and absolute change in H_2O in wt% was calculated. Relative change in H2O in the charge (in %) was calculated using the nominal bulk H_2O of the charge.

6. Errors

Standard deviations (SD) and standard errors (S) for phase proportions were calculated from the mass balance. SD and S for phase composition were calculated from microprobe analyses. Errors were propagated to give error in Fe_2O_3 in run products. Error in Fe_2O_3 in the starting mixes was assumed to be negligible. Error in Fe_2O_3 was propagated to give error in H_2O loss.

APPENDIX 3

Estimation of Peridotite H_2O Content

The H_2O content of the peridotite at equilibrium was calculated as follows:

Peridotite H_2O = estimated melt fraction x melt H_2O

This is a simplified form of the batch melting equation, where D^{H2O} peridotite-melt is assumed to be effectively zero, as before. Estimated melt fraction was calculated by 2-stage mass balance (see Appendix 4). Melt H_2O was measured directly or calculated as in Appendix 1.

In experiments with stable amphibole, then:

Peridotite H_2O = (estimated melt fraction x melt H_2O) + (estimated amphibole fraction x amphibole H_2O)

In the subsolidus experiment 1100B, then:

Peridotite H_2O = estimated amphibole fraction x amphibole H_2O

APPENDIX 4

Estimation of Degree of Melting (F) and Error Propagation

1. Solid phase compositions

Olivine compositions were checked for stoichiometry and averaged. All pyroxene analyses are checked for stoichiometry and non-stoichiometric analyses were discarded. Multiple analyses from each experiment were plotted in terms of Ca vs Al (6-oxygen basis). Rim compositions were chosen as an average of the most evolved stoichiometric analyses. Amphibole analyses were plotted in terms of Ca and Al (6-oxygen basis), and analyses trending towards pyroxene or melt composition were discarded. Spinel compositions were averaged. The mass balance method is sensitive to the spinel composition used (Robinson *et al.*, 1998). In 1 experiments (VN1160), the whole-capsule bulk composition mass balance calculation resulted in a small (<0.5%) negative proportion of spinel. To correct for this, the same proportion of spinel was subtracted from the bulk composition and the mass balance calculation repeated, but excluding spinel. Garnet compositions were checked for stoichiometry and averaged.

2. Whole capsule bulk composition

Real rather than nominal starting material composition was used for peridotite Leo3, and was determined by XRD methods. Nominal starting material composition was used for peridotite LeoP1. Basalt starting compositions were glassed at 1GPa, 1300°C using a Au-Pd-Pt double capsule, for a run duration of 30 mins. All liquids were analysed by electron microprobe. Whole capsule bulk compositions were calculated according to the relative amounts of powders added to the capsule. Weighing errors were not taken into consideration.

3. Whole-capsule mass balance

Solid phase compositions and liquid were mass-balanced to the whole-capsule bulk composition. This gives an estimate of the abundance of the phases in the experiment. An important assumption was made that the relative proportions of the solid phases would be the same in the experiment (with its shifted bulk composition) as they would be if the experiment were performed by simply melting the bulk composition of interest (Leo3 or LeoP1), *i.e.* a direct melting experiment.

In two experiments where amphibole and melt co-exist, the mass balance method was very sensitive to the compositions of the 2 phases. If both amphibole and melt were included, the whole-capsule bulk composition mass balance calculation resulted in an unrealistically high (>20%) proportion of one, and a high (>15%) negative proportion of the other. To correct for this, the proportion of amhibole in the charge was estimated from EMP backscatter image observations, and subtracted from the whole-capsule bulk composition. The mass balance calculation was then repeated, but excluding amphibole. To check the sensitivity of the mass balance calculation, the proportion of amphibole subtracted from the whole-capsule bulk composition was varied. It was found that, within the range of amphibole proportions considered reasonable from EMP backscatter image observations, estimates of melt fraction agreed within 2S. The preferred estimate of amphibole proportion was that which gives the smallest residual error in the whole-capsule bulk composition mass balance calculation. Where 2 estimates of amphibole proportion give very similar residual errors, the estimate most consistent with the EMP backscatter image observations was used.

4. Partition coefficients

Nernst partition coefficients ($D = C^i_{xtl} / C^i_{liq}$ where C^i_{xtl} is the concentration (wt%) of oxide *i* in a phase and C^i_{liq} is the concentration (wt%) of oxide *i* in the liquid) for each oxide were calculated for each phase, *i.e.* D_{Na2O} is calculated for olivine, opx and cpx, and so on for the other oxides.

5. Bulk distribution coefficients

The solid phase proportions derived in (3) are normalised to sum to one for olivine, opx, cpx, spinel (or garnet) and amphibole (if present). The solid modes were then used to weight the separate D's to produce a single bulk distribution coefficient ($\overline{D}$) for each oxide in each experiment.

6. Melt fraction

The batch melting equation was used to calculate F for each oxide:

$$F = \left(C_o / C_l - \overline{D}\right) / \left(1 - \overline{D}\right)$$

where $\overline{D} = \sum X_i D_i$.

C_o = concentration of the oxide in the peridotite bulk composition (Leo3 or LeoP1) and *not* in the whole capsule bulk composition.

C_l = concentration of the oxide in the liquid

X_i = fraction of solid phase *i*

D_i = Nernst partition coefficient for oxide *i*

7. Propagation of errors

As errors in $\overline{D}$ and C_l are correlated, the batch melting equation is rewritten so that:

$$F = \left[\frac{C_o}{C_l} - \frac{\sum_{xtls} X_{xtl} C^i_{xtl}}{C_l} \right] \Bigg/ 1 - \frac{\sum_{xtls} X_{xtl} C^i_{xtl}}{C_l}$$

and simplified to:

$$F = \frac{C_o - \sum X_{xtl} C^i_{xtl}}{C_l - \sum X_{xtl} C^i_{xtl}}$$

This was then differentiated by parts to give an error equation in terms of standard errors which is of the form:

$$S^2_{F_i} = \left(\frac{\partial F}{\partial C_o} \right)^2 S^2_{C_o} + \left(\frac{\partial F}{\partial C_l} \right)^2 S^2_{C_l} + \sum_{xtals} \left[\left(\frac{\partial F}{\partial C^i_{xtal}} \right)^2 S^2_{C^i_{xtal}} \right] + \sum_{xtals} \left[\left(\frac{\partial F}{\partial X_{xtal}} \right)^2 S^2_{X_{xtal}} \right]$$

where S_F = standard error in F

S_{C_o} = standard error of the oxide in the peridotite bulk composition

$S_{X_{xtl}}$ = standard error in the estimate of the mode for the crystal phase

S_{C_l} = error of the oxide in the liquid. In experiments where the liquid quenched to a glass, S_{C_l} = 1 standard error. In experiments where the liquid quenched to a mat of crystals and interstitial glass, S_{C_l} = 2 standard errors. This reflects the greater difficulty in analysing a quench mat accurately, and is considered to make the melt fraction estimate more robust.

and

$$\frac{\partial F}{\partial C_{l_C}} = -F \Big/ C_l - \left(\sum_{xtls} X_{xtl} C^i_{xtl} \right)$$

$$\frac{\partial F}{\partial C^i_{xtal}} = X_{xtal}(F-1) \Big/ C_l - \left(\sum_{xtls} X_{xtl} C^i_{xtl} \right)$$

$$\frac{\partial F}{\partial X_{xtal}} = C^i_{xtal}(F-1) \Big/ C_l - \left(\sum_{xtls} X_{xtl} C^i_{xtl} \right)$$

The error in C_o is zero as the bulk composition is fixed.

8. Weighted mean melt fraction ($\overline{F}$)

The average melt fraction for each experiment is calculated as a weighted mean in the form:

$$\overline{F} = \frac{1}{\sum_i S^{-2}_{F_i}} \left(\sum \frac{F_i}{S^2_{F_i}} \right)$$

The standard error in $\overline{F}$ is:

$$S_F = \left(\sum_i S^{-2}_{F_i} \right)^{-\frac{1}{2}}$$